Electrical Impedance Tomography (EIT)

The Establishment of a Dual Current Stimulation EIT System for Improved Image Quality

Prepared By:

Ezra Luke America

Submitted to the Department of Electrical Engineering at the University of Cape Town in fulfillment of the academic requirements for a Degree of Master of Science in Electrical Engineering

Supervisor:

Dr. Mohohlo Samuel Tšoeu

Department of Electrical Engineering

University of Cape Town

November 1, 2017

This Dissertation is dedicated to my father, Joseph Ismael America (10 August 1947 – 15 September 2017), who passed away from stage four lung cancer.

Declaration

1. I know that plagiarism is wrong. Plagiarism is to use another's work and pretend that it is one's own.
2. I have used the IEEE convention for citation and referencing. Each contribution to, and quotation in, this report from the work(s) of other people has been attributed, and has been cited and referenced.
3. This report is my own work, and has not been submitted to another institution for a Degree.
4. I have not allowed, and will not allow, anyone to copy my work with the intention of passing it off as their own work or part thereof.

Signed by candidate

Signature: (Ezra Luke America)

Date: 03/08/2017

Abstract

Electrical Impedance Tomography (EIT) is a noninvasive imaging technique that reproduces images of cross-sections, based on the internal impedance distribution of an object. This Dissertation investigates and confirms the use of a dual current stimulation EIT (DCS EIT) system. The results of this investigation presented a size error of 2.82 % and a position error of 5.93 % in the reconstructed images, when compared to the actual size and position of the anomaly inside a test object. These results confirmed that the DCS EIT system produced images of superior quality (fewer image reconstruction errors) to those produced from reviewed single plane stimulating EIT systems, which confirmed the research hypothesis. This system incorporates two independent current stimulating patterns, which establishes a more even distribution of current in the test object, compared to single plane systems, and is more efficient than 2.5D EIT systems because the DCS EIT system only measures boundary voltages in the center plane, compared to 2.5D EIT systems that measure the boundary voltages in all electrode planes. The system uses 48 compound electrodes, divided into three electrode planes. Current is sourced and sunk perpendicularly in the center plane, to produce a high current density near the center of the test object. Sequentially, current is sourced through an electrode in the top electrode plane and sunk through an electrode in the bottom plane, directly below the source electrode, to produce a high current density near the boundary of the test object, in the center plane. During both injection cycles, boundary potentials are measured in the center plane. Following the measurement of a complete frame, a weighted average is computed from the single and cross plane measured data. The weighted measured voltages, injected currents and Finite Element Model of the object is used to reconstruct an image of the internal impedance distribution along a cross-section of the object. This method is applicable to the biomedical imaging and process monitoring fields.

Acknowledgements

To my supervisor: gratitude is paid to my project supervisor. Your questions and explanations on tough concepts have helped me exercise critical thinking and systematic problem solving.

To the control laboratory facilitator (Mr. D. De Maar): gratitude to you for all your efforts to provide a comfortable working environment.

To my family: thank you for all the support that you have shown me throughout these trying times. Especially to Gavin Strauss, your system debugging skills are exceptional and provided great insight, and to Zaakirah Dawood-Hawa for your patience and unending encouragement and support even in times of doubt.

To my sponsors: gratitude is paid to my sponsors (The Frank Wilhelm Trust Scholarship), for all the faith that you have placed upon my completion within the prescribed time and for providing the necessary finances needed to comfortably complete my Masters.

Contents

List of Figures

List of Tables

1 Introduction

This report discusses the design, implementation and control of an Electrical Impedance Tomography (EIT) system, which is used to detect and monitor anomalies within a test tank. This chapter introduces the concept of EIT, background on the current state of the art, the research hypothesis and questions that this report aims to answer, the objectives of and the approach taken to complete the research.

EIT is a noninvasive imaging technique that creates images of cross-sections of objects by discriminating an object based on estimates of its internal electrical properties; estimated impedance distribution within the medium [1]. Current is injected into the object and the current density establishes resultant boundary potentials which are measured, and, using the known injected current and measured boundary potentials, a map of the internal impedance distribution of an object can be realized [2]. Imaging of this internal impedance distribution is performed in the following major steps.

First, a forward model of the physical system is produced to hold important properties of the test object such as its physical dimensions, current injection protocol, and boundary voltage measurement protocol [1]. All of these properties are used when computing a sensitivity matrix, also known as the Jacobian matrix, which describes how the boundary potentials change due to a change in the internal impedance distribution [3], [4]; when using the EIT sensitivity approach.

The next step is to form an inverse model for the EIT problem. It is known as the inverse model because the Jacobian matrix is inverted and multiplied to the measured boundary potentials to form a matrix of estimated internal impedances [5]; for a linear EIT problem. This means that the inverse model uses the inputs and the measured outputs of an object, to compute the model parameters. This estimated impedance distribution within the object, is used to reconstruct an image of the internal electrical properties of the object.

A few fields that employ EIT are the biomedical, industrial and geophysical fields. In the biomedical imaging field, EIT is used to detect, monitor and classify malignant tissue, measure brain function, monitor cardiac systems, detect a haemorrhage or image the thorax [1]. In the industrial fields, EIT is used as a means of non-destructive testing (due to its non-invasive properties) to detect cracks, image fluid flows and fluid distribution in pipelines and mixing vessels

[1]. In the geophysical fields, EIT is used to measure geophysical surfaces, cross boreholes and prospecting [1].

The advantages of EIT include low cost, fast imaging, portability and a non-invasive characteristic. However, the electrical current that is injected through a pair of electrodes, attached to the boundary of a three-dimensional medium, will disperse non-linearly throughout the domain of the medium [1]. The scattering of current in the medium results in poor current distribution within the measurement plane, which means that a change in conductivity in the plane will have an insignificant effect on the boundary potentials; which results in poor detection of anomalies due to poor current distribution. EIT is a nonlinear soft-field problem, which assumes that all electrical current travel within the measurement plane. Further disadvantages of EIT include electrode errors and noise susceptibility [1]. These are major disadvantages of EIT which delay large scale implementation in clinical fields that require high accuracy and reliable measurements, such as routine medical analysis and anatomical imaging. In contrast, EIT does show promise for continuous bedside monitoring of cerebral ventricular haemorrhage and gastric emptying [1].

Furthermore, a dynamic class of EIT, called functional EIT, can be considered to reconstruct images that help develop an intermediate understanding of the changes within a medium. These images are based on a change in measured data taken at different times or a change in the impedance caused by a frequency sweep of the injected signals or by injecting several signals, having different frequencies [6], [7].

1.1 Background and the current state of EIT

In a biological case, electro-chemical conductivity depends on the free ion concentration which allows one to differentiate between absolute EIT, which is based on the difference in free ion content between various biological tissues, and relative or functional EIT which is based on the different functional states of one and the same tissue [8]. Due to the fact that free ion content determines the conductivity of tissue and fluid, muscle and blood will conduct the applied currents better than fat, bone or lung tissue. Hence, when observing the voltage patterns from the measured boundary data, one will notice peaks or dips in the voltage profile (established by finding the difference between two datasets of the measured boundary voltages taken at different times; for time-difference EIT) caused by an inhomogeneity which could be the result of a

malignant tissue. This observation is commonly simulated using a cylinder phantom test tank filled with a salt solution, and placing an object (having a different impedance distribution) into the tank, creates a nonhomogeneous medium through which current flows [1].

In contrast to linear x-rays used in Computed Tomography (CT), EIT uses low amplitude electrical currents which travel in three dimensions along several paths of low resistance. This means that part of the electric current leaves the transverse plane and results in a change of impedance. This increases the complexity in EIT image reconstruction because there are usually several solutions for the reconstruction of images of a 3-D area projected onto a 2-D plane [1]. Furthermore, difference EIT eliminates some of the effects of current dispersions, because it uses a modest number of measurements to recover a modest number of unknown impedance parameters [1], and given that the measurements hold the difference in the state of the medium, means that some of the common irregularities from several frames such as current dispersions will be eliminated. Therefore, the mathematical problem of recovering a large matrix of the object's unknown internal impedances given the surface potential measurements and known injected currents, is severely ill-conditioned as there is no one-to-one mapping from measured boundary potentials to unknown internal impedances. This means that the limited number of boundary measurements are not able to detect arbitrarily large changes in the impedance distribution at a given system precision, and according to the Hadamard criteria, the solution of unknown internal impedance distribution does not continuously depend on the measured data [1]. Consequently, EIT is an ill-posed problem in which regularization is one of several preferred methods used to compute a stable and accurate solution, when including in the solution, prior knowledge about the problem [9], [10].

As aforementioned, EIT has two common methods for reconstructing images, the first is absolute EIT and the other is functional EIT. In addition, there are time and frequency difference imaging methods which form part of a subclass called difference imaging (Functional EIT). Time difference EIT, for instance, has one major advantage over absolute EIT; inaccuracies that result from insufficient skin contact of surface electrodes, impedance transfer or inter-individual anatomy can be dismissed because most artifacts will eliminate themselves due to simple image subtraction [8]. However, time difference imaging becomes troublesome when the system changes state at a high rate [1], [8]. Frequency difference on the other hand works fine in rapid changing systems (such as uncontrolled systems – example: lungs). However, the system could get swamped by repetitive data [1], which is a result of an object that did not change its state over the measurement time. This means that, although several signals of varying frequencies are injected into the object, the measured frame will show the same information for all frequencies, producing repetitive data.

EIT is a relatively new imaging technique, therefore, it is yet to be adopted on a large scale as an industrial or a medical or geophysical tool [1]. Stepping stones to the adoption of EIT on a large scale requires a system that is robust, has improved resolution and is highly reliable to ensure routine and confident employment for diagnostics.

Among other limitations, 2D imaging cannot provide vertical location information of off-plane contrasts; for a horizontal electrode plane system. Alternatively, there are ways of theoretically predicting the effect that an off-plane anomaly has on the resulting image by using 2.5D image reconstructions [11].

1.2 Hypothesis and research questions

The hypothesis of this investigation is that a dual current stimulation protocol can be used to reconstruct images that have a higher image quality, compared to those produced from a single current stimulation protocol EIT system, which uses time-difference EIT. Commonly, EIT systems use a single current stimulation pattern, which results in a system that has a non-uniform current distribution; which is evident in the reconstructed images for different anomaly positions that show a variance in the reconstruction errors with some images having more errors than others based on the position of the anomaly. For example, if current is injected through adjacent electrodes, then there will be a high current density near the boundary and a significantly weaker current density near the center of the test tank [12], which is evident in the reconstructed images that show lower image reconstruction errors in the size and position of anomalies that were placed near the boundary, compared to those reconstructed for anomalies near the center. The inverse is true for the ninety degree current stimulation pattern; the opposite injection method introduces ghosting. This means that, for a given single current pattern, some areas within the test medium will have a high detectability of anomalies that are placed in those areas, and a significantly lower detectability of anomalies that are placed in areas that have a weak current density. It is then assumed that, using two current stimulation patterns, a dual current stimulation protocol will have a high detectability throughout the medium, when using one current pattern that has a high current density near the boundary, and the second pattern having a high current density near the center of the test tank. Furthermore, three electrode planes are used to produce the two current stimulation patterns. The center plane is used to inject current using a specific pattern, and the top and bottom planes are used to establish a cross-plane current stimulation protocol.

Therefore, the research questions to be investigated are:

1. *Could cross-plane current stimulation in conjunction with single plane current stimulation improve image quality, when using carefully selected current stimulation patterns and an optimal electrode size and positions?*
2. *What are the achievable advantages that dual stimulation EIT has over single plane stimulation EIT?*

These questions are directed at enhancing the reconstructed images by improving the EIT system prior to image reconstruction.

1.3 Objectives of this study

The main goal in this research is to use the concept of electrical impedance tomography to detect and monitor anomalies in a phantom test tank. The following objectives will need to be addressed in order to come up with a suitable long lasting solution.

- Critically analyze the various configurations and designs of electrical impedance tomographic systems.
- Design a working EIT system that is cost-effective, portable and small. Furthermore, a method to introduce a second, independent, current injection pattern needs to be established.
- Develop an understanding of various algorithms used to control an EIT system in order to efficiently apply low amplitude current patterns and reconstruct images of the test object, using the weighted average of all measured data from two independent current injection patterns.
- To further improve the system accuracy, requires improvement in the data acquisition bit accuracy. This is achieved by using a 24-bit Analog-to-Digital Converter (ADC) Integrated Circuit (IC) which converts the continuous boundary voltage measurements to a digital format for further PC based analysis. The results are then compared to a 16 bit EIT system. Therefore, the objective is to identify how well the image quality has improved for a 24-bit system, when compared to a 16-bit system.

1.4 Scope and limitations

This study does not deal with the development of an image reconstruction software; existing software will be used in this regard.

The study has a duration of two years. Hence, this time constraint will affect the depth of the research. As such, the motivation for this work included the design of a system which can detect anomalies within a test tank, however, the designed system is not focused on biomedical applications during the prototype phase and thus, using human test subjects and building a purely biological test phantom is outside the scope of this work. Tests will be conducted on the system to provide results that can be used to answer the research questions. Furthermore, only time difference 2D imaging will be implemented.

The designed prototype system will be made of cost effective parts. This further limits the hardware capabilities.

1.5 Author contributions

While there are EIT systems that use single plane current stimulation, or multiple plane stimulation (as in 3D EIT), and other systems that use the zigzag current stimulation method, these systems do not incorporate more than one current stimulation pattern. This work therefore extends the study of image enhancement, in EIT, by incorporating multiple current stimulation patterns, and provides proof that the dual current stimulation system reconstructs images that have a higher image quality than those produced from single plane stimulation (time-difference) EIT systems. Furthermore, the challenges and limitations of a dual current stimulation system, compared to the time-difference single plane EIT system, will be explored.

In addition, time-difference single plane stimulation EIT systems suffer from a non-uniform current distribution, which results in a system that has a non-uniform detectability as the anomaly is moved to different positions inside the test tank. Therefore, this work shows that the dual current stimulation system produces images of a higher image quality and detectability, irrespective of the position of the anomaly.

1.6 Research approach

The aim of this project is to detect and monitor anomalies within a phantom test tank using EIT. Additionally, to aid the investigation, an EIT system will be built and tested.

To ensure that this dissertation is finely ‘tuned’, several stages were revisited on several occasions and this paper follows a logical process taken to answer the research questions. Therefore, this project started with an in-depth discussion with the project supervisor on the terms of reference and the project deliverables.

The next step involved planning of the project timeline and reachable short term milestones. These milestones included, finishing activities such as the different stages of the product design at the end of each week. Furthermore, certain activities were allowed to stretch over the entire duration of the project; such as the literature review.

Once the timeline was set, the next step involved conducting a literature review to acquaint oneself with the body of knowledge and state of the art to avoid duplicating the work of existing projects.

Following the initial phase of the literature review, a hypothesis and questions that test the hypothesis were postulated.

After the hypothesis stage, a careful choice of the system design and mathematical algorithms were made. Furthermore, simulations of the model of the system were made to test the system design, before the system can be fabricated. Once the design and simulations were completed, the system was built and tested to ensure that a working system results from the design. Thereafter, the fabricated system was used to detect anomalies in the phantom test tank.

Thereafter, key information was extracted from the acquired data from the experimental results, which were used to answer the research questions. These answers were discussed in relation to the hypothesis, and conclusions were drawn.

Figure 1- 1 shows the project top-down diagram, which was followed to ensure successful completion of the project.

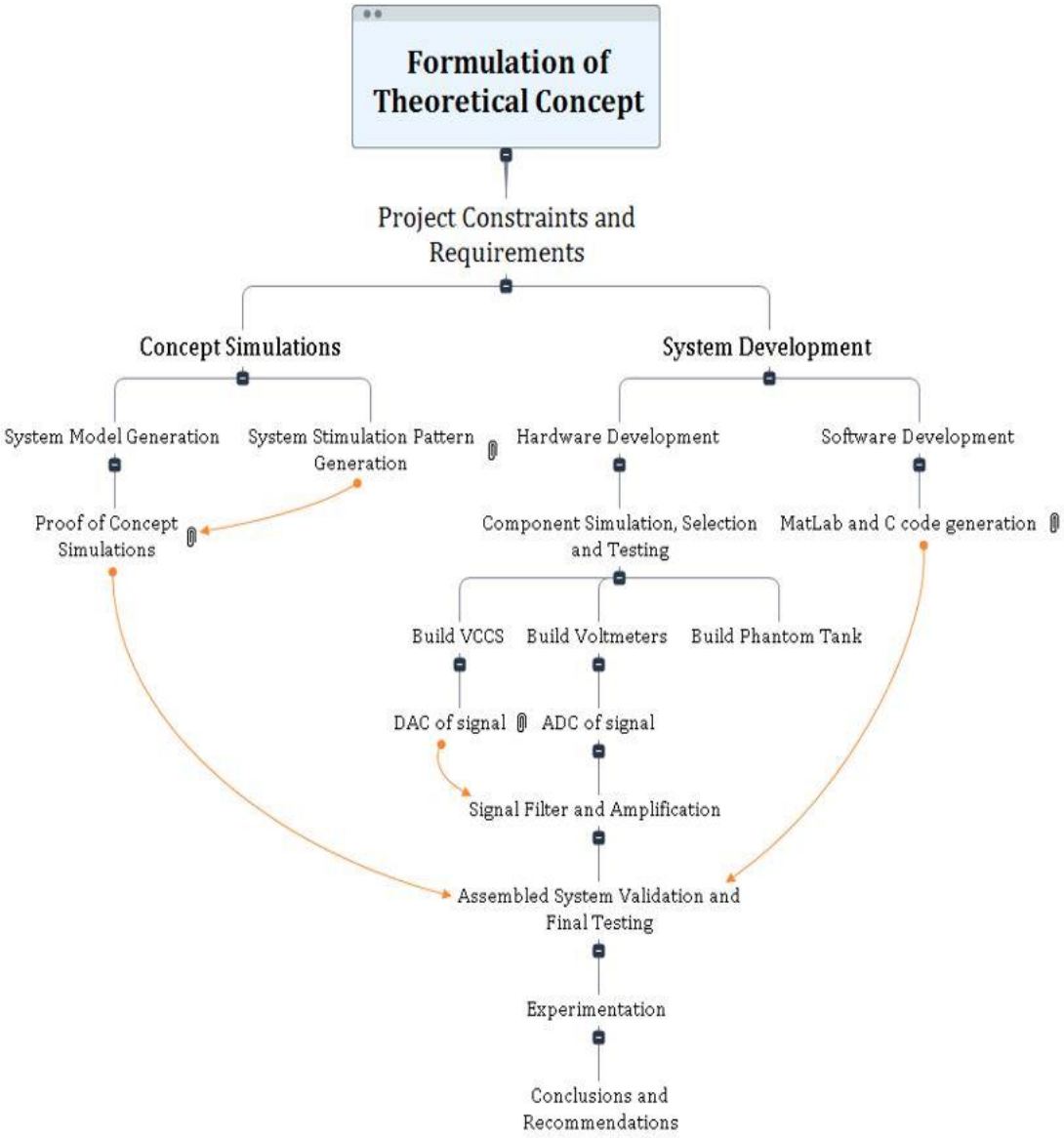

Figure 1- 1: Project top-down diagram to be followed for successful completion of the project.

Figure 1- 1 shows the process followed to ensure successful completion of the project. The project diagram starts with the formulation of the governing theoretical concept, which needs to be tested throughout the investigation. Following the development of the theoretical concepts, a few project constraints need to be established to constrain the project to focus only on ways of answering the research questions. The project divides into concept simulations and system development. The concept simulations are used to provide simulations which accept or negate the research

hypothesis, by developing proof of concept simulations. At the same time, while simulating the EIT problem, the system is developed. The system development process involves simulating several viable circuit designs using cost-effective and easily accessible components which meet the system functional constraints. From these simulations, the best performing components (relative to the cost of these components) and circuit designs are selected and built. After building these circuits, the next step is to test the sub-systems, followed by the assembly of the complete system. Once the complete system is assembled, the written codes will be implemented onto it, to test the complete operation of the system and to ensure that the system operates as it was intended to operate. Following the final system test is the capturing of data from the EIT experiment. This data is analyzed and compared to the experimental results from available modern related works. A conclusion is drawn from these results and recommendations are outlined to aid future developments.

In addition, a Gantt chart was compiled from the diagram in Figure 1- 1. A summary of the project Gantt chart is outlined in the table below. Furthermore, the table below only shows the dates and organization of tasks based on the project's critical timeline.

Table 1- 1: Summary of the Project Timeline, obtained from the project Gantt chart.

Project Stage	Number of days	Dates (dd/mm/yy)	Comment
Project start	-	14/03/16	Project begins.
Constraints and requirements	30	14/03/16 – 13/04/16	Prioritized to occur as soon as possible with highest priority.
Concept Simulations	97	13/04/16 – 19/06/16	Prioritized to occur immediately after constraints and requirements.
Hardware Development	366	19/06/16 – 20/06/17	Prioritized to run in parallel with Concept Simulations.
Software Development	120	20/02/17 – 20/06/17	Prioritized to run in parallel with, and to start four months before the end of Hardware Development
Experimental Results	10	20/06/17 – 30/06/17	Prioritized to run as soon as System Development ends.
Conclusions and Recommendations	10	30/06/17 – 09/07/17	Prioritized to run last, as soon as Experimental Results end.
Project End	-	09/07/17	Project terminates.

The number of days selected for each project phase in Table 1- 1, was chosen to accommodate the time needed to acquaint oneself with related works, for each phase. It was assumed that the project constraints and requirements stem from the research hypothesis and research questions, and thus, only a short expected time is needed to formulate the project constraints. Concept simulations require additional time to familiarize oneself with the existing Electrical Impedance and Diffuse Optical Reconstruction Software (EIDORS) and available literature on generating mathematical models of a real EIT problem and selecting a stimulation pattern. The hardware development phase is expected to take the longest of all the project phases, because it deals with various subsections of the hardware, such as the design and simulations of various components and circuits, and the assembly and final testing of the assembled system. Therefore a large portion of the project timeline is dedicated to ensure that the EIT system hardware functions as intended. The software development runs in parallel with the hardware development and returns the final codes that are used to ensure that the system functions properly. The experimental results is expected to take a few days, because it is assumed that once the system operates as it was intended to, then placing different anomalies inside the test tank and reconstructing images of the internal impedance distribution will not take more than ten days. The same logic applies to the conclusions and recommendations phase, because one can only conclude after the experimental results have been analyzed and compared to the results of other related works.

1.7 Report outline

This report is structured as follows.

Chapter 1: Introduction

This chapter introduces the problem of Electrical Impedance Tomography. A few possible applications of EIT are described. The objectives, hypothesis and research questions are outlined. The chapter then establishes the scope of the work, author contributions and research approach.

Chapter 2: Literature Review

This chapter describes the concept of Electrical Impedance Tomography and its pitfalls. Following this, the chapter then shifts to focus on exploring the current literature of related work on the development of an EIT system. These studies are then critically analyzed. This chapter reveals the difficulty of EIT (ill-posed and ill-conditioned nature), the limitations of EIT (spatial resolution),

solving the forward and inverse problem of EIT using the Finite Element Method to discretize the domain, several EIT system topologies are reviewed with a few key considerations per component, selecting a hyper-parameter for regularization, followed by a few performance figures of merit on which to test and compare the reconstructed images to the results from other modern EIT systems.

Chapter 3: Proof of Concept

Provides a proof of concept in the form of simulations, using the EIDORS software, and existing theory. It also introduces a way to inject a second current pattern into a test tank by injecting current across several electrode planes. The chapter presents the limitations in using single plane current stimulation and shows that injecting two independent current patterns into the tank, improves the spatial resolution and detection of anomalies.

Chapter 4: System Design

This chapter deals with the design of the EIT system based on the constraints formed to answer the research questions. It reviews several system concepts followed by a few simulations of each subcomponent in the system. The simulations showed that the designed system is adequate for testing and to help answer the research questions. The final prototype system used a signal generator to generate a voltage that is used to control a mirrored modified Howland current source. This source produces a constant current at the output, irrespective of the variation in the load. The current from the source entered a multiplexer which is used to select the current sink and source electrodes on the test tank. 16 instrument amplifiers were used to measure and difference the resultant boundary potentials on the tank and amplify these signals before sending the signals to an Analog-to-Digital Converter (ADC). The ADC converts the continuous signals to a digital format for further PC based analysis.

Chapter 5: System Test

This chapter explains the tests which were performed to ensure that a working EIT system was assembled and is capable of answering the research questions. The tests showed that the Voltage Controlled Current Source (VCCS) was able to produce a constant current over a load range of 100 Ω to 10 kΩ at frequencies up to 25 kHz, that the multiplexers functioned correctly and produces insignificant loss in transmission of the applied signals, that the instrument amplifiers were able to difference and correctly amplify the measured signals and that the ADC correctly converts the signal to a digital format. Furthermore, the build quality of the test tank was examined.

Chapter 6: Image Reconstruction

This chapter provides the design and execution of the image reconstruction code. Followed by a few tests to see if the system is able to produce repeatable results. To observe the system's ability to produce repeatable results, several measurement frames were capture for four different anomaly positions and the image were analyzed to show repeatable results. The images corresponding to a given anomaly position was shown to produce identical images with identical impedance calculations.

Chapter 7: Experimental Results

This chapter provides the result of the experiments. Followed by a discussion of the results in relation to the comparison between the simulated results versus the experimental results and how well the results of the system compete with other reported systems. The errors in the DCS reconstructed images were significantly less than those from related works. The DCS images were better able to define irregular anomaly shapes and sizes as well as the simultaneous detection of several anomalies of different sizes.

Chapter 8: Conclusions, Recommendations and Future Work

This chapter draws conclusions from the results of the investigation and makes recommendations for future work and adaptations. The chapter concluded that the DCS EIT method was able to produce images of more enhanced quality compared to related works that incorporate 2D imaging. It also concludes that a working prototype system was built and outlines the drawbacks of the system and a few possible ways of improving the system to incorporate multi-frequency imaging; Electrical Impedance Spectroscopy.

2 Literature review

2.1 Introduction

This chapter starts with a brief overview of tomography and the definition of EIT image reconstruction. This is followed by a review of the EIT forward and inverse problems; developed from numerical methods and modelling. The subsequent section of the chapter reviews the concept of difference imaging. After this, a comparison is made between several EIT system concepts, from the available literature, that were successfully built. The chapter ends with a discussion on different performance figures of merit.

2.2 Tomography

Tomography refers to imaging an object in sections, derived from the Greek word *tomos*, through the use of energy waves that penetrate through the object [13]. The resultant image is called a 'tomogram' while the device used to produce this image is called a 'tomogragh'. Some EIT systems focus on reconstructing images from the electrical conductivity, permittivity, electromagnetic permeability or a combination of these to form the impedance.

Electrical Resistance Tomography (ERT) deals with extracting information about the internal electrical conductivity of an object. This is done by injecting an alternating current through a pair of electrodes, and detecting the amplitudes of the measured resultant boundary voltage signals, shown in Figure 2- 1. This form of imaging is not frequency dependent, and thus, only depends on the amplitudes of the sourced and measured signals. Therefore, ERT cannot adapt to frequency difference imaging or spectroscopy, and is thus limited to time difference imaging. In contrast, these systems are able to inject short duration signals, which results in an increased temporal resolution [7], [14].

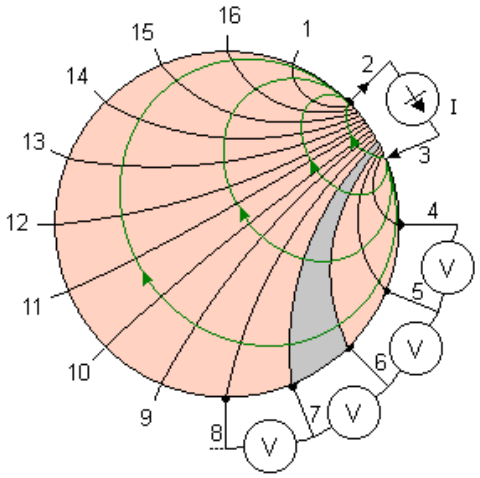

Figure 2- 1: Shows the current injection, voltage measurement scheme used in ERT systems [15].

Electrical Capacitance Tomography (ECT) deals with extracting the dielectric properties of the object, by injecting a multi-frequency current into the medium and measuring the resultant voltages. Based on the dielectric properties between two electrodes, one can extract the capacitance between those electrodes, shown in Figure 2- 2. From these measurements, a map of the dielectric contents of the object can be realized. This method is applicable to frequency difference and spectroscopy imaging, as it is heavily dependent on the excitation frequency. However, the selection of excitation signals are limited. To avoid increasing the complexity of the system, frequency is increased in discrete steps. All of the injected signals have to guarantee an even distribution for the chosen discrete frequencies for which they have been optimized. This requires prior information about these signals at the selected frequencies, which may not be available in spectroscopy systems [1].

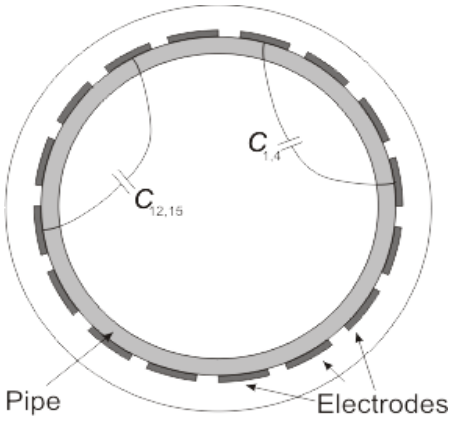

Figure 2- 2: Shows the computed capacitances between different electrodes, based on the dielectric content between those electrodes [16].

Electrical Impedance Tomography (EIT) uses a combination of the first two imaging methods by extracting information about the internal resistive and reactive properties of the object [1]. This modality carries the advantages of the first two. In contrast, it does require more electrodes, increased electronic hardware complexity and signal processing. Some reported systems use separate electrodes for the measurement of the internal resistance and capacitance of an object [15]. Other reported systems use a similar electrode configuration as used in ERT [1].

2.3 How EIT works

An inverse problem, with regard to EIT, is the reconstruction of an image based on the mapping of unknown parameters (**m**) using measured and known parameters (**n**) [1]; when the dimension of matrix **m** is much greater than vector **n**.

Consider the subsequent example of EIT, which demonstrates the imaging of a Thorax using EIT:

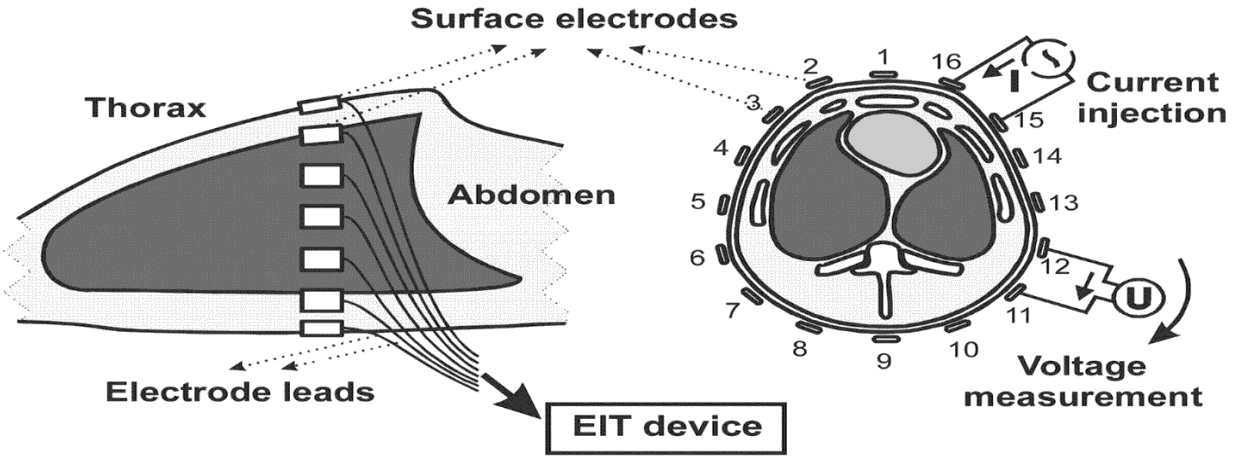

Figure 2- 3: EIT imaging of the Thorax [18]

Figure 2- 3 above, shows the process of imaging the Thorax using EIT. A current is injected at a single pair of electrodes and the voltage is measured at the remaining electrodes. With this information, an image can be reconstructed by mapping the internal electrical properties of the Thorax.

When current is injected into an electrode attached to a medium of unknown internal impedance distribution, as shown in Figure 2- 3, it follows several paths (in the medium) of least resistance,

towards a grounded or current sinking electrode. When current propagates throughout the medium, an electric field is established, which forms potential vectors that are perpendicular to the electric field [16]. These potential vectors also occur at the boundary of the medium, which allows one to measure the boundary potentials [1]. These measured boundary potentials are compared to the computed boundary potentials from the forward problem; a problem which first discretizes the domain of the medium (using the Finite Element Method) then uses the known injected current and an initial guess of the internal impedance distribution to compute the expected boundary potential using Maxwell's equations, and forms a sensitivity matrix relating changes in the boundary voltages to changes in the internal impedance of a medium [17]. The internal impedance distribution is then computed as the product of the inverted sensitivity matrix and the measured boundary potentials; for a linearized EIT problem. Following the computation of the internal impedance distribution of a medium, an inverse problem is solved. The inverse problem assigns a single impedance value to each element in the forward model and uses a color scheme to assign a color to an impedance value [18]. An image is then produced from these elements, by using the element values as pixel values.

Furthermore, most EIT systems employ sinusoidal currents [1]. This is advantageous to the medical field because an alternating injection current significantly reduces the skin resistance and improves current penetration [1]. Furthermore, an alternating injection current provides additional information about the internal impedance distribution, of an object, that varies by changing the frequency of the applied current. Additionally, alternating injection currents reduce electrode corrosion, provide easier filtering of stray signals and is used to comply with safety standards [19].

2.4 The difficulty of EIT

Conventional imaging techniques project a radiation beam (x-ray) in a straight line through the body; which is the case in computerized tomography (CT) [13]. This means that the pixels in the image will affect only a small portion of the measurements. At lower frequency, scattering will occur, which causes the technique to shift from local (beam passes in a straight line through the region of interest) to non-local (the beam gets scattered and some fragments of the beam no longer follow a straight line). This property, of non-locality, becomes more prominent as the frequency decreases, which affects the measured surface voltages induced on the electrodes in CT [1]. Evidently, in EIT, this problem exists at low to moderate frequencies which makes EIT

image reconstruction a difficult task. It is difficult because, ideally, one must solve a set of simultaneous equations which relates every pixel (or voxel, impedance element) to every measurement in order to reconstruct an image of the internal conductivity distribution [20]. Additionally, the ill-conditioned nature of the EIT problem provides additional difficulty, as there are more unknown impedances compared to measurable boundary voltages; this means that the solution does not continuously depend on the measured parameters and becomes unstable, making it a severely ill-posed problem.

Furthermore, a mathematical model of a physical problem is well posed, according to the Hadamard criteria, if:

- A solution exists for all acceptable data.
- A solution continuously depends on the data for stability.
- A solution exists, it should be unique.

Logically, an object will have a large number of internal impedance nodes, while the boundary measurements are severely limited. Hence, mapping a large number of unknown impedance nodes given fewer available measurement data becomes troublesome. In these instances, either a solution does not exist or there is no unique solution [21].

In EIT, the second point of Hadamard's criteria becomes a problem when recovering, from the boundary data, an unknown conductivity which makes the EIT problem severely ill-conditioned and unstable.

Practically, for any given measurement precision, there exists arbitrarily large changes in the conductivity distribution which cannot be detected by the measured boundary voltages at the same precision [1]. The fact that EIT is aimed at working at low frequencies (between 1 kHz and 1 MHz for biomedical imaging applications) makes the problem worse as this low frequency signals will disperse throughout the object, instead of concentrating the signal paths to the electrode plane. In addition, EIT assumes that all current distribution paths remain inside the electrode plane; which makes it a soft-field problem [1].

One way to solve this problem, requires a hyper-parameter which is used to regularize the problem and provide a practical solution [17]. Furthermore, suppose one knew enough information in advance about the impedance distribution, then a solution to the problem could be formed. Once the information is known, it becomes easier to constrain the solution and discard any significant variations [5]. The hyper-parameter is used to constrain the solution based on

known information such as assumptions and constraints. Typical constraints include a convergence tolerance, minimum length solution, minimum error based on previous solutions or the smoothness (which causes image blurring) of the solution [5].

In terms of the uniqueness of the solution, the conductivity inverse boundary value problem is to show that there exists a complete set of relationships between the measured boundary voltages and the injected currents which forms the conductivity of the body, uniquely [17].

2.5 Limitations of EIT

Current flow is not restricted to the electrode plane, which results in a loss of accuracy when reconstructing the cross-sectional images [1]. Three-dimensional image reconstruction provides a solution to the effects of current dispersions, by measuring the boundary potentials around multiple electrode planes on the surface of the object. Another way to solve this problem is to use functional EIT [8]. In addition, the sensitivity of the EIT system decreases with an increase in the distance from the nearest electrode for tomographic systems.

The next limitation of EIT is its resolution (~6 mm for a 16 electrode system of side-to-side length of 10 cm) which is much lower than conventional imaging techniques (~1 mm) [13]. This resolution is prescribed by the physical arrangement of the electrodes, the number of electrodes and the number of different spatial excitation patterns used. Consider imaging a square medium to detect an internal impedance anomaly. A 16 electrode array will allow 15 optimal patterns if one electrode is used as a fixed ground electrode that, together, form a complete orthogonal set (additional patterns within the same plane add no new information). Each pattern will have 16 measurements which in total results in 240 independent measurements. Thus, for a medium of side-to-side length of 10 cm using 240 electrode patches results in a patch of 6.5 mm per side [1]. This is the spatial resolution of the system. In practice, the resolution of a tomographic system is highest at the boundary and lowest at the center of the image; when sourcing and sinking current through adjacent electrodes. To solve this problem requires additional electrodes and optimized stimulation patterns. This drawback prevents EIT from becoming the preferred screening method [1]. In contrast, increasing the spatial resolution of the system could ensure large scale use of EIT as an imaging tool.

2.6 Numerical methods

This section deals with the solution to the forward problem before solving the inverse problem, of EIT. During each stage, a systematic method to numerically solve the problem is employed.

2.6.1 The forward problem

The forward problem of EIT refers to the linear or non-linear and iterative computations of the boundary potentials from the injected currents, for a known impedance distribution [18]. This forward model is used to predict observations. In this case, the spatial electric field, and hence the boundary potentials, are predicted from the injection of current to a model of known impedance distribution [11]. This allows one to compute the Jacobian, or Sensitivity, matrix which can then be used to solve the inverse problem.

2.6.1.1 Forward equation - conversion from Maxwell to Laplace

The electrical properties of an arbitrary medium vary with position and time ($z(\vec{x},t)$), when it undergoes electrical stimulation. As the stimulation frequency is reduced, so does the internal impedance of a medium reduce its dependency on time ($z(\vec{x})$) [1].

Also, reducing the stimulation frequency significantly reduces the imaginary component of the internal impedance of a medium, because, as the frequency is reduced, only small changes in the reactive component is observed.

Hence, the internal impedance may be represented as:

$$z(\vec{x}) = \sigma(\vec{x}) = internal\ conductance$$

This internal conductance is assumed to be linear and isotropic.

Furthermore, to determine the effect and direction of current flow through the medium and the resulting boundary potential, one needs to consider Maxwell's equations [16]. Based on those

equations, injecting current into a medium sets up an electric field within that medium. The current flow pattern or density, $J(\vec{x})$, is directly linked to the electric field, $E(\vec{x})$, by:

$$J = \sigma E \tag{2.1}$$

The presence of an electric field in a medium, sets up a voltage distribution, $u(\vec{x})$, which are represented by vectors in space. The electric field may be found by computing the negative gradient of the voltage distribution.

$$E = -\nabla u \tag{2.2}$$

Furthermore, by Kirchhoff's current law, the net current at a node in an electrical circuit (similar to a discretized model of a biological specimen) is always zero. Provided there is a zero charge buildup.

$$\nabla J = 0 \tag{2.3}$$

Substituting equation (2.2) into (2.1) and substituting the result into equation (2.3), yields the following equation:

$$\nabla\big(-\sigma\nabla \mathrm{u}(\vec{x})\big) = 0 \tag{2.4}$$

Equation (2.4) is known as the Laplacian for the internal electric potential of a medium. It suggests that the flow of electrons and the voltage are in the direction of the negative electric field. In electrical circuits, conductance multiplied by a change in voltage across a wire, gives the current that flows through that wire. Hence, $\sigma\nabla \mathrm{u}(\vec{x})$ refers to the current at position $\vec{x}$ [1]. In addition, since a reasonable assumption would be that no charge builds up within the medium, the divergence of current or the tendency of the internal current to remain at this position is zero.

After observing the behavior of the current in a medium, the next step involves observing how this current and internal potentials affect the formation of boundary potentials at the electrodes.

Boundary conditions must be developed for stimulating electrodes, grounded electrodes, boundary potential measuring electrodes and the spaces between electrodes. The formation of the boundary conditions are based on the Complete Electrode Model (CEM) [22] which provides an accurate representation of the electrode system.

By ignoring the effects at the edge of the stimulating electrodes, the instantaneous total stimulating current (I_{stim}) perpendicular to a given stimulating electrode (electrode i) is the surface integral of the current density ($\boldsymbol{J}(\boldsymbol{r},t)$) over that electrode [6].

$$I_{stim} = \int_{electrode,i} \boldsymbol{J}(\boldsymbol{r},t).\boldsymbol{n}dS \tag{2.5}$$

The grounded electrode is responsible for sinking all current that is injected through the remaining stimulating electrodes, to ensure charge conservation [6]. For systems that multiplex the ground electrode for each injection, in an attempt to maintain a uniform current distribution pattern within the medium, the instantaneous total current at that grounded electrode is the negative value of the stimulating current. This ensures that a bipolar AC signal is kept for each injection to avoid polarization of the contents of the object, and that there is a conservation of charge.

For systems that use separate stimulation and measurement electrodes, the measurement electrodes ideally have zero current due to the high input impedance amplifiers at the output of these electrodes.

In addition, one boundary condition of a medium would be formed by fixing the normal current, $j\hat{n}$, at every point on the boundary [1].

$$j\hat{n} = -\sigma\frac{\partial u}{\partial \hat{n}} \ , at\ a\ boundary \tag{2.6}$$

Equation (2.6) can then be modified to account for the electrodes at the boundary of the medium.

Equations (2.4) and (2.6) form the forward problem of EIT, which are used to predict the boundary potentials based on a known injected current and an estimated internal conductance. Furthermore, for applications where the internal electrical properties of the medium heavily depend on time and or frequency, requires the replacement of the conductivity with impedance and includes time and space variables in the equations above.

Models that have arbitrary boundary geometries, require numerical methods such as the finite element method of modelling, which converts a continuum problem to a discrete algebraic problem [23].

2.6.1.2 Finite Element Method (FEM) of modelling

The finite element method (FEM) is a technique that models a system based on the approximate solutions to a set of partial differential equations [24]. The FEM is currently the most common method employed to numerically solve the EIT problem [1]. It has the advantage of being able to model arbitrary geometries with various boundary conditions [1]. Other methods, such as the finite difference and volume methods, have more efficient solvers. However, these methods use regular mesh grids, which makes it difficult to accurately model irregular anomalies.

The finite element method reduces the EIT continuum problem of infinite dimension (the continuous electric potential variable is defined over an infinite number of values because it is a function of the infinite number of points in the medium) to one which is discrete with finite dimension. It achieves this by discretizing the medium into triangular elements; forming a finite element mesh as shown in Figure 2- 4.

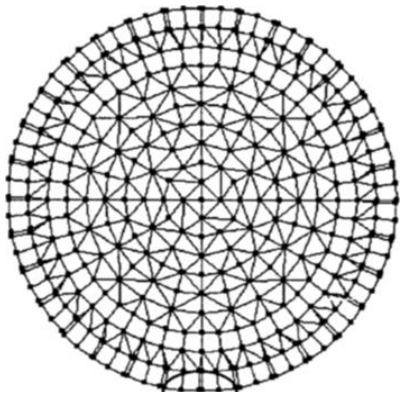

Figure 2- 4: Two-dimensional circular FEM model using 389 nodes and 376 independent elements.

Each element in this mesh, in Figure 2- 4, holds a single value of the internal electric potential variable, which is approximated by a shaping or interpolation function defined only by the nodes (specified fixed points) of the individual element [1]. In most cases, the nodes are the points that

connect adjacent elements. These individual elements collectively define the behavior of the electric potential over the entire medium.

There are three different FEM techniques, listed below [24]:

1. Direct approach: Provides an intuitive way of understanding the FEM. However, it is limited to elements with constant conductivity.
2. Variation approach: Uses calculus to compute the extremes of a potential function. It is used to work with arbitrary element shapes and to solve high order interpolation functions.
3. Method of Weighted Residuals (MWR): Does not depend on a variation statement. It works with a set of governing equations and is mainly used to derive element properties for non-structural applications such as fluid flow.

Each of these approaches proceed with the following sequence, considering a 2D EIT problem [24]:

1. Mesh generation: A finite element mesh made up of finite, non-uniform, non-overlapping elements, connected at nodes, to discretize the spatial domain of a medium.
2. Shaping function selection: Involves selecting a shaping function, which is defined at the connecting nodes of the elements, to approximate the electric potential within an element. These functions are piece-wise, linear or quadratic. Some papers report using higher order functions [25].
3. System Modelling: For each element, a local stiffness matrix is computed from a set of partial differential equations, which is used together with the shaping function to compute the electric potential solution at the element nodes. A global stiffness matrix is formed from all local stiffness matrices.
4. System Solver: This step imposes the boundary conditions, which are categorized into three stages (fixed field variable, derivative of the fixed field variable and a mixture of the first two stages). After imposing these conditions onto the global matrix, it is then inverted to compute the electric potential value at each node.
5. System Solution: Using the shaping functions, and the global matrix, a solution to the entire mesh network is approximated.

For the systems that require adaptive currents and mesh refinements, an iterative approach should be employed. Furthermore, as the order of the shaping function increases or as the number of elements increases (bounded interior angles), the solution converges to a tolerable uncertainty.

After solving the forward EIT problem, one needs to solve the inverse problem. An inverse problem is formulated to reconstruct an image of the medium, based on the mapping of its internal impedance distribution.

2.6.2 The inverse problem

In EIT, the inverse problem also refers to image reconstruction, which is the process of forming an image of a medium by mapping its internal impedance distribution. The impedance of a medium can be static or may vary with time, frequency, or a combination of the two. Thus, there are the following categories of reconstruction algorithms:

1. Static/ Absolute imaging: An image is obtained from the absolute impedance distribution at an instant in time.
2. Time difference imaging: Forming an image from multiple absolute images that are captured at different instances of time. This method is used to observe the change of impedance over time.
3. Frequency difference imaging: Used to observe the change of impedance as the supply frequency is varied.
4. Dynamic imaging: Used to observe fast impedance changes over short intervals.

In this Dissertation, difference imaging is considered, as it is widely understood to improve the stability of reconstructing an image, errors caused by inaccurate electrode positions, non-linearity, poorly defined boundary shapes and 2D approximations of 3D fields [1].

In the forward problem, a linear approximation operator (Jacobian or Sensitivity Matrix) is used to compute the change in impedance for a change in internal potential. For non-linear problems, the linear operator is updated and re-applied at each iteration until the solution converges to a specified tolerance. The Jacobian matrix has the number of columns equal to the number of elements in the mesh network and number of rows equal to the number of boundary

measurements. Each column in the Jacobian, i^{th} column, describes the effect of a change in impedance of the i^{th} element when there is a change in potential between measurement electrode pairs. Other methods have been presented in literature to solve the inverse problem including the back-projection approach and Neural-Networks.

The back-projection approach is derived from the methods used in Computed Tomography [26]. Signals are propagated through the medium in a straight line to observe the attenuation profile. In addition, injecting signals at different angles results in different attenuation profiles as shown in Figure 2- 5, which shows the attenuation voltage profiles for two sources. Furthermore, combining all profiles results in the localization of the attenuating object within the medium. However, in EIT current does not travel in a straight line, which means that current is not evenly distributed through the medium and assuming that current is evenly distributed, results in poor system performance and image quality.

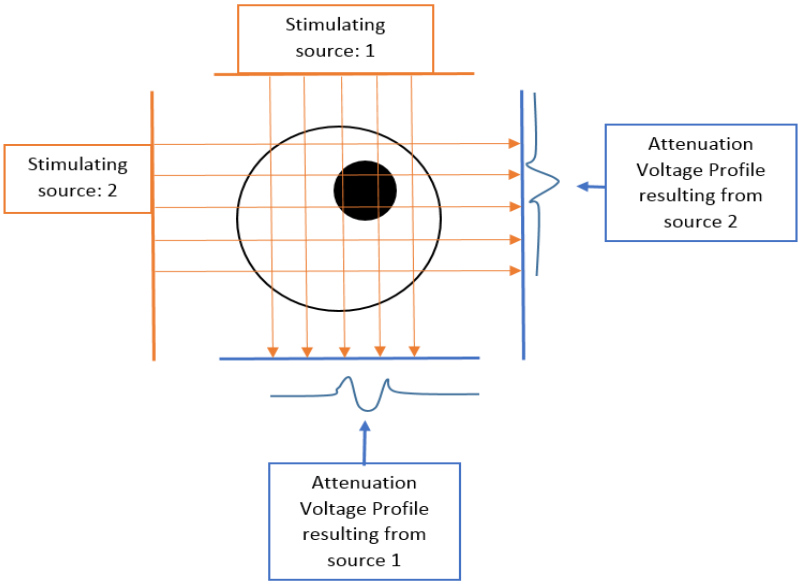

Figure 2- 5: Back-projection method of reconstructing images by solving the EIT inverse problem. It shows two stimulating sources that inject a waveform that penetrates through the medium in a straight line. The resulting boundary potential profile is observed to extract information about the size and location of the black circle anomaly.

The neural-networks approach uses a trained Artificial Neural Network (ANN) to perform image reconstruction given the internal impedance of the object. The ANN goes through a regression process to compute the unknown impedance from a vector of measured boundary potentials. The ANN then undergoes training, which involves using the known input-output samples from the

system to determine the weights to minimize a least-squares cost function. Followed by a classification stage which is similar to the regression stage, however, this time the elements of the output vector are defined for discrete values representing different classes. This process then assigns a specimen represented by a vector of inputs to one of the classes. However, ANN's are most commonly used for ECT systems and do not take measurement noise into account. In addition, large pixels have been used to avoid poor results due to low sensitivity [27].

Consequently, the Sensitivity approach proposed in [28] is implemented in this report, because it accounts for scattering current distributions and allows the use of smaller pixels and high sensitivity.

2.6.2.1 Deriving the Jacobian and solving the EIT inverse problem

The EIT inverse, image reconstruction, problem can be modelled as $\hat{\boldsymbol{x}} = \boldsymbol{B}\boldsymbol{v}$; a linear equation that relates the measured boundary voltages, $\boldsymbol{v}$, to the internal impedance distribution, $\boldsymbol{x}$, using the inverse of a Jacobian matrix, $\boldsymbol{B}$. For time difference imaging, the above equation is applied over a time interval to obtain the change in impedance over that interval. Hence, to compute the impedance distribution within a medium, requires the measurement of the boundary potentials and a Jacobian matrix [18].

For a linearized forward problem, the Jacobian is developed from:

$$\boldsymbol{v} = \boldsymbol{J}\boldsymbol{x} + \boldsymbol{n} \tag{2.7}$$

$$where\ J\ is\ the\ Jacobian\ and\ n\ is\ the\ measured\ white\ noise$$

Each element in the Jacobian can be computed as:

$$J_{i,j} = \frac{\partial v_i}{\partial x_j}, when\ z(t = t_0) = z_0 \tag{2.8}$$

Which shows that each element in the Jacobian relates a change in the measured boundary voltage to the change in impedance at each node inside a finite element model.

However, the impedance and the Jacobian are unknown in the forward problem. Furthermore, suppose the Jacobian was successfully computed, solving the inverse problem becomes troublesome because the Jacobian is not a square matrix and, thus, cannot be inverted by simple algebraic methods. The following methods can be used to invert the Jacobian.

A few suggestions to invert the Jacobian and solve the inverse EIT problem follows:

1. Least Squares Approach: This method aims to minimize the cost function, $||Jx - v||$. Which has the solution:

$$\hat{x} = (J^T J)^{-1} J^T v \tag{2.9}$$

   However, the EIT problem is severely ill-conditioned as there are more unknown conductance's than there are measurable boundary voltages. Thus, the matrix $J^T J$ is rank deficit and cannot be inverted.
   Furthermore, the problem is ill-posed, which means that small changes in the input results in large changes in the output, resulting in an unstable system. Hence, a possible unique solution can be severely corrupted by small errors and noise [17].

2. Singular Value Decomposition: This method provides a way of factoring a non-symmetrical, rank deficit matrix.
   Consider the following decomposition of the Jacobian:

$$J = U\Sigma V^T \tag{2.10}$$

$$In\ this\ decomposition, U\ and\ V\ are\ left\ and\ right\ singular\ vectors\ of\ J$$

$$and$$

$$\Sigma = diag(\sigma_1, \sigma_2, \dots, \sigma_n)\ is\ a\ matrix\ with\ the\ singular\ values\ of\ J\ along\ it's\ diagonal$$

   One major problem introduced by this method, is that the high frequency oscillations in the inverse problem are amplified by small singular values when the Jacobian is inverted. Consequently, noise will be amplified [17].

3. Regularization: This method uses a hyper-parameter which filters the high frequency singular values. Thus, the ill-conditioning and ill-posed problems of EIT becomes null. There are many regularization methods that attempt to maintain continuity of the solution on the data from an ill-conditioned medium. One widely reference method, is the Tikhonov-Phillips regularization method [17]. This method relies on inserting prior information about the system or possible filtered prior data, into the least squares minimization solution.
   In other words, the method attempts to minimize:

$$\hat{x} = arg\min_{x}\left\{\left||Jx - v|\right|^2 + \lambda^2\left||Rx|\right|^2\right\} \tag{2.11}$$

$$Here\ R\ is\ a\ diagonal\ regularization\ matrix,$$
$$\lambda\ is\ the\ hyperparameter$$
$$and$$
$$\lambda^2\left||Rx|\right|^2\ represents\ the\ prior\ information\ about\ the\ impedance\ distribution$$

   This method guarantees a unique solution, provided $\lambda > 0$. The hyper-parameter also controls the trade-off between solution stability and accuracy.

   Commonly, the regularization matrix is the identity matrix or the matrix that corresponds to the first and second difference operators [17].
   From the regularized inverse, the solution to the minimization problem is:

$$\hat{\boldsymbol{x}} = \left(\boldsymbol{J^T J} + \lambda^2 \boldsymbol{R^T R}\right)^{-1}\boldsymbol{J^T v} = \boldsymbol{B v} \tag{2.12}$$

   This equation should be solved iteratively to obtain a non-linear solution when large internal impedance changes is observed.

Furthermore, the method of regularization filters the high frequency singular values of the Jacobian. To see this, consider the following singular value decomposition, with ***R*** = identity matrix [17].

$$\hat{\boldsymbol{x}} = \boldsymbol{J^{-1}v} = \sum_{i=1}^{n} f_i \frac{\left(u_i^T \boldsymbol{v}\right)\boldsymbol{b_i}}{\sigma_i} \tag{2.13}$$

To filter the high frequency singular values, requires the selection of the low-pass filter function:

$$f_i = \frac{\sigma_i^2}{\sigma_i^2 + \lambda^2} \tag{2.14}$$

By selecting this low-pass function, eliminates all singular values that are smaller than the hyper-parameter. These are also the high frequency singular values.

In 2D applications of EIT, Maximum *a Posteriori* (MAP) Regularization is used [17]. It defines the most likely estimate of the impedance distribution given the measured boundary voltages with the aid of statistical information about the medium.

A solution of the following form is then produced:

$$\hat{\boldsymbol{x}} = \left(\boldsymbol{J^T W J} + \lambda^2 \boldsymbol{R^T R}\right)^{-1} \boldsymbol{J^T W v} = \boldsymbol{B}(\lambda)\boldsymbol{v}, \tag{2.15}$$

$$where\ \boldsymbol{v} = \boldsymbol{v}(\boldsymbol{t_{i+1}}) - \boldsymbol{v}(\boldsymbol{t_i}),$$

$$\boldsymbol{R}\ is\ the\ regularization\ matrix,$$

$$and$$

$$\boldsymbol{W}\ is\ a\ data\ weighting\ matrix\ which\ considers\ electrode\ location\ errors\ and\ noise$$

2.6.2.2 Hyper-parameter selection

A hyper-parameter is used to regularize the inverse problem of EIT. It provides a tradeoff between image accuracy and stability, and is selected to preserve as much as possible of the recorded data by applying the least amount of prior information, about the problem, while producing a useful reconstructed image [20]. Common methods used to select a hyper-parameter include Heuristic Selection, L-Curves, Generalized Cross-Validation and the Fixed Noise Figure.

Heuristic selection:

The heuristic selection method involves selecting a hyper-parameter using trial and error. Image reconstructions are observed for several hyper-parameter values and the parameter that produces the best image is selected [17], shown in Figure 2- 6.

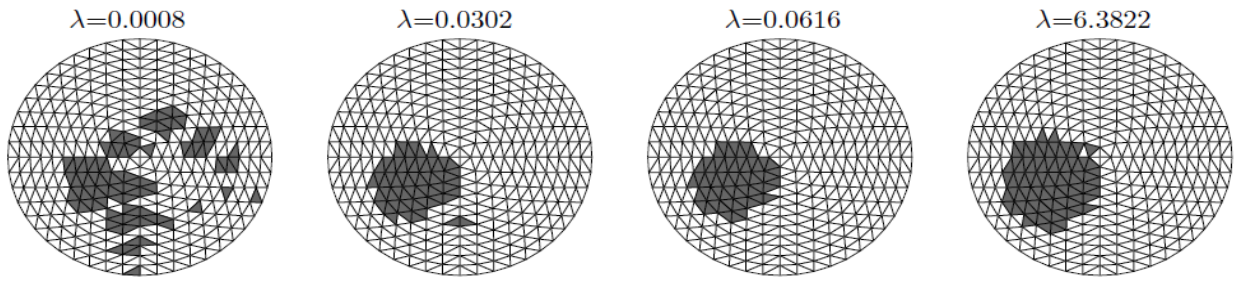

Figure 2- 6: 2D reconstructed images of the evolution of the amount of the anomaly that is detected (dark patches) with an increase in the hyper-parameter [20], lambda.

This method is more labor intensive than the other methods as the process must be repeated for each data set. Currently, there is no known research on specifically evaluating the performance of heuristic selection for one step solutions.

L-curve:

This method plots the semi-norm,$\log_{10}|\boldsymbol{R}\hat{\boldsymbol{x}}|$, versus the norm, $\log_{10}|\boldsymbol{J}\hat{\boldsymbol{x}}-\boldsymbol{v}|$, of the corresponding residual vector parametrically over a range of hyper-parameter values [29]. The resulting plot resembles a L-shape with the optimized parameter located at the corner of the curve, shown in Figure 2- 7.

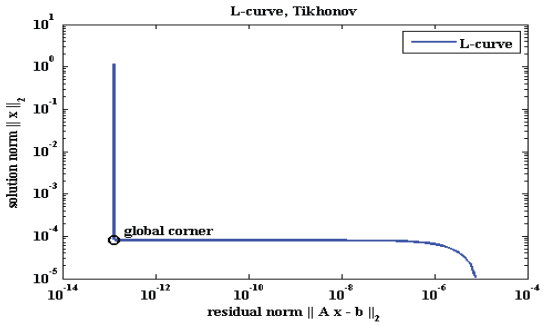

Figure 2- 7: L-curve used to select the best hyper-parameter for the measured data [32]; assuming R = identity matrix, b = voltage and A = Jacobian matrix.

However, this method fails when there is no defined corner of the curve, shown in Figure 2- 8.

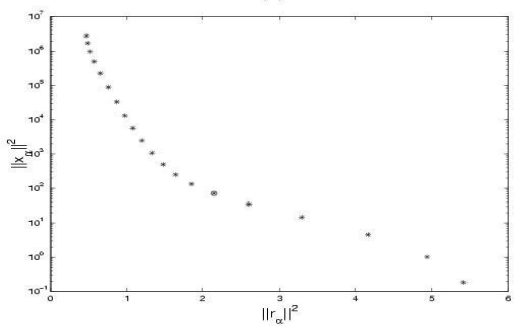

Figure 2- 8: L-curve showing a poorly defined corner. These scenarios make it difficult to confidently select a hyper-parameter [20]; in the image $||r_\alpha|| = ||Jx_\alpha - b||$= residual norm, b = voltage vector, J = Jacobian matrix.

Generalized Cross-Validation (GCV):

This method selects a hyper-parameter that minimizes the GCV function, which predicts a missing arbitrary element in a data set [30]. The GCV function is shown below.

$$GCV(\lambda) = \frac{\left||\boldsymbol{J}\hat{\boldsymbol{x}} - \boldsymbol{v}|\right|^2}{trace(\boldsymbol{I} - \boldsymbol{JB})^2} \tag{2.16}$$

Here $\hat{\boldsymbol{x}}, J, \lambda \; and \; B$ were defined in the previous section and I is the identity matrix. One advantage of this method is that no prior information is needed about the error norm.

Fixed Noise Figure (FNF):

This method is based on the noise figure calculation [31] which is defined as the signal to noise ratio in the measurements to that of the reconstructed image for an inhomogeneity placed at the center of the medium.

$$FNF(\lambda) = \frac{SNR_{in}}{SNR_{out}} \tag{2.17}$$

In this case the FNF is selected by the user and by using a bisection search technique, the hyper-parameter can be selected.

2.7 EIT system design

EIT has a wide variety of applications from detecting and monitoring breast cancer and brain functioning to monitoring fluid flow in pipes. Consequently, there are several studies that propose different EIT system designs that tackle individual applications of EIT; these are discussed later. Nonetheless, most of these designs follow a similar design path; signal injection through signal source electrodes placed on a test tank, followed by data acquisition at the remaining electrodes (measuring the boundary potentials). These measurements are then transmitted to a computer for further analysis. These data are processed on the computer and the result will be used to update a FEM model of the subject. Once the solution converges, an image will then be produced from the mapping of the subject's internal impedance distribution.

This section reviews several pieces of literature that deal with the practical design of an EIT system.

A typical low cost EIT system design flow has the following layout:

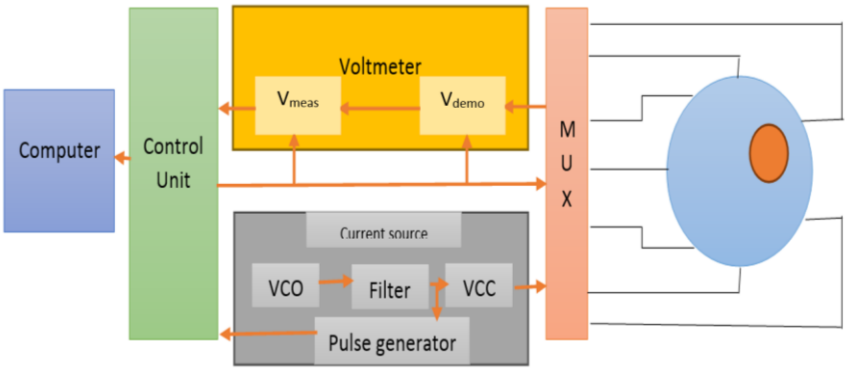

Figure 2- 9: Block diagram of a typical low cost EIT system

Figure 2- 9, above, shows that a typical low cost EIT system is made up of:

1. A VCCS (Voltage-Controlled Current Source) with an optional built in VCO (waveform generator), filter and VCC (Voltage-to-Current Convertor) to supply the current through a single pair of electrodes.
2. A multiplexer to supply the current through a selected pair of electrodes and to select the electrodes of which to measure the potentials from the remaining electrode pairs.
3. A voltmeter which demodulates the voltage.

A few practical factors that need to be considered are that the VCC requires stability and high precision [32] and to achieve this, one should build a VCC with a high output impedance, linear voltage to current conversion, precise output waveform and optimal performance over a wide range of frequencies. Also, the current should be alternating at various frequencies for a multi-frequency system, hence a sinusoidal waveform should be generated using a waveform generator that has an accurate output waveform, a low output impedance, a wide bandwidth and a steady amplitude throughout the frequency range [1]. Typically, EIT operates over the frequency range from 1 kHz to 1 MHz [33], thus the circuit should ideally be built to operate over this range with enough support to work on a 10 kΩ load. Likewise, the output impedance of the current source should be greater than the expected load.

In addition, the measured potential at any instant appears across two adjacent electrodes and before the boundary potentials are measured, one should begin demodulating (using differential synchronous demodulation) the potential [32]. The demodulation stage attains sampled data from the multiplexer and prepares the electrode voltages for measuring, using an analog-to-digital converter. The analog-to-digital convertor then transmits the sampled data to a microcontroller which forms the control unit. Furthermore, the multiplexer should be selected to have high speed operation with the same number of output pins as the number of boundary electrodes.

A few related works on EIT system design

1. Z. Zhou et.al proposed a telemedicine system based on EIT and the result was a fast and portable system. The final proposed system has the potential to be a monitoring device for out-of-hospital patients and in ambulance vans. The system provides the operator with the benefit of operating in two different modes – diagnosis and medical. A cloud storage technique is used to store the medical data and the diagnosis mode uses 3G communication and voice broadcasting. To perform digital signal processing and data transfer via a third generation (3G) network, a Field Programmable Gate Array (FPGA) chip was used. Furthermore, to provide portability of the device, two lithium batteries were used [34].

2. Alzbeta Elizabeth Hartinger et.al developed an EIT system that included a hand-held probe with 16 semi-invasive electrodes. This system was designed to target early diagnosis of skin cancer. A FEM model was developed and the electrical behavior of the skin was studied in order to understand and discriminate the operating frequencies of

benign and malignant lesions. Research concluded with great opportunities by revealing an improved resolution and a decrease in the image artifacts by 70 % [35].

3. Tushar Kanti Bera et.al developed a multi-frequency EITS for biomedical imaging. Research included practical tests on practical phantoms made from a salt solution and vegetables (to provide non-homogeneity). EIDORS (Electrical Impedance Tomography and Diffuse Optical Tomography Reconstruction Software) was used to efficiently reconstruct the images from the measured data [36].

4. Deepti Garg and Vikas Goel designed a system that comprised of electrical circuitry to obtain data signals from the surface of the subject (the arm). After acquiring the data, the image was then reconstructed using direct and iterative methods. Research concluded by stating that the human body impedance varies in the range of 0.7 kΩ to 1 kΩ. The accuracy of the system depended upon the constant applied current and a reference resistance source. The images were successfully reconstructed using the MATLAB EIDORS toolbox and the method of imaging was non-invasive and rejected any effects of radiation. The reconstructed images were validated from the original shape of the arm [32].

In addition, several considerations about the individual components of the EIT system follows. Foremost, all electronics that make up the EIT system should be placed close to the source, and common ground should be used to avoid leakage currents. Moreover, leakage currents are also introduced through parasitic circuit components.

With regard to the type of injection current (if current is chosen to be the stimulating signal) some systems use single ended current injections and a common ground electrode [6], floating current sources, multiple fixed position sources and mirrored sources [1]. In all cases, a voltage is first established, using oscillators or signal generators, and sent to a voltage controlled current source which supplies a constant current through a pair of electrodes, irrespective of the internal impedance change of the medium. The most common VCCS is the modified Howland circuit [1]. Furthermore, systems that use single floating sources require to be multiplexed to each driving electrode pair. This is done by using a multiplexer. The requirements of the multiplexer is adequate speed, no loss in transmission and the number of channels must be twice the number of injection patterns; one to source and another to sink the current.

With regard to the type and configuration of electrodes, copper or stainless steel electrodes are commonly used due to their high conductivity and low cost [37]. Stainless steel is preferred due to its strong anti-corrosion properties. Silver electrodes have also been used in biomedical applications [38], however, the cost of these electrodes are too high for the prototyping stage. Moreover, to avoid injecting harmful metal ions into a patient, alternative electrodes are made of carbon [1], [39]. Furthermore, some papers share electrodes for stimulation and measurement [40], while other papers use separate electrodes [2], commonly using compound electrodes, for each purpose to reduce the contact-impedance. For compound electrodes, the center, ideally point electrodes are used to measure the potentials while the larger electrodes are used to inject currents. Compound electrodes have been shown to provide good current distribution through the medium and accurate voltage measurements [41]. Furthermore, the size of the electrodes is an important factor to improve current distribution and to limit electric field distortion.

Furthermore, some papers use a saltwater solution to form a homogeneous environment within the test tank and using an inhomogeneity of impedance close to that of the saltwater solution, to form a well representation of a biomedical specimen and to guarantee that the system remains fairly linear [15], [26], [36]. This allows one to use a one-step reconstruction algorithm, which reduces reconstruction complexity and time.

With regard to the voltage measuring end of the system, the difference in voltage between two electrodes is measured and scaled to reduce the large voltage ranges associated with single boundary voltage measurements [6]. For this action, instrumentation amplifiers are used because they have large input impedances which block any current from exiting through the measuring electrodes, causing leakage currents.

After measuring the boundary potentials, the potential should be converted to a digital format to allow for further digital computations and image reconstruction. This is done by using an analog-to-digital circuit which takes samples of the measured signal and transmits these data to a digital controller. Consequently, careful attention should be placed upon recording a sufficient number of samples to accurately extract the amplitude and phase shift (amplitude location) of the measured signal.

2.8 Performance figures of merit

A good measure of the performance of an EIT system is to compute different errors in the system. To observe the spatial qualities of the reconstructed images, requires computing the difference between the reconstructed image and the actual nonhomogeneous case. These differences can be grouped into the size error, position error and noise error ratio for a given anomaly inside the phantom [6], [42]. Furthermore, the errors in the reconstructed images are caused by the type of reconstruction algorithm and the errors in the hardware.

2.8.1 System hardware performance

To test the performance of the hardware requires the measurement of:

Signal to Noise Ratio (SNR) and Noise Error Ratio (NER):

The SNR is computed as:

$$SNR_i = \frac{mean(v)_i}{sd(n)_i} \tag{2.18}$$

The SNR (SNR_i) for a given measurement channel (i), is the ratio between the mean of the measured signal ($mean(v)_i$) and the mean of the noise ($sd(n)_i$) on the same signal channel. An adequate estimate of the mean of the noise in the measured data frame, is the standard deviation of that frame [43]. An SNR > 0dB means that there is more signal than noise. Furthermore, for an EIT problem, minimum SNR constraints are placed upon the system design. This is based on the minimum impedance that the system is required to measure. After establishing this constraint, one can then compare the SNR for different measurement frames to this constraint to show that the system adheres to the design.

Additionally, the noise error ratio (NER) is defined as the inverse of the SNR, [6]. The NER must be a small value to show that the noise level is significantly lower than the measured signal. In this paper, small refers to any value less than 20 %, which corresponds to a SNR > 14 dB.

System measurement accuracy:

The measurement accuracy of a system is the smallest change in the internal impedance distribution of the object, which the system can detect [6]. In the author's opinion, the system measurement accuracy is computed by observing the minimum voltage that can reliably be measured for a selected current amplitude. A threshold is applied to the measured data to extract only the measurements that lie outside of the expected noise level of the system, and this threshold gives the minimum voltage that the system can reliably measure. Furthermore, using Ohms law, the minimum resistance that the system can detect is computed. This is replicated using the amplitude and frequency of the applied current and measured potential signals to compute the minimum impedance.

Other methods for computing this quantity is to directly measure the impedance of an anomaly, place it into the phantom and observe the impedance of the anomaly in the reconstructed image data [44]. However, this method requires repetitive labor whenever an anomaly, having a different impedance distribution, is inserted into the phantom. This method itself produces errors as the exact accuracy of the system is not accurately measured.

System symmetry:

To observe the symmetry of a system, requires reconstructing images of anomalies that are placed, opposite each other, at equal distances from an axis of symmetry [6]. The reconstructed image of an anomaly, placed at a certain position, should be the mirror image of that which is produced when an anomaly is placed diametrically opposite the first position, for an ideal system. However, practical systems have electrode position errors and the manual positioning of an anomaly could all cause a system to appear to be unsymmetrical. In the author's opinion, to test the symmetry of a system, is to compare the position and size errors of the reconstructed images for anomalies that are placed diametrically opposite one another. Another method for observing the systems symmetry, is to compute the amplitude response (AR) of the system. The AR is computed by subtracting the mean pixel value of a given image from each pixel and dividing the result by the standard deviation of all pixels in the image [43]. The AR for one image is then compared to that of another image, when an anomaly is placed in the mirror position.

Low Frequency Drift (LFD):

The low frequency drift of the system, is the observed drift of a measurement frame, of the measured signal's amplitude and offset when a DC signal is injected [6]. This is usually caused by ionization and polarization in the medium, temperature and hardware properties [45]. One way to eliminate LFD, is to reduce prolonged measurement times.

Measurement Frame Rate (MFR):

The measurement frame rate of a system is the total time taken to measure the voltages at all measurement electrodes until current has been injected through all possible injection electrode pairs for a given current injection pattern. Reducing the MFR also reduces the LFD, at the increased cost of fabricating a fully parallel system.

2.8.2 Image Reconstruction (IR) performance

The IR performance of a system is a measure of how close the reconstructed images resemble the actual nonhomogeneous case. This includes how well the size, position and shape of the anomaly is preserved in the image. The following figures of merit are used to estimate the IR performance of a system.

Position Error (PE):

The PE refers to the error between the actual and reconstructed image positions of an anomaly, at a selected position in the phantom [42]. It is computed as:

$$PE = r_{recon} - r_{actual} \tag{2.19}$$

Here, $r_{recon} - r_{actual}$ is the difference between the radial distances to the center of the actual anomaly and the anomaly in the reconstructed image. However, a more useful measure of the position error, is to compare this difference to the radius of the test tank, r_{tank} , shown below.

$$PE[\%] = \frac{|r_{recon} - r_{actual}|}{r_{tank}} \; x\,100 \tag{2.20}$$

Size Error (SE):

The SE refers to the difference in diameter of the reconstructed image anomaly to the actual case [42]. In a similar way to computing the PE, here, the difference between the diameters of the anomalies are divided by the diameter of the test tank, as shown below.

$$SE[\%] = \frac{|d_{recon} - d_{actual}|}{d_{tank}} x100 \tag{2.21}$$

Distinguishability:

Distinguishability refers to the ability of the system to distinguish between several anomalies, placed inside the phantom, which could have different impedance distributions, shapes or sizes [6]. To quantify this performance merit requires computing the level of shape deformation, size error, position error and measured impedances. Alternatively, knowing the size and position error and *observing* that the shape of the anomaly in the reconstructed image is close to the shape of the actual object is adequate information to conclude that the system is able to distinguish between different anomalies.

Ringing:

Ringing is the evidence of artefacts in the reconstructed image that have an opposite polarity to the anomaly [42]. It is caused by the reconstruction algorithm and the hardware. In this paper, to remove ringing that is caused by the hardware of the system, requires the use of thresholding.

Detectability:

Detectability is a measure of the smallest change of impedance that can be detected by the system [6]. Furthermore, knowing the systems measurement accuracy already presents this information. Other papers suggest that detectability is a measure of how well the reconstructed images are able to detect an anomaly [6]. However, this definition of detectability is similar to that of distinguishability, which means that once the system can distinguish between several anomalies, then it is reasonable to conclude that the system is able to detect several anomalies.

In addition, if several anomalies can be detected, then intuitively, a single anomaly can be detected.

Repeatability:

Repeatability refers to the ability of a system to produce repeatable measurements, at different instances, which are used to produce identical images. To observe this, requires taking several measurement frames for a selected anomaly position, and reconstructing images thereof. How well these images resemble each other, gives an indication on the repeatability of the system.

Furthermore, the methods for measuring different performance figures of merit for the EIT system, were discussed. In addition, there are other methods to test the performance of a system; such as the anomaly impedance error, which is the difference between the impedance measured in the image and the actual impedance of an anomaly. However, those methods do not provide relevant information for the designed prototype and the research questions in this paper, and are not widely used.

2.9 Summary

Solving the 3D EIT problem requires a large number of finite elements in the model to accurately detect anomalies; resulting in increased storage constraints. Alternative methods of imaging, 2.5 D EIT imaging, solves the 3D equation by employing a 2D model and solving a smaller number of equations [46]. However, at the start of this investigation, injecting current using two stimulation patterns successively, in order to increase the number of reliable and orthogonal measurements, was not investigated; from the author's knowledge.

In all dimensions of EIT (2D, 2.5D and 3D), the spatial resolution is greatly improved by increasing the number of electrodes around a single plane. In contrast, drastically increasing the number of electrodes requires a reduced electrode contact area, which results in increased electrode-skin contact impedance with a reduced electric field intensity [47]. Wider electrodes create a higher electric field intensity and reduced contact impedance, thus, improved sensitivity. However, an electrode surface area that is too large will create a distorted electric field because it becomes increasingly difficult to keep the entire electrode at the same potential when a small boundary

potential is expected. As a result, intuitively, a large electric field distortion results in the degradation of the reconstructed images.

In this chapter the current state of the art of Electrical Impedance Tomography was reviewed. First the different modalities of electrical tomography, ERT, ECT and EIT were discussed. This discussion included common system configurations, modality advantages and disadvantages and the respective applications. The subsequent section covered computations of an impedance which led to the problems and limitations of EIT. The problems of EIT were found to be its ill-posed and ill-conditioned nature, which refers to the problem of computing a matrix of the internal impedance distribution of an object given far fewer boundary potential measurements, which results in an unstable solution because the solution does not continuously depend on the measured data. This showed that there is no one-to-one relationship between known (or measured) and unknown (or computed) data. The limitations of EIT were found to be the signal constraints for various applications (require a current amplitude <= 1 mA with frequency in the range 1 kHz-1 MHz) and the size and number of electrodes (which limits the spatial resolution). The next limitation was that of scattered current throughout the medium which limits the current density. Subsequently, the forward and inverse problems of EIT were addressed. The forward problem refers to using an initial estimate of the internal impedance of the object with the known injection current, to compute the boundary potentials for these initial conditions. From this information, a sensitivity matrix is computed by observing how the voltage changes with a change in impedance at the nodes of the elements in a finite element model of the EIT problem. Furthermore, the inverse problem involves inverting the sensitivity matrix. This inverted matrix is then multiplied with the measured boundary potentials to get the estimated internal impedance distribution of the object; for a linearized EIT problem. Following this, an image can then be reconstructed using an available image reconstruction software. Subsequently, common EIT system configurations were explored, while outlining the importance of each system component and any common pitfalls associated with these systems. The final section outlined a few performance figures of merit that have been used to quantify the performance of an EIT system.

3 Proof of concept simulations

From extensive literature review, it is found that most EIT systems employ a single current stimulus pattern. The most common are adjacent, perpendicular and opposite injection patterns [1]. For each of these patterns, the current density changes and the localization of one pattern can be superior to another for a given region in space. Some patterns provide a high current density near the boundary of the test tank, and systems that employ this pattern will have good localization of anomalies that are near the boundary [12]. However, as the anomaly is placed closer to the center of the tank, the system is observed to have poor localization due to a reduction in the current density, the further the anomaly is moved away from the boundary.

Other patterns may enhance localization at the center of the tank by increasing the current density in that region. However, increasing the current density in one region results in a reduction of the current density in another region. Hence, there is no single pattern that provides a uniform current density throughout the medium. Therefore, it is intuitive to assume that a combination of these current patterns (a dual current stimulation protocol) will provide a more uniform current distribution.

To provide a proof of the concept of Dual Current Stimulation (DCS) EIT image reconstruction, a systematic approach is taken. Starting with a few simulations that are provided with a discussion on how well the dual method is expected to compare with single plane stimulation methods. It should be noted that a dual stimulation protocol was not available on the chosen software platform (MATLAB/EIDORS). Consequently, adequate proof of concept is to show that cross-plane current injections provide the ability to detect anomalies that are placed at positions where a single plane current stimulation pattern fails to accurately detect. One could infer that the DCS method, which employs both stimulation (in- and cross-plane) patterns, will inherit the detection advantages from both stimulation methods, and that improving the detection capabilities, which reduces errors in the reconstructed images, means that the spatial resolution and image quality has been improved.

3.1 Single plane source current injection protocols

The method used to inject current into a medium affects the system's sensitivity. There are three typical current injection protocols [12]. The first method injects current at all electrodes while simultaneously measuring the boundary potentials; systems that use this method employ electrodes with the configurations shown in Figure 3- 1 (a). However, this method suffers from high electrode-skin contact impedances. The second method injects current at a single pair of electrodes, while measuring the potentials at the remaining electrodes; systems that use this method also use electrodes with the configurations shown in Figure 3- 1 (a). Consequently, the number of measurements is reduced to avoid injecting and measuring at the same electrode. The third method uses compound electrodes, which allows one to separate current injection electrodes from the potential measuring electrodes; systems that use this method employ electrodes with the configurations shown in Figure 3- 1 (b). The third method removes the effect of contact impedance, compared to the first two methods, with an increase in system flexibility and independent current injection and voltage measurements.

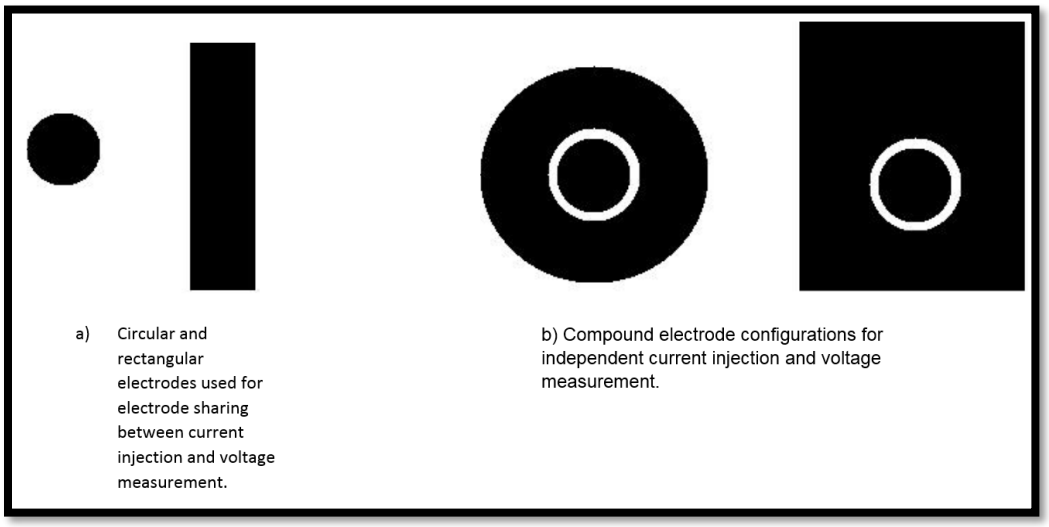

Figure 3- 1: Shows different electrode configurations [6].

Different injection patterns will be used to reconstruct an image of a two-anomaly plane, shown below:

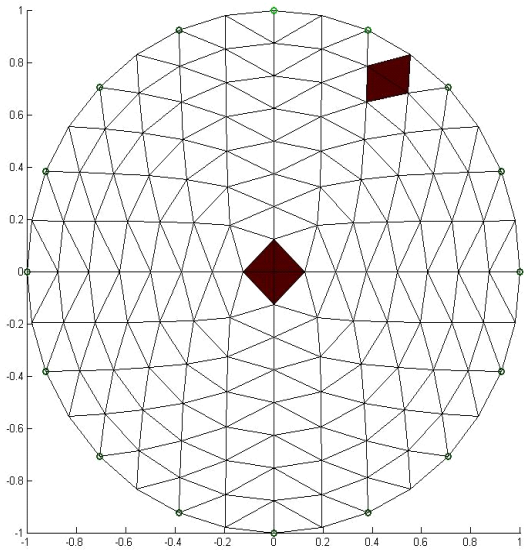

Figure 3- 2: 2-Anomaly plane to be reconstructed. The impedance of these anomalies were selected to be twice that of the homogenous background to ensure that there are no large changes in impedance within the medium.

Figure 3- 2 above needs to be reconstructed, using the noser-prior filter and the one-step Gauss Newton algorithm; several filter methods (Gaussian High Pass Filter, Laplace Prior Filter, Total Variation, etc.) were tested and this filter provided the best results based on reduced ringing, speed of reconstruction and anomaly detection. Two anomalies were used; one near the boundary and the other at the center of the tank to expose the limitations of each stimulation pattern.

Furthermore, both anomalies had equal impedances which were different (double the magnitude) to the homogeneous medium and the amplitude of the stimulation current was set to 1 mA.

The following current patterns are typically employed on a compound electrode system.

3.1.1 Adjacent current injection patterns

When using the adjacent current stimulation pattern, current is injected through two adjacent electrodes, while the boundary potentials are measured simultaneously at each electrode pair within the plane (for a compound electrode system). Because the current electrodes are independent to the potential measuring electrodes, the current is injected in the next adjacent pair of electrodes while the potentials are simultaneously measured. This continues until current has been injected through each possible adjacent current electrode pair (format of adjacent current pairs for a 16 electrode system (source electrode, sink electrode): (0, 1), (1, 2), (2, 3), (3, 4), … (15, 1)).

When applying an adjacent current stimulation pattern to the two-anomaly plane, the following image was reconstructed:

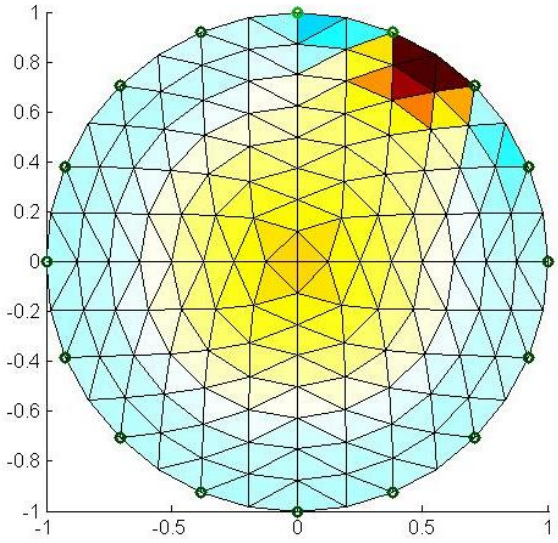

Figure 3- 3: Reconstructed image using an adjacent current drive pattern

Figure 3- 3 above shows, using adjacent current stimulation patterns, that only the boundary anomaly is detected. This shows that adjacent stimulation does not work well for systems that have several anomalies, with one being at the center. This result is warranted in [1], [12]. In contrast, it was observed (shown in Figure 3- 4) that, using the adjacent stimulation pattern, center anomalies can be detected if only one anomaly is placed in the homogeneous medium (i.e.

removing the boundary anomaly in Figure 3- 2). However, the reconstructed image still presents large size errors for center placed anomalies, because the current density is weakest at the center of the medium. Hence, the regions of weak current distribution are treated as anomalies of high conductance; making it more difficult for current to penetrate.

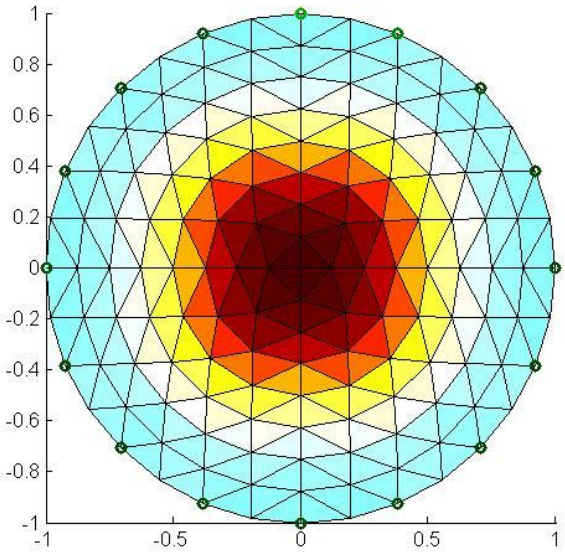

Figure 3- 4: Reconstructed image, of a single center placed anomaly, using an adjacent current drive pattern

A few advantages of using an adjacent current stimulation system includes reduced contact impedance, minimal hardware, high sensitivity to objects near the boundary and perturbations in the boundary geometry [1].

3.1.2 Diametrically-opposite current injection patterns

When using the diametrically-opposite, or opposite, current stimulation pattern, current is injected through electrodes that are spaced 180 degrees apart (format for opposite current pairs for a 16 electrode system (source electrode, sink electrode): (0, 8), (1, 9), (2, 10), (3, 11), … (7, 15)), which is commonly used to monitor brain function [1]. As with adjacent stimulation, the potentials are measured at each potential-measuring electrode pair within the plane. This process is repeated until current has been injected through all possible diametrically opposite current electrode pairs.

When applying an opposite current stimulation pattern to the two-anomaly plane, the following image was reconstructed:

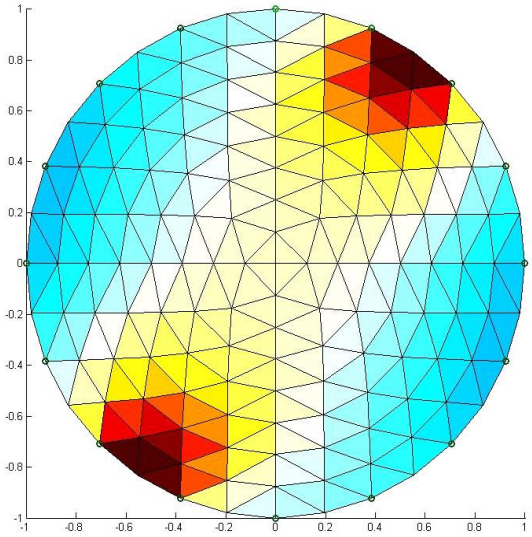

Figure 3- 5: Image reconstruction using 180-degree current stimulation patterns

Figure 3- 5 above shows, using an opposite current stimulation pattern, that again, only the boundary anomaly was detected. However, an additional problem of ghosting is introduced; where the anomaly at the boundary is mirrored about the center line [12]. This result is warranted in [1], [12]. Furthermore, intuitively, ghosting does not present itself when a single anomaly is placed at the origin, shown in Figure 3- 6. This is due to the fact that placing an anomaly at the origin, which is on all axes of symmetry, will not have a mirror image because the mirror of an anomaly at the origin does not exist in a 2D plane.

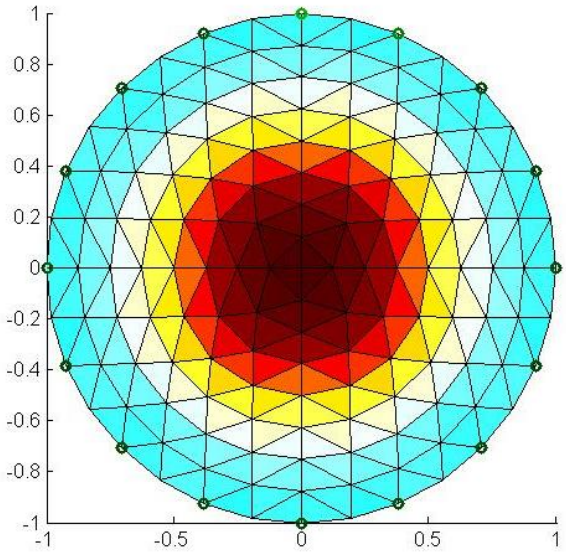

Figure 3- 6: Image reconstruction, of a single center placed anomaly, using 180-degree current stimulation patterns

Figure 3- 6 above shows the reconstructed image, using the opposite current stimulation pattern, for a center placed anomaly. As with the adjacent stimulation example, the opposite stimulation method is able to detect an anomaly that is placed in the center of the medium. However, the image shows large size errors.

3.1.3 Perpendicular current injection patterns

The perpendicular current stimulation method injects current through electrodes that are spaced 90 degrees apart. As with the first two methods, here the process is repeated until current has been injected through all possible electrodes that are spaced 90 degrees apart, within the same plane (format for 90-degree current pairs for a 16 electrode system (source electrode, sink electrode): (0, 4), (1, 5), (2, 6), (3, 7) … (15, 3)).

When applying a 90-degree current stimulation pattern to the two-anomaly plane, the following image was reconstructed:

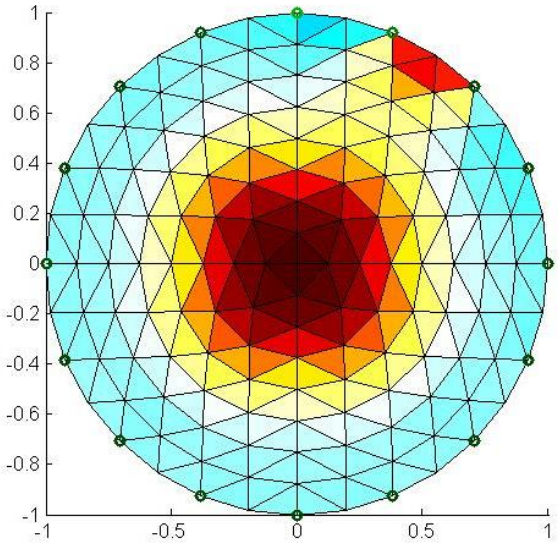

Figure 3- 7: Image reconstruction using 90-degree current stimulation patterns

Figure 3- 7 above shows, using a 90-degree current stimulation pattern, that both anomalies were detected with minimal anomaly size and position errors (concluded by inspection). Further observation, by inspection, is made that the 90-degree stimulation has an enhanced overall sensitivity compared to the first two methods; which is warranted in [12].

From the presented current patterns, the perpendicular method provides enough current density near the boundary to notice that there is an anomaly at the boundary between electrode 2 and 3 (1 o' clock), and a high current density at the center. In addition, the reconstructed image for a center placed anomaly, shown in Figure 3- 8, presents fewer reconstruction errors compared to the first two stimulation methods. Therefore, the perpendicular current injection pattern is selected as the initial current stimulation pattern.

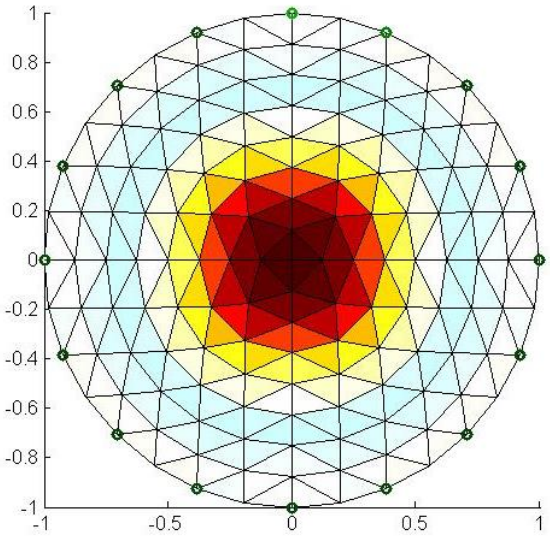

Figure 3- 8: Image reconstruction, of a single center placed anomaly, using 90-degree current stimulation patterns

In addition, these images were reconstructed using simple reconstruction methods. It is then intuitive to assume that using a more advanced reconstruction method such as the iterative Gauss-Newton method could indeed improve the detection capabilities of each system, which improves localization near the boundary and at the center, for all current patterns. However, the 90-degree stimulation pattern will still provide the best overall sensitivity, when using single plane stimulation.

After observing the reconstructed images for a perpendicular current injection pattern, it is evident that more current density is needed near the boundary. However, suppose the current injection electrodes are hardwired to source and sink current perpendicularly and to improve system symmetry. Then a second pattern cannot share electrodes with the first pattern. Furthermore, if there was a way to incorporate a second pattern, then the adjacent stimulus pattern would be deemed an adequate second pattern to improve localization at the boundary. Additionally, the dual system is then expected to have an improved spatial resolution as compared to a single stimulation method.

Moreover, for a finite element model (having triangular elements of equal cross-section) and using 256 independent boundary voltage measurements in a frame and a test tank of diameter equal to 15 cm, results in a spatial resolution of 0.69 cm^2. Therefore, to increase the spatial resolution, more independent measurements need to be taken, to introduce new data. This can be done by

increasing the number of electrodes in an electrode plane. However, increasing the number of electrodes, reduces the electrode contact area, which affects the depth of current penetration in the medium [1]. Thus, the electrode size should not be reduced while a second current injection pattern needs to be established.

3.2 Incorporating a second stimulus pattern

This section aims to find a way of incorporating a second stimulus pattern that resembles the adjacent stimulation pattern. Using a systematic approach, the opposite current injection method is considered. From the previous section, it is evident that ghosting occurs when an anomaly is located at any position other than the origin. Ghosting does not occur when an anomaly is placed at the origin because the anomaly is placed on the center of all possible axes of symmetry, hence, a mirror image will not be formed.

Furthermore, suppose the two-dimension problem is observed in three dimensions as shown in Figure 3- 9.

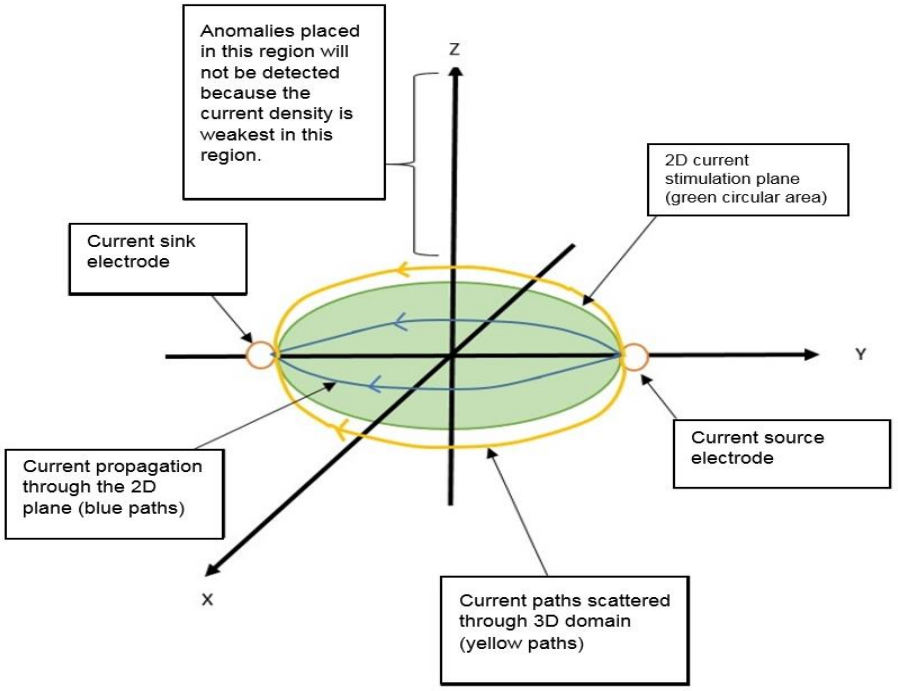

Figure 3- 9: Shows three dimensional view of the two dimensional problem. It shows that the injected current is not confined to the xy-plane. This is used to introduce the second current stimulus pattern.

In Figure 3- 9, placing an anomaly at the origin in the xy-plane removes ghosting, and by using the current pattern that is distributed along the z-axis, it is then possible for one to place an anomaly at any point along the z-axis without the concern of ghosting. The same current density limitations that are present in the single injection methods in a 2D plane, are present in this three-dimensional space. One limitation in particular, as shown in Figure 3- 9, is that the further an anomaly is placed from the origin, along the z-axis, the less chances there are of detecting it, because the current density reduces the further the object is moved from the source; which is in the xy-plane.

Furthermore, in Figure 3- 9, it becomes evident that the xy-plane observes the opposite current injection pattern, but the yz-plane observes a different pattern. Intuitively, increasing the distance between sink and source electrodes will reduce the area over which anomalies cannot be detected, by increasing the current density further from the origin along the z-axis (this is limited by the source strength). In a similar manner, reducing the distance between these electrodes will provide an increased current density for z-positions that are close to the origin. This shows that the xy-plane observes an opposite injection pattern, but the yz or xz-planes will observe an adjacent current pattern. The plane in which one measured the boundary potentials is the plane that observes a current pattern. Hence, measuring along the yz-plane will result in a system that observes an adjacent current pattern.

Following this, the next step involves flipping and rotating the three-dimensional coordinate system and incorporating the boundary of a test tank to limit the z-axis from zero to the diameter of the test tank as shown in Figure 3- 10.

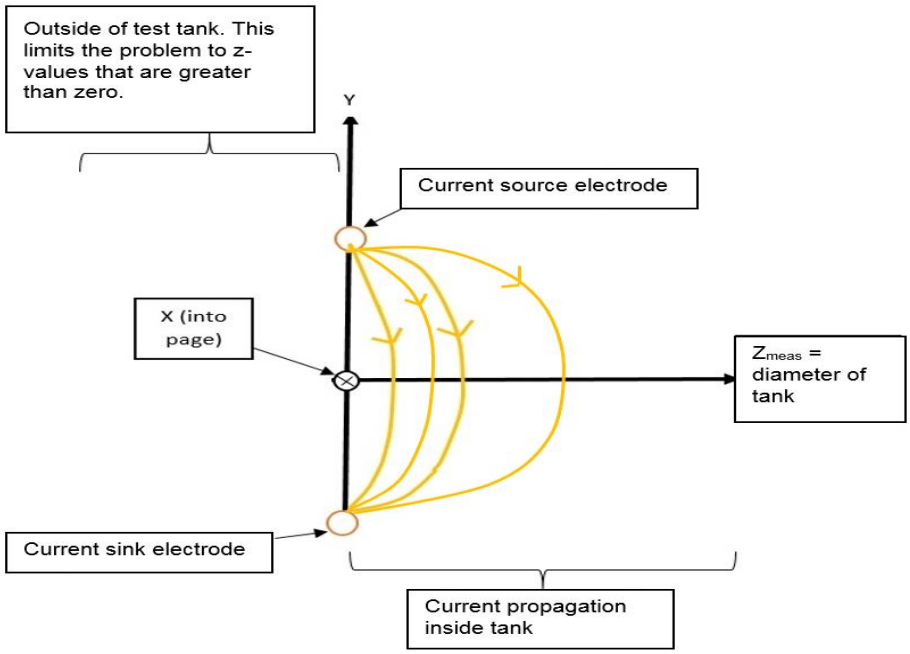

Figure 3- 10: Shows the yz-plane. The z-axis is limited by the boundary of the tank and the drive electrodes are placed vertically opposite each other. It further shows that the current pattern within the tank has a high current density near the origin.

Figure 3- 10 shows that the current is distributed through the test tank. Furthermore, as long as an anomaly is placed perpendicular at any position on the limited z-axis, no ghosting will occur, given that the boundary potentials are measured along the boundary of the test tank which is the xy-planes origin for each subsequent vertical or cross plane injection pair.

From this discussion, it is concluded that two electrode planes are needed in addition to the plane that is used to measure the boundary potentials and inject a current perpendicularly. One plane will be placed above the measuring plane and the other is placed at an equal distance below the measuring plane. From here onwards, the measuring plane will be referred to as the center plane, and the other planes are referred to as the cross planes.

3.3 Cross plane current injection method

To this point, it was decided that the source and sink current electrodes will be perpendicularly spaced apart within the center plane of the test medium. This type of stimulation has a high current density near the center of the medium and weaker near the boundary, hence, for small conductivity changes within the medium, 90-degree stimulation can accurately detect objects that are placed near the center of the medium. Consequently, for the second stimulation protocol, the cross plane stimulation protocol should have the advantage of being able to detect anomalies along the boundary. For this reason, the current will be sourced through an electrode in the top plane and sunk through an electrode in the bottom plane directly below the source electrode. This results in adjacent current stimulation properties, as observed by the center plane. This was shown to have a high current density near the boundary and weaker near the center of the medium, thus, being able to accurately detect anomalies near the boundary. This section provides simulations to corroborate with the theory presented in the previous section.

Below is a model of a tank which has three planes of 16 electrodes each.

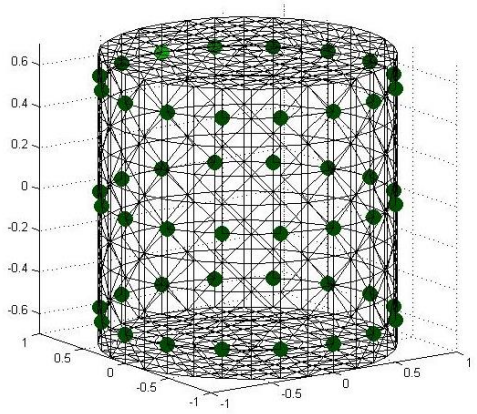

Figure 3- 11: The image shows a model of the test cylinder. Anomalies will be placed within this cylinder to observe that the system can indeed detect objects at the boundary and at the center of the tank.

The model, in Figure 3- 11, has two stimulation patterns; 90-degree center plane and vertical cross-plane stimulation, which was achieved by altering the EIDORS stimulation libraries. An anomaly was placed at the center of the tank, as shown in Figure 3- 12 below.

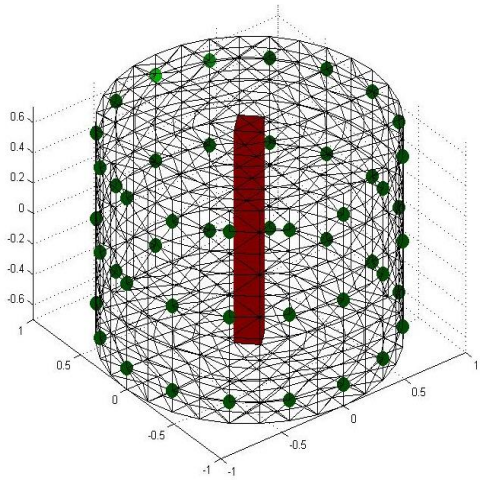

Figure 3- 12: Anomaly placed at the center of the test tank.

The reconstructed slices per plane of the tank above, containing a centered anomaly, is shown in Figure 3- 13 below.

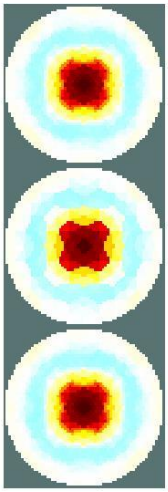

Figure 3- 13: Slices of the reconstructed image, when an anomaly was placed at the center of the tank.

In Figure 3- 13, the middle slice provides the sharpest image. This is due to injecting current at 90-degrees in the center plane. Hence, the current density is highest near the center of the cylinder in the center plane. For this reason, the anomaly was accurately detected in this plane.

Subsequently, an anomaly was placed near the boundary of the tank, as shown in Figure 3- 14 below.

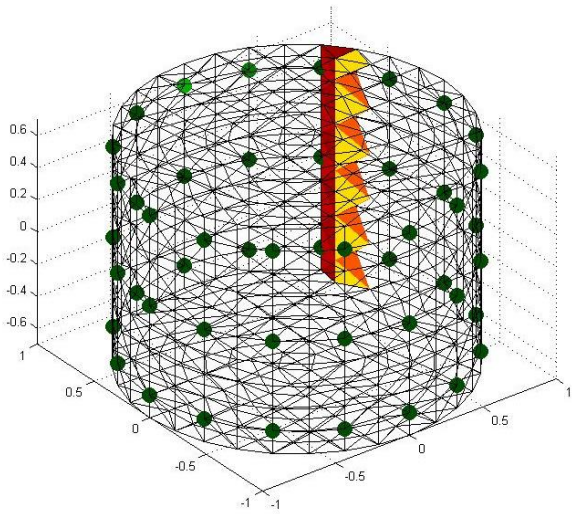

Figure 3- 14: Cylinder with anomaly placed at the boundary of the tank.

The slices per plane of the anomaly position, in Figure 3- 14, is shown in Figure 3- 15 below.

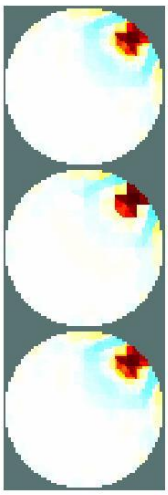

Figure 3- 15: Slices of the reconstructed image of a tank with an anomaly near the boundary.

From the slices in Figure 3- 15 and Figure 3- 13, it is intuitively assumed that the Dual Current Stimulation (DCS) method is able to detect anomalies at all points within the test cylinder, as it is able to detect anomalies at the two extremes; namely at the boundary and at the center of the cylinder in the measurement plane. This is a reasonable assumption to make, because a system that can detect anomalies at extreme locations within the cylinder, will indeed be able to detect anomalies at any location between these extremes. As such, further research can commence to observe the physical realization of the DCS protocol.

Furthermore, a solution to ensure that the system is able to detect anomalies at any random position, is to use a more advanced reconstruction algorithm. A few algorithms were considered and tested. However, some advanced algorithms were observed to require significantly more memory and CPU processing speed and others introduce ringing in the pixel values. It is therefore advantageous to formulate a method, which deals with improving the physical system prior to image reconstruction, to improve the system's distinguishability using a simple reconstruction algorithm.

Moreover, a DCS EIT system is expected to have a frame of 512 voltage measurements, which is double that of the single plane stimulation protocol. Therefore, an EIT system that has a test tank of diameter equal to 15 cm, will have a spatial resolution of 0.35 cm^2; if all triangular elements of the FEM model are equal. Thus, a DCS EIT system is expected to improve the spatial resolution, compared to single plane stimulation EIT, by 50 %; based on the spatial resolution computation previously executed. This means that the size and position errors in the reconstructed images from the DCS EIT system is expected to be half that of the single plane stimulation EIT system.

3.4 Summary

It was shown that increasing the distance between current injection electrodes provides a deeper current penetration through the medium, and increasing the number of electrodes extends the measurement times and improves the image quality, by increasing the number of independent data. Hence, it was established that, to improve the image quality would require a protocol that extends the measurement data frame by increasing the number of stimulation electrodes, optimizing the distance between current injection electrodes, and optimizing the surface area of the electrodes. To solve this problem requires independent electrodes that are either used for current injection or for measuring boundary potentials. Hence, compound electrodes are used. Sixteen current injection electrodes covering 66.7 % of the periphery of the test tank were used to provide a more uniform current distribution, as compared to narrow electrodes, in the domain of interest and has low electrode-skin contact impedance.

To meet the constraint on an increase of the measurement frame and number of electrodes, requires the addition of two extra planes of electrodes; one above and the other below the 16-electrode voltage measurement plane. Current is injected through an electrode in the top plane and returned though an electrode in the bottom plane, resulting in a cross-plane current injection pattern. In addition, this injection protocol allows one to incorporate two different current injection protocols (any two from adjacent, opposite, 90 degree, trigonometric or any other protocol) to detect an anomaly.

In this chapter, the theory and corroborating simulations were formed to justify the study of a dual current stimulation (DCS) EIT system. A systematic approach was followed, starting with the simulations of three common current injection patterns for a compound electrode system. It was shown that, of the three patterns, the adjacent injection pattern had the highest current density at the boundary, the perpendicular injection pattern had the most uniform current density and that the diametrically opposite injection pattern produced ghosting when an anomaly was located at a point that is not at the origin. From this, the perpendicular injection pattern was chosen as the first injection method. The next phase involved selecting the second method of excitation. However, as the stimulating electrodes of the single plane system was thought to be hardwired to source and sink current at 90 degrees, a different technique was needed to introduce the second injection pattern. This second injection pattern had to produce a high current density near the boundary of the tank as this is the region where the perpendicular method behaves poorly. To achieve this, the 2D problem was viewed using a 3D coordinate system. It was observed that, if the source and

sink electrodes are in the xy-plane and if these electrodes were diametrically opposite, then an anomaly can be placed along the z-axis without the occurrence of ghosting. It was then stated that reducing the distance between these electrodes will result in a higher current density for small values of z, this is true because current scatters throughout the 3D domain. Furthermore, in the xy-plane, an opposite current pattern is observed and in the yz-plane, an adjacent current pattern is observed. This intuitively suggests that if the z-axis goes along the diameter of the test tank, starting at zero, then the current will distribute throughout the tank in a similar way as if an adjacent pattern was injected in the z-axis; around the boundary of the tank. At this point two electrode planes were needed; one above and the other below the measuring plane. This resulted in a DCS EIT system when the center plane is used to source and sink current perpendicularly while simultaneously measuring the boundary potentials, and the top and bottom planes are used to inject current from top to bottom while, again, the boundary potentials are simultaneously measured at the center plane electrodes. Following the theory of a DCS system, a few simulations were generated to view whether or not the DCS system is capable of enhancing the detectability and distinguishability of the EIT system as compared to a single current stimulus system, using visual inspection. In addition, the DCS EIT system showed a spatial resolution improvement by 50 %, compared to a single plane stimulation EIT system. Moreover, the simulations agreed with the theory, and design of the EIT hardware system can commence.

4 EIT system design

In this chapter, a motivation for the development of an EIT system to aid in answering the research question will be presented. Thereafter, several system specifications and requirements will be discussed. Furthermore, the procedure followed to design an EIT system for this research, which includes creating a phantom test tank within which anomalies will be placed, will be discussed. Additionally, the final step is to construct a data acquisition system which measures the resulting boundary potentials, and transmits this data to a controller module that will process the data before sending the result to a computer, or to resume onboard computations.

4.1 Motivation for an EIT system

At the beginning of this research, and to the best of the author's knowledge, an EIT system that could perform time difference imaging while using dual current stimulation patterns was unavailable. Hence, a new system is needed to answer the research question. Furthermore, based on the following system requirements, a new system is needed.

1. *Current injection and voltage measurement independency:*

   To significantly reduce the effects of contact impedance at the electrodes, while creating independent current stimulation and voltage measurement electrodes, a compound electrode system is needed. These electrodes provide more available non-redundant measurements which improves the system accuracy, compared to systems that share electrodes for current stimulation and voltage measurement. Furthermore, these systems have low interference between all electrodes as the driving and measurement electrodes are independent [41].

2. *Time Difference Imaging:*

   As the research question places a constraint on the type of imaging, thus, a time difference imaging system will be designed. Although the system will be used to produce time difference images, it will remain flexible enough to allow adaptation of frequency difference imaging, by applying a frequency sweep signal.

3. *24-bit versus 16-bit data acquisition:*

   To determine how much the image quality is improved, by increasing the measurement bit resolution, a 24-bit data acquisition system will be compared to a 16-bit system.

4.2 EIT system specifications

The aim of designing an EIT system for this research, is to design an electrical anomaly detection system by mapping the internal impedance distribution of the system. Furthermore, most geological and process monitoring applications require tomographic system that are large and expensive compared to biomedical application requirements [48]. The reason behind this is that biological specimen, such as the breasts, lungs, brain and thorax all require low amplitude and frequency stimulating signals; signals operating under 1 mA at a maximum frequency of 1 MHz [36]. Hence, the most cost-effective application for student research is one which focuses on imaging biological specimen or a downscaled prototype EIT system that can incorporate industry needs. The following sections provide well documented engineering standards to ensure system reliability and safety.

4.2.1 Functional characteristics

Functional characteristic overview

The EIT system is designed to reconstruct cross-sectional images using the computed internal impedance distribution of objects. This is done by surrounding the object with a ring of driving and measurement electrodes and using additional circuitry to extract and analyze the measured

quantities. A few constraints regarding the hardware of the final system, is that the system needs to be portable, cost-effective, light-weight and produced from an assembly of easily accessible products. The data are collected using an analogue-to-digital converter (ADC), which sends the measured and formatted quantities to a controller module or PC. Images are reconstructed from these measurements using the MATLAB EIDORS image reconstruction libraries.

Signal Levels

In biomedical applications, the stimulation current that can be sensed by biological tissue and penetrate through the resistance of skin is 1 mA at 1 kHz [49]. Applications that require lower amplitudes must adhere to higher frequency signals. While lower frequency requirements need larger proportional amplitudes. This amplitude-frequency trade-off is based on the hearts vulnerability at frequencies higher than 60 Hz [6]. In industrial applications, the penetrating signal must have a higher amplitude and/or frequency.

Frame Rates

For the purpose of this research, a decision was made that the maximum time taken to read all measurements (4096) is one minute, as this gives ample time for the designed system to acquire a complete set of data. This can be improved if a fully parallel ERT system design is used; any frame rate above this is adequate. Furthermore, as the frame rate bears no significance to the research questions, as long as data is acquired in a reasonable amount of time of less than one minute, it is concluded that the system has an adequate frame rate.

System Accuracy

A system measurement accuracy of 0.9 % would be deemed satisfactory for a 16 electrode single plane system, which uses a 10-bit resolution ADC and can detect a voltage in a range of 5 [V], [6]. A 48 electrode DCS EIT system is expected to have the same measurement accuracy because the boundary potentials are only measured using the 16 electrodes in the center plane. Furthermore, the measurement accuracy per electrode is $\frac{total\ measurement\ accuracy}{total\ electrodes} = \frac{0.9\%}{16} = 0.05625\ \%$. A 24-bit data acquisition system is adequate to achieve this level of accuracy.

4.2.2 Safety characteristics

A few safety precautions are listed below. Although the designed system will not explicitly focus on biomedical imaging, it does use some of the constraints placed upon biomedical instrumentation.

- Overcurrent fuses will be used to prevent possible fires and electrical shorts caused by an electrical fault.
- Common ground will be used throughout the system.
- Multiple points of failure will be integrated into the system.
- System diagnostic tests will be performed regularly using risk preventative methods that are embedded into the computer algorithm.
- Implement fail-safe computer algorithms and hardware.

4.2.3 Non-functional characteristics

A few non-functional characteristics of the system are described below. These characteristics do not directly describe the operational requirements of the system nor do they place any test subject safety constraints. These characteristics define the user-end side of the design for the final system after the prototyping stage.

System quality

The system is to be assembled from easily accessible, high quality and reliable components to ensure repeatable performance over long term usage.

System data acquisition fabrication

The data acquisition system should be fabricated using university resources. This includes free sourced PCB design software and board printing and component assembly resources.

Economic factors

The project budget is dictated by the university resources. Furthermore, the total cost of the project should be kept to a minimum compared to standard available EIT systems which cost roughly R500 000 [6]. For the prototype, the budget will be capped at R10 000.

Ergonomic factors

To provide an ergonomic system, the following requirements should be met.

- The system should be portable, lightweight and be user-friendly.
- The system should be able to withstand reasonable user–device abuse.
- The system should not create user discomfort.
- The system design layout should be of a logical manner.
- The system should be powered by a 12V DC power supply, as these are common voltage source outlets in vehicles and buildings.

4.3 EIT system layout concepts

A few common EIT hardware concepts need to be reviewed to find the best cost-effective means of acquiring data. This involves connecting the phantom tank to a central processor via a data acquisition system. The central processor is needed to reconstruct the images and to control the acquisition board and the multiplexers. Several EIT system layout concepts are discussed below.

4.3.1 First concept: computer and data acquisition cards

Using a personal computer to receive data from a data acquisition card, such as the μDAQ cards by Eagle Electronics, provide the simplest system layout. These cards come as an ADC or DAC or a combination of the two. If two cards are used, then referring to Figure 4- 1, the image reconstruction and display tasks are done on a personal computer. A DAC card sources an analog electrical signal. This signal is passed to a voltage controlled current source (VCCS), and the resulting signal is multiplexed to the surface mounted electrodes on a test tank. At the voltage

measurement end, the voltages at the boundary of the tank are measured using difference amplifiers. The result is passed to an ADC card that measures and samples the output analog signal before sending the result to the computer for image reconstruction.

These cards provide high sampling rates (as high as 1 MHz) shared among 16 channels. Consequently, the sampling rate is 62.5 kHz per channel. Furthermore, the slower of the two cards dictate the sampling speed of the system; the sampling speed should be twice that of the card that has the slowest signal output or measure rate.

4.3.2 Second concept: computer and microcontroller

Most applications that require signal transmission and data acquisition, require devices that can store samples of the measured data, in memory, before sending that acquired data to a primary device that does further formatting of this data before producing useful information. Microcontrollers have severely limited storing capabilities. One of several other solutions to this problem, if microcontroller compatibility is essential, is to store all code on the primary device, such as a computer, and use the microcontroller as a secondary control device. The supply signal could be processed on the computer, and sent through the microcontroller's onboard DAC, to produce a supply signal. However, most onboard DACs have limiting output frequencies and bit resolutions. With regard to the storing problem, a SD card may be used to increase the memory of the controller. This design layout is shown in Figure 4- 1.

4.3.3 Third concept: computer and field programmable gate array (FPGA) board

The concept of using a FPGA, coupled with a computer, is similar to the previous concept. The advantages of using an FPGA, over a microcontroller, is the processing speed and system flexibility. However, the FPGA shares some inherent disadvantages with the microcontroller such as the low onboard memory (a 5GB storage space is needed for EIT applications) while being less cost-effective. A stand-alone FPGA system was considered, using the Altera SocKit Cyclone V development board. It provided 1 GB RAM with 128 MB QSPI Flash and 925 MHz processing

speed. However, the setup costs for the FPGA system was much higher than the alternatives, and did not provide enough advantages over the other concepts to justify the implementation costs.

4.3.4 Fourth concept: microcomputer

Microcomputers provide some promise, as they remove the cost and need for a personal computer. Two microcomputers were considered for the task; the PCDuino 3B and the BeagleBone Black. Of the two choices, the PCDuino provided the most onboard storage of 1GB with 1GHz onboard processing capabilities. Furthermore, it has storage upgrade capabilities via a SD card slot. However, the PCDuino required additional software to provide a supply signal and read and format the measured data. In contrast, the microcomputer tends to outweigh the disadvantages of a computer or FPGA standalone systems. In addition, this concept can be powered from a 5V DC source. Which means that this system provides advantages in cost, size, portability, speed, and flexibility. However, for the research questions that need to be answered, the microcomputer provides a high level of complexity during the implementation phase as compared to the other concepts, which will dramatically affect implementation times. This is due to the fact that new image reconstruction libraries are needed to be written specifically for the microcomputer.

4.3.5 Concept evaluation

The above mentioned concepts are now evaluated towards achieving the functional, safety and non-functional characteristics that were previously outlined. A scaling system is used to assign scores to each concept based on *portability, cost, design complexity, implementation complexity, supply and control signal output rate, and the data acquisition rate.* All system concepts need to be portable, which is weighted at 5 %. The overall cost is an important factor, and is weighted at 15 %. Design complexity establishes how complicated the design is, which adds to the time needed for implementation, and is given a weight of 20 %, which implies that a design that has a high level of complexity will drastically affect the design and implementation time. The implementation complexity refers to the accessibility of the system components and how long it

will take from ordering components to setting up the complete system, and is given a weight of 10 %, because the time needed to implement the system will greatly affect the time it takes to complete the research objectives. The signal output rate is given a weight of 20 %, because the output rate affects the frame rate of the system. The data acquisition rate is given the remaining weight of 30 %, because it affects the frame rates while restricting the range of frequencies that can be used to reconstruct an image. The table below shows the scoring for each concept.

Table 4- 1: EIT System Layout Concept Scoring Table

	Characteristics						
Concept	Portability [5%]	Cost [15%]	Design Complexity [20%]	Implementation complexity [10%]	Signal Output Rate [20%]	Data Acquisition Rate [30%]	Total [100%]
1	50	50	70	90	10	50	50
2	50	80	80	70	50	50	62.5
3	100	30	30	40	90	90	58.5
4	100	50	50	50	80	80	67.5

As seen in Table 4- 1 above, concept four provides the best overall score, however, the complexity of the system layout will cause too many delays. Concept three provided the best functional characteristics, however, the cost of implementing this concept far outweigh its advantages, which are not as much of an advancement over the other concepts. Concept two is the best suited system layout for the research as it provides low complexity and cost, which are two major factors for the time to completion and the cost of the investigation. Furthermore, the μDAQ was selected for the 16-bit system as it was readily available.

A block diagram of a complete signal injection and voltage measurement procedure is given below.

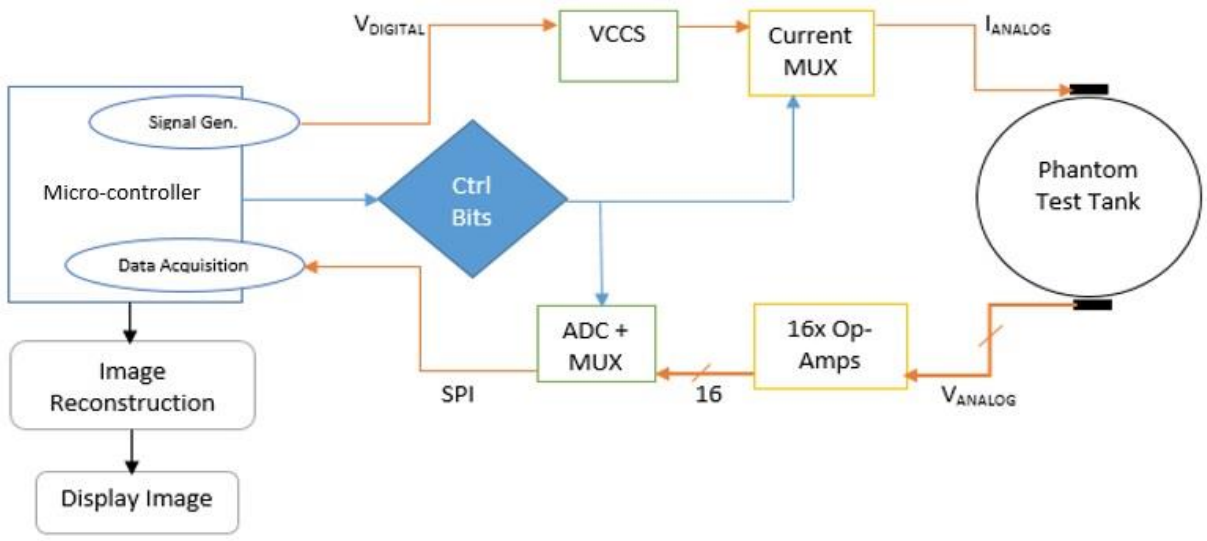

Figure 4- 1: Block Diagram of the complete EIT system (NB. Crossed arrows indicate serial bus connections)

Figure 4- 1 shows the complete EIT system flowchart. It shows that voltage is generated using a signal generator. This voltage is then used to control a VCCS which sends a constant amplitude current to the correct drive electrode pair, using a 16 channel multiplexer. While the current is injected into the test tank, the boundary voltages will be measured simultaneously and passed to 16 analog signal amplifiers. These amplifiers compute the voltage difference between two adjacent measuring electrodes and amplify the result. The resulting signals are sent to an ADC which should have an onboard multiplexer to multiplex through each of the signals, to reduce the cost of using 16 ADC's. The digital signal from the ADC is then transmitted to the microcontroller which computes the voltage equivalent value from the ADC samples and sends the result to a computer. The computer then opens these results in MATLAB and the EIDORS toolkit is used to reconstruct an image from this data.

4.4 Design of a phantom test tank

Typically, for 2D EIT systems, a single electrode plane test tank is used. However, these systems can only apply a single, usually hardwired, current stimulation pattern. As discussed in Chapter 3, a common current pattern is the adjacent current drive, which has a high current density near the boundary and significantly weaker current density at the center of the tank. Another common pattern is the opposite current drive which places the current electrode pairs diametrically opposite each other. This pattern introduces ghosting; a mirror image of an anomaly near the boundary is produced during the image reconstruction phase. An alternative current drive pattern is the 90-degree current drive pattern, which is achieved by placing the current source-sink electrode pair ninety degrees apart. This pattern achieves a current density that is strongest near the center of the tank, and weaker near the boundary furthest from the current source-sink electrode pair. Thus, a system that incorporates two patterns (a dual current stimulation system), one with a high current density near the boundary and another with a high current density near the center of the tank, would be a reliable system that could detect anomalies at any position within the tank. This could be achieved by *soft-connecting* the current drive electrodes; using multiplexers and code to switch between current driving patterns. However, this method will increase the system complexity and cost by requiring additional multiplexers. Alternatively, the current drive patterns could be independently *hardwired*, by introducing two extra planes of electrodes as shown in Figure 4- 2 below. In addition, this dual current stimulation protocol provides more available non-redundant measurements, which will improve the spatial resolution (as computed in Chapter 3) and detection capabilities (which will be shown in a subsequent chapter).

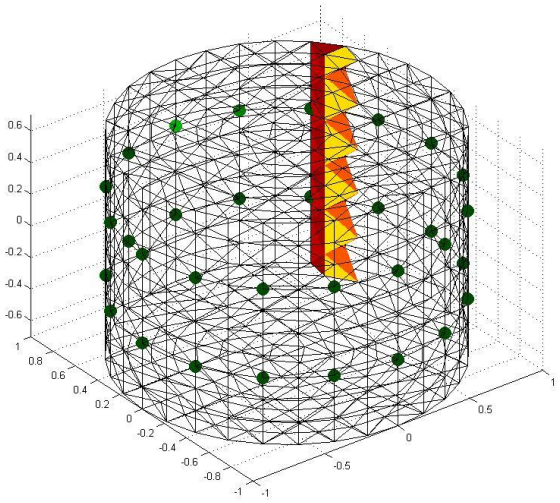

Figure 4- 2: Two plane EIT system used to introduce an additional current pattern – excludes the center plane

Figure 4- 3: Slices from Figure 4- 2 after applying a cross-plane adjacent current stimulation pattern

Figure 4- 2 shows the two extra planes of electrodes that are used to introduce an additional current drive pattern. The tank contains an anomaly near the boundary of the tank, which is to be detected. The simplest pattern to introduce between two planes is the adjacent current drive pattern. In this case, current enters through a source electrode in the top plane, and exits through an electrode directly below the source electrode, in the bottom plane; hence, detecting an anomaly close to the boundary between these planes as shown in Figure 4- 3. The center plane should have a different current drive pattern which has a high current density near the center of the tank as discussed in Chapter 3; a 90-degree current drive pattern.

A few things to consider before selecting the number and type of electrodes are:

1. The electrodes should have a slow corrosion rate with high conductance.
2. The electrodes should cover 60-70 % of the tanks circumference to ensure optimal electric field intensity and to reduce contact impedance [1]; wide electrodes increase sensitivity by providing a more uniform current distribution compared to narrow electrodes. On the other hand, if the electrodes are too wide, a short circuit could occur for injected currents and coerces the contact surface underneath the electrodes to assume an equal potential (due to a high conductive electrode) which reduces internal current density and affects the distribution of the sensing field, causing a degradation of the reconstructed image.
3. Increasing the number of electrodes causes an increase in the measurement times and usable data, resulting in an improved image quality.
4. Using compound electrodes reduces contact impedance while providing independent current source and voltage measuring electrodes. These electrodes further reduce the trade-off between having the best current pattern and the best voltage pattern [1], [12].

Based on the considerations above, the following decisions have been made to ensure that an optimal test tank system is designed:

1. Test tank with a diameter of 15 cm.
2. 16 stainless-steel compound electrodes per plane (48 total electrodes) of outer diameter 20 mm, middle diameter of 10 mm and inner diameter of 6 mm.
3. Planes are spaced 2.5 cm apart.

Below is an image of the phantom test tank.

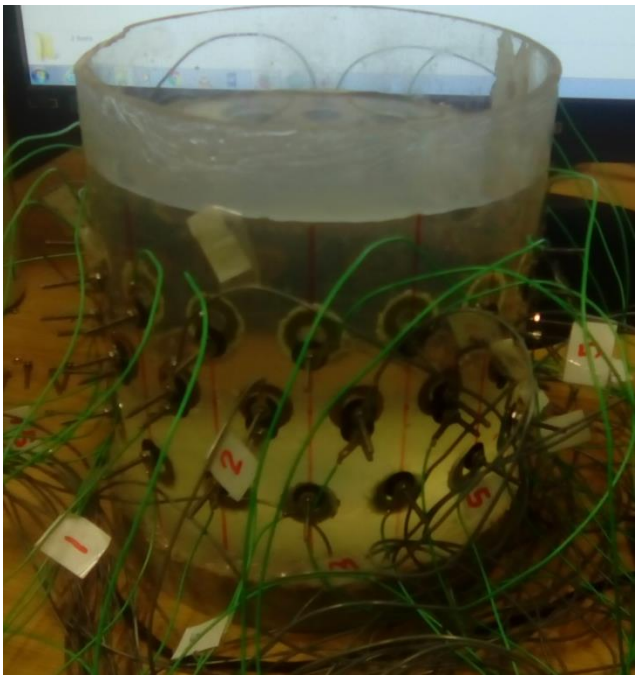

Figure 4- 4: Phantom 48-electrode test tank for use in the Dual EIT system.

In Figure 4- 4 above, there are 48 compound electrodes (three planes of 16 electrodes each). The center plane is used to inject alternating current at 90 degrees while simultaneously measuring the resulting boundary potentials. The top and bottom planes introduce a second cross plane adjacent current drive pattern. Furthermore, the boundary voltages will only be measured around the center plane, to keep this a 2D EIT problem.

After completion of the test tank, the next step is to measure the resistance across the measurement electrodes to later determine the voltage drop across the electrodes. To measure the resistance across the electrodes, a multi-meter probe must be attached to the electrode within the tank and the other probe should be attached to the outer screw end of the electrode. The measured resistance varied from electrode to electrode. Consequently, the range of electrode resistance was 7.5 Ω to 9 Ω. These values are significantly lower than the expected resistance of the contents of the test tank, thus, it will not significantly affect boundary voltages measurements.

4.5 Supply signal transmission and data acquisition

A stable alternating current should be multiplexed to the individual current electrode pairs. To achieve this, a voltage-controlled current-source with a signal generator, the Agilent 33220A, is used to supply the current at an amplitude of 1 mA with a frequency in the range of [1 kHz, 1 MHz].

An alternating current is applied to a pair of (16 channel) multiplexers; in the electrode plane. Considering current stimulation in the center electrode plane, one multiplexer switches the supply current to consecutive electrodes while the second multiplexer introduces a return path, 90 degrees apart from the supply current electrode, through which the current will flow. While the current flows from one electrode to another, the potential buildup at the electrodes in the center plane is measured. The resulting boundary potentials are passed through a high input impedance signal amplifier, which outputs the voltage difference between two adjacent electrodes. The resulting 16 voltage difference signals enter an analog-to-digital (ADC) module, which samples and holds the voltage values before converting the result to a digital signal. This digital signal is then sent to a microcontroller for further computations and the result is sent to a PC for image reconstruction. This process is repeated for the cross plane current stimulation protocol. The following sections outline the main characteristics of each component in the data acquisition system.

4.5.1 Design of a current source

A sinusoidal voltage signal is supplied by the Agilent 33220A signal generator. A current source, the modified Howland voltage-controlled current source made using an AD795 op-amp, which is shown in Figure A- 1, in Appendix A, is then needed to convert this supply voltage to a sinusoidal current, which will stimulate the test tank.

The voltage controlled current source (VCCS), shown in Figure A- 1, was designed to produce a constant current, across a grounded load, in the micro- to milli-ampere range. The resistor R5 is used to set the gain and is selected to match the ratio R1/R4 to R3/(R4+R5). Typically, this ratio is set to 1/1 and the resistors R1 = R3 = R4 = R, R5 = r, R2 = R+r and R6 is given the expected total resistance of the test tank.

In contrast, current will be injected between a selected pair of injection electrodes. Hence, current should flow into one electrode and exit through the paired electrode. Most EIT systems keep an electrode fixed to ground and inject current through the remaining electrodes [6], this results in an asymmetrical system because a single electrode is used to sink current from several other current source electrodes, resulting in a highly concentrated current density near this electrode. In contrast, the EIT system for this research was designed to treat the tank as an ungrounded system, which means that there is no ground points on the tank. Instead, the tank is treated as a '*resistor*' connected in series with the EIT system, which means that a positive current will be injected into the tank through a current source electrode and a negative current, of equal magnitude, will exit at the current sink electrode. As most current sources are single ended, a dual ended source is needed. This is done by designing a Mirrored Modified Howland Current Source (MMHCS) shown in Figure A- 2, in Appendix A.

In Figure A- 2, two wide bandwidth op-amp circuits are used. The MMHCS provides a constant current across a load. This setup consists of two symmetrical, modified Howland circuits. The circuit was designed to produce a constant load current of 1 mA from 1 Hz to 1 MHz. It is expected to have an output impedance of 70 Ω. Furthermore, research has shown that the output impedance of the VCCS should be larger than the expected impedance of the test load [1]. In contrast, the circuit above was tested using the expected loads and was fully capable of supplying the constant current, even though the output impedance is lower than that of the contents of the test tank.

In addition, the resistors were selected based on the constraints placed upon the modified Howland source, the selected input voltage and the required load current. The circuit in Figure A-2 was simulated in LTSpice for a load resistor value in the range 1 Ω to 10 kΩ. The load current was observed to be a constant 1 mA over this range of load resistances and over the frequency range 1 kHz to 25 kHz, which is adequate for the task at hand. The plot in Figure A- 3, in Appendix A, shows that the load current remained at 1 mA for a variable load resistance of 1-10 kΩ and a supply voltage of 1 V. This confirms that the designed and simulated current source is adequate for the EIT system.

4.5.2 Supply current multiplexing

The supply alternating current is multiplexed between different pairs of current injection electrodes. Each pair of electrodes should have a closed path, through which the supply current must flow. Thus, two multiplexers are needed per current injection protocol; one to supply the positive current and another to provide a negative current or current return path. There are a tally of four multiplexers; two per current injection method. One pair forces a 90 degree current injection protocol in the center plane, while the remaining pair forces the cross plane current injection protocol between the top and bottom planes. The requirements for the current multiplexer, is that it should have 16 channels to be able to multiplex through all 16 electrode pairs per injection pattern, fast signal propagation speeds to reduce data acquisition delays, noise cancellation properties to reduce interferences (which cause artifacts in the reconstructed images) and a low uniform internal resistance to avoid asymmetric and large voltage drops and saturation of the VCCS. Hence, the following multiplexer was selected.

The CD74HCT4067 multiplexer/de-multiplexer, by Texas Instruments, is used to multiplex the supply signals. The CD74HCT4067 has the following characteristics.

- Wide analog input voltage range; up to 7 V.
- Low resistance.
- Fast signal propagation speeds of up to 1 ns.
- 16 Channel multiplexing/de-multiplexing.
- Low power consumption.
- High noise immunity (cancel noise levels as high as 30% of the supply voltage).

Consequently, simulations of the multiplexer is not needed as it provides these characteristics which surpass that which is required by the EIT system, and any uncertainties in the circuit will not cause any major alterations in the amplitude or frequency of the injected current; as guaranteed by the trusted manufacturer. Furthermore, the circuit will be tested using an Arduino and a resistor-LED network in the next chapter to ensure that it is capable and reliable in performing the required tasks.

As the current supply and return paths are being multiplexed to the appropriate current electrode pair, voltages are formed inside and on the surface of the test tank. The voltages on the surface of the tank is to be measured. Thus, a high input impedance signal amplifier is placed at the voltage measuring electrodes around the center plane to measure these voltage differences while attenuating the output current at these electrodes.

4.5.3 Output signal amplifier: boundary voltage measurements

The voltage between each adjacent pair of electrodes should be measured and amplified. The difference between adjacent electrode voltages are measured instead of single electrode voltages to avoid large voltage ranges, common-mode rejection ratios and gain bandwidth [6]. A few signal amplifier circuits were considered such as the differential, operation and instrument amplifiers. The operational amplifier is a building block of all amplifiers, it has a moderately high input impedance which reduces the input current to nearly zero (which is a system requirement). However, additional external resistors are needed to select the gain. The difference amplifier allows some current to enter through the input terminals and a varying resistive input source from measurement loads could cause measurement variations which affects the system accuracy and repeatability. The instrument amplifier is a difference amplifier with the advantages of using one external resistor to set the gain and no current flows in or out of the device, irrespective of a variation in the input resistors. In summary, the instrument amplifier described below was selected, as it provides adequate bandwidth, reduced implementation complexity, signal transmission speed and a high input impedance to reduce current flowing out of the tank and into the amplifier circuitry.

The LM7041N was selected as the output operational amplifier which will be used to construct an instrument amplifier. This amplifier provides:

- A typical bandwidth of 1 MHz
- Wide voltage supply range of 3-32 V.
- Draws 700 µA (max) when supplied with 32 V.
- Low complexity for implementation.
- Fast signal transmission.
- Low input bias current of 45 nA.
- Low input offset voltage of 2 mV and offset current of 5 nA.

Typically, these circuits are configured in the following way:

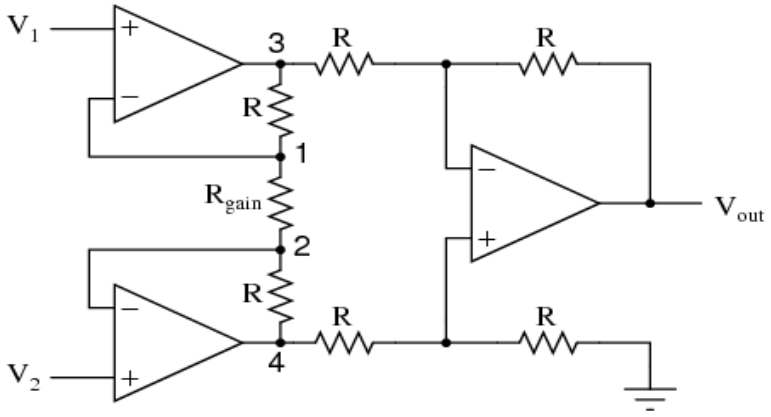

Figure 4- 5: Typical Application of a LM7041N. The gain of this instrument amplifier can be controlled with Rgain.

Figure 4- 5, above, shows the typical application of a LM7041N incorporated instrument amplifier circuit. The circuit receives two boundary voltages. The difference between these voltages are measured before the result is amplified. The output is defined by the following equation.

$$V_{out} = \left(1 + \frac{2R}{R_{gain}}\right)(V_2 - V_1) = 3(V_2 - V_1)\ [V] \tag{4.1}$$

In the above equation, the ratio of the external resistors, selected to be significantly greater than the internal resistance of the phantom test tank (to minimize the resistive loading of the source) and well-matched to obtain an acceptable Common Mode Rejection Ratio, provide an adequate gain of three if all resistors are equal. Twelve quad Op-Amps were selected to form 16 instrument amplifiers to measure the 16 possible output voltage differences which are sent to an ADC for data conversion.

To simulate the above circuit, an AD795 op-amp was used as it provides identical operational characteristics to a single op-amp within the LM7041N integrated circuit and was readily available on the software simulation package, shown in Figure A- 4 in Appendix A.

Figure A- 4 was simulated in software. The input voltages were set to 500mV and 100mV. The current at the input was observed to be zero and the output voltage was 1.2V, shown in Figure A-5. Hence, the simulation concluded that there was a zero input current and the voltage at the output was equal to three times the input voltage difference, as expected. This gain was selected to ensure that the resistors are well above the resistance of the contents of the test tank and to ensure symmetry at the output of the tank. Furthermore, capacitors were placed at the inputs of the circuits, to allow AC-coupling.

In addition, multiple variations in the input voltage was used to test the design. The maximum output voltage was observed to be Vsupply-0.1 [V] (Vsupply = 7 V). Sinusoidal signals were applied to the inputs and the frequency was swept to observe the maximum input frequency. The maximum frequency was observed to be 0.93 MHz, after which the circuit reached a saturation and a roll-off occurred at the output.

4.5.4 Signal analog-to-digital (ADC) conversion

After measuring the 16 output boundary potentials, the signals need to be converted to a digital format before the data can be processed on a microcontroller. The system requirements for an ADC circuit is:

- 16 channel input to measure output voltages from all 16 instrument amplifiers.
- Sample and hold capabilities, if the channels are multiplexed (not needed for multichannel output conversion).
- High speed data conversion of at least 2 kHz to convert fast enough throughout the input signal bandwidth. Due to the fact that the measured signal should be sampled at a rate of at least twice that of the minimum expected signal frequency, which is 1 kHz.

16-bit data acquisition

The 16-channel 16-bit µDAQ board by Eagle technology (µDAQ USB30-D) was used to do the necessary A/D conversion of the measured boundary potentials. This board has the following abilities:

- 16 channel ADC inputs.
- 4 channel DAC outputs.
- 1MHz sampling rate.
- 16-bit resolution.

24-bit data acquisition

A 16-channel 24-bit ADC, by Linear Technology (LTC2418), was selected to improve the systems bit resolution. The LTC2418 has the following characteristics.

- 16 Channel inputs.
- 24-Bit resolution.
- Low supply current (200 µA).
- No missing codes (2ppm INL).
- 0.2ppm Noise.
- No Latency which leads to accurate conversion.
- Internal Sample-and-hold Circuit and Multiplexer.
- High DC common mode input rejection (>140 dB).
- Uses 4-wire SPI communication interface.
- Minimum Conversion Time (set by a maximum external oscillator frequency of 2 MHz) = 10.255 [ms].

The following diagram depicts the state transition within the LTC2418.

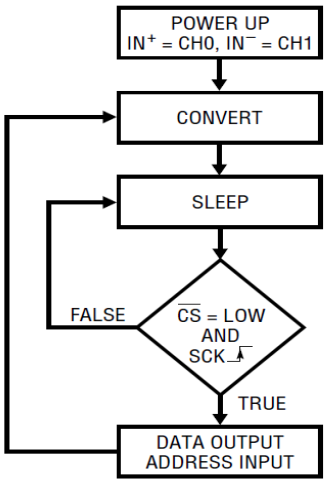

Figure 4- 6: LTC2418 State Transition Diagram

Figure 4- 6, above, shows the state transition of the LTC2418. At start up, the IC goes into a conversion state. Once the conversion is complete, the IC enters sleep mode while it waits for the next conversion instruction. To wake-up the IC, a logic low signal should be applied to the chip select pin during the rising edge of the serial clock signal. When the IC operates in awake mode, the value stored on the internal sample and hold circuit (from the output of the internal multiplexer, which switches between the 16 input differential voltage signals) is converted to a digital format, and the result is returned to the Arduino Due microcontroller via the serial data output pin of the ADC.

Furthermore, the 24-bit IC provides several speed advantages over the 16-bit data acquisition board. For this reason, the speed at which data is acquired (i.e. system frame rate) will not be assessed as the two boards are not identical. For this reason, the comparison between the two systems is strictly limited to the image quality based on the change in bit resolution and the measurement accuracy. The speed of conversion is irrelevant for the comparison of the reconstructed images based on the bit resolution. This does become relevant when comparing the DCS EIT method to the single plane current stimulation method, because one of the two ADC's will be used for both methods.

Consequently, these circuits were not simulated as their operations are to convert data without any variation, such as applying any simple mathematical operations to the measurement result. Furthermore, the ADC circuits will be tested by applying test signals to the input channels and compared to the results from a precision multi-meter.

4.5.5 Data acquisition board design

After selecting the appropriate components, the next step is to design a PCB that allows communication between the different IC's. The following diagram depicts the data acquisition PCB schematic.

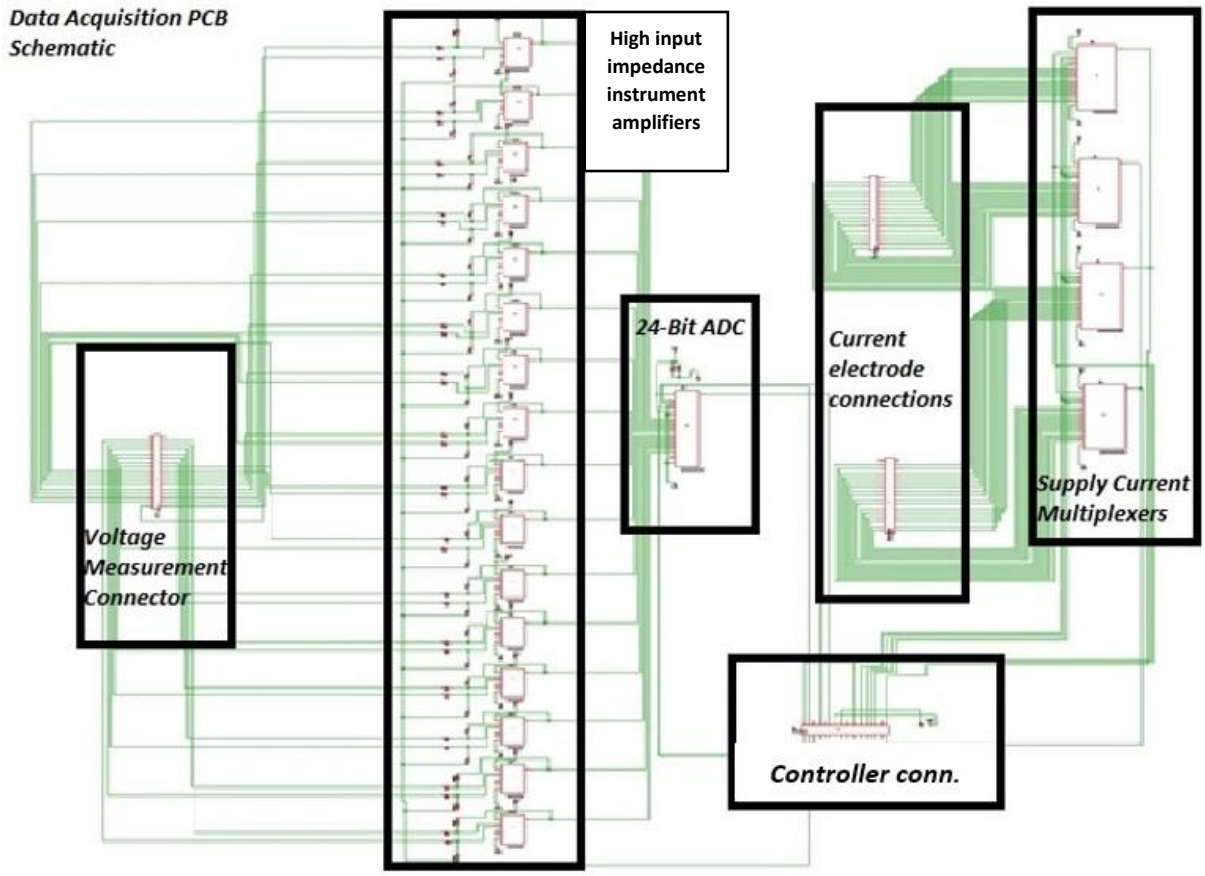

Figure 4- 7: EIT Data Acquisition Board Schematic

Furthermore, the above schematic is converted to a PCB board file which is sent for fabrication. The complete EIT system can then be assembled after fabricating the board.

4.6 Summary

This chapter provided the complete process taken to design the prototype DCS EIT system. The first step was to select a system layout concept design. Several designs were considered, and the design that managed the best measure between low cost and functional performance was selected. This concept employed the microcontroller for system control and data post-processing. The measured data was then stored onboard a personal computer, and additional code were written in the C programming language to provide further data formatting before reconstructing an image.

The second step was to design the EIT data acquisition system. The system was designed to reconstruct 2D images that aid in detecting anomalies inside a phantom test tank, using 48 electrodes divided across three electrode planes. The center plane of electrodes used 90 degree current stimulation while the remaining two planes used cross-plane current stimulation. The electrodes are made of stainless-steel with a compound configuration to reduce contact impedance and to provide high electrode conductance, and the voltage measurement electrodes are located in the center plane. Boundary voltages were measured using output instrument amplifiers, with high input impedances to attenuate output leakage current while reducing the effects of contact impedances. The resulting voltage differences were sent to a 16 channel 24-bit ADC which has an internal multiplexer and sample-and-hold circuit, for 24-bit data conversion, and to a 16-bit μDAQ data acquisition board for 16-bit data conversion. The data acquisition board was fabricated and the next step is to test the EIT system. Furthermore, as this is a prototype, several non-functional characteristics were omitted in the design.

5 EIT system test

Before reconstructing images of the test tank, the EIT system should be tested. Testing an EIT system involves testing each individual module of the system, to ensure that they function as intended, and testing the assembled system to ensure repeatability and accuracy.

This chapter first discusses the tests applied to each subsystem. Followed by measuring the zero-input noise levels and DC-offset levels to test the repeatability and accuracy of the assembled system. Furthermore, during the multiplexer and ADC testing stages, a program test was conducted to ensure that the program was able to correctly control these components.

5.1 Voltage controlled current source (VCCS)

A constant supply current is needed to reduce the risk of corrupted data before reconstructing images; corrupted data can be caused when an anomaly is inserted into the tank causing a change in the current distribution, and if an unstable current is injected into the system then the time-difference data might not be useful to detect an anomaly or the reconstructed images will have several random artefacts (causing false positives in the image). The mirrored modified Howland VCCS, in Figure 5- 1, was used to provide a constant current source.

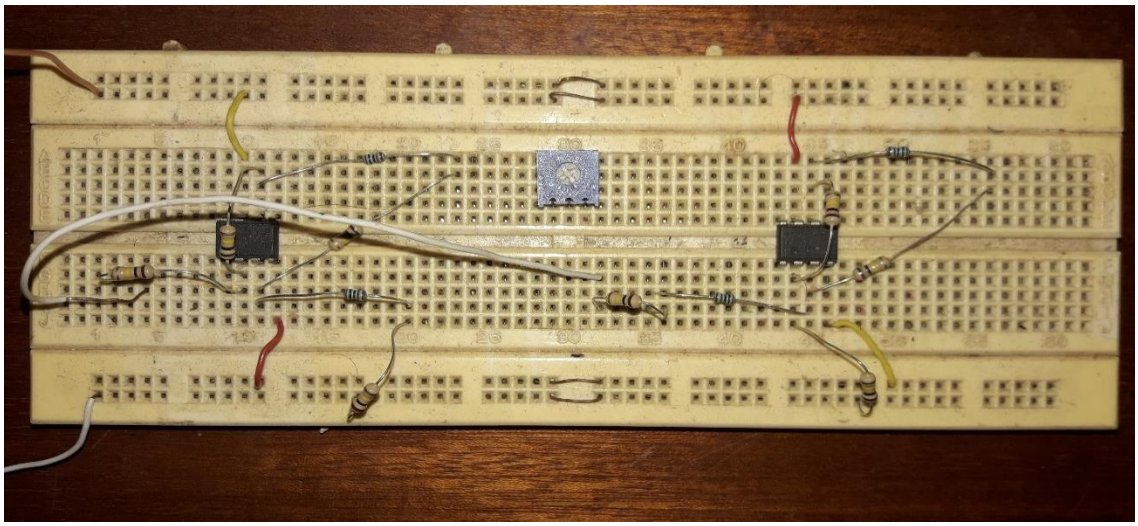

Figure 5- 1: Image of the built mirrored modified Howland current source. The output current is measured across a variable load that matches the expected test tank load.

The circuit in Figure 5- 1 was tested by placing an ammeter in series with an output 100 kΩ variable resistor (blue block component in Figure 5- 1). The resistance of the potentiometer was selected to play the role of the expected changes in resistance of the contents within the test tank. The circuit was designed to supply a 1 mA signal over the frequency range of 1 kHz – 1 MHz, given an input voltage of 1 V within the said frequency range. Furthermore, the test involved turning the potentiometer to vary the load resistance while observing the variation in the supplied current over this range of the load. The test concluded that the current remained constant until the potentiometer resistance caused the output voltage drop to exceed the circuit's voltage saturation limit, which caused the current to have a maximum variation of 22 µA when the load reached 100 kΩ. Additionally, the test tank is expected to never reach 100 kΩ. Instead, the test tank load is expected to have a maximum resistance of 25 kΩ (this value includes the 10 kΩ expected load plus some uncertainty), which is well below the maximum load of the VCCS. This variation in current is acceptable and is not expected to cause major interferences.

5.2 Current multiplexing

After testing the VCCS, the next step is to test that the current multiplexing circuit is working properly. This is done by referring to the datasheet and observing that a binary counter program can be used to cycle through each of the 16 channels of the multiplexer. Each output channel of the circuit was fed to a series LED-Resistor configuration. In total, 16 LED's were placed in a row, and a binary counter program (showing the important section of code in Figure 5- 2) was flashed to the microcontroller to cycle through the channels of the circuit. This setup is shown in **Error! R eference source not found.**. The test concluded that the binary counter program was able to control the multiplexers and that the correct channel delivered the correct amount of current to the LED's to sequentially light each LED. Furthermore, the supply signal frequency and amplitude was limited by the multiplexers. The absolute maximum amplitude limit is 7 V and the frequency limit is 1.2 MHz for the chosen multiplexers. These limits are well above the expected stimulating signal limits, hence, the multiplexer circuits have successfully passed the test.

```
//changes mux switch position
void MUX_SWITCH(byte switched){
  output_low(E);
  int SwitchPos[] = {S3, S2, S1, S0};

  for(int k = 0; k<4 ; k++){
    if(bitRead(switched, k)==1){
      output_high(SwitchPos[k]);

    }
    else{
      output_low(SwitchPos[k]);

    }
  }

}
```

Figure 5- 2: Multiplexer switching code. Used to enable the multiplexer circuit then select a switch position within the circuit to send the input signal to the correct output channel.

The code in Figure 5- 2, enables the multiplexer circuits and forms an array of the switch control pins on the Arduino board. A binary counter is then established, and based on the position in the count sequence, the corresponding pins are switched high or low, hence, the corresponding multiplexer channel is selected. The test was passed and the next step is to test the phantom test tank for any errors.

5.3 Phantom test tank

Inaccuracies in the built test tank should be recorded as these inaccuracies are needed to form a forward model that closely resembles the test tank. Additionally, test tank parameters and internal impedance measurements are needed. The following table shows the parameters of the test tank that were recorded and deemed important.

Table 5- 1: Summary of tests performed to observe the uncertainties of the test tank.

Parameter to be tested	Result	Passed? Y/N	Steps taken to measure parameter and determining the risks
Electrode error displacement	4mm [expected electrode distance is 30mm but some electrodes were spaced 34mm apart]	Y	Physically measuring the distance between electrodes and comparing the result to the ideal distance of 30mm.
Water leakage	No	Y	Filling tank with solution and check for leaks and corrosion after a week.
Test solution impedance	10kΩ	Y	Place multi-meter probes within the tanks solution at the boundaries of the tank.
Wire resistance and expected noise level	Resistance = 0.5Ω Noise level = 0.5*1mA = 0.5mV	Y	A multi-meter is used to measure the resistance of the signal wires. The expected noise level is computed from the measured resistance and the applied current of 1mA.

The table above shows that all tests (deemed important) were passed. Concluding that the built test tank is adequate for further work.

5.4 Voltage measurement amplifiers

The instrument amplifiers, shown in Figure 5- 3, were tested to observe any errors that may exist in the measurement scheme. To test the instrument amplifier circuits, a 100 mV_{pp} and a 500 mV_{pp} were applied to the two inputs of the circuit as was shown in the circuit design and simulation sections in chapter 4, and the output voltage was measured. The circuits were designed to amplify the difference between the two input voltages by a factor of three. The test involved applying the respective voltage at the inputs of the circuit, switch the inputs and finally set one of the inputs to zero. This was done to check that the amplification remained constant for each test and that the measurement system was symmetrical. To conclude, the circuits operated symmetrically at the inputs, which means that the amplification remained constant irrespective of the input signal polarity. Furthermore, the input current was measured to be zero at all inputs.

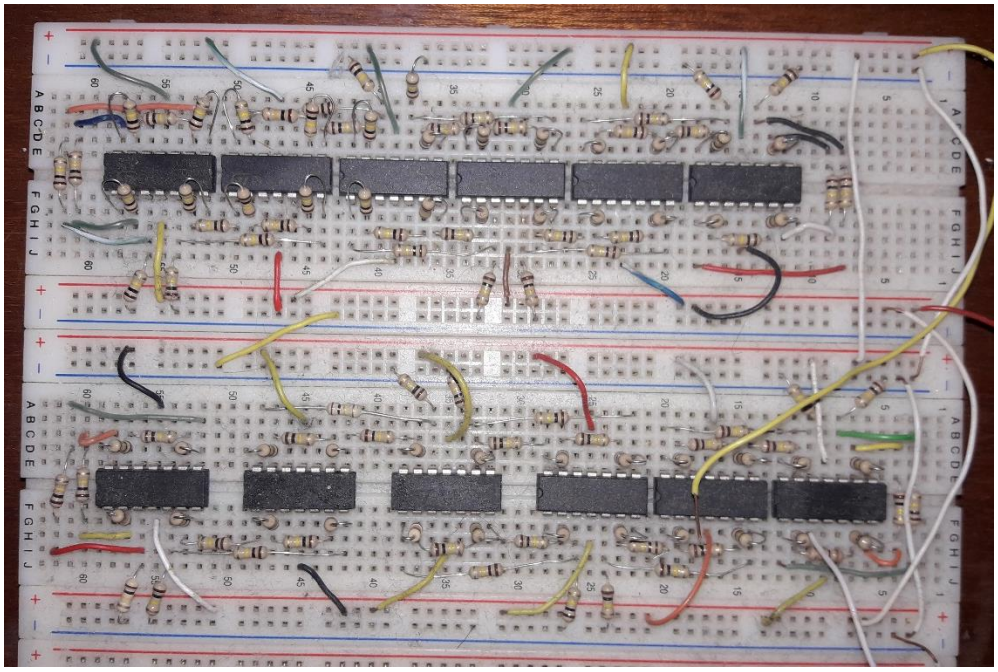

Figure 5- 3: Image of the 16 instrument amplifier circuits made from 12 quad op-amps.

The following conclusions were drawn, following the testing of the instrument amplifier circuits.

- The gain remained at a constant 3 [V/V].
- 2mV noise at the output caused by the noise from the wires exiting the tank.
- Input current remained at 0 A.
- CMRR = 52 dB.
- PSRR = 89.5 dB.

These results are well within accepted bounds, hence, these circuits will be used in the final system.

5.5 Analog-to-digital conversion

To test the ADC boards, requires calibrating the boards based on a comparison between the measured data from the ADC and from a precision multi-meter.

The 16-bit ADC board was tested by supplying a 50 % duty cycle, 250 mV_p square waveform to the input of each channel. The signal was measured by the ADC and it was observed that the ADC had a DC-offset voltage, and the measured signal was amplified by two, as shown in Appendix B, in Figure B- 1. This amplification and offset was compensated for, in the acquisition code.

The 24-bit ADC board was tested by supplying a 200 mV_{pp} sinusoid at each channel, the measured signal is shown in Figure B- 2. However, this board required further calibration, based on the measured signal plot in Figure B- 2. One form of calibration is to select the correct mode of operation, which is to send data on a rising clock edge and capture data on the falling edge. By correcting this mode, the plot in Figure B- 3 was produced.

The plot in Figure B- 3 shows the reconstructed (100 mV_p with a 1 kHz frequency) signal from the samples of the 24-bit ADC. Furthermore, the figure shows that the ADC accurately detects the input signal without any DC-offset or measurement noise. This noise is filtered out by the ADC's onboard notch filter, which only passes signals that have a frequency equal to that which is applied at the frequency control pin, on the ADC chip. All other signals, including noise, is attenuated.

The final test concluded that both boards were operating as expected.

5.6 System accuracy

5.6.1 Zero-input and system measurement accuracy

To ensure that the system produces accurate results, the level of the system's inherent noise needs to be assessed. With the observation of this level of noise, a signal to noise ratio (SNR) can be computed to show the weighting of the measured signal to the noise level, which gives the integrity of the system. In Figure 5- 4, the noise level is observed to be 8 mV_{pp}. Consequently, for a system that is designed to measure a load in the range of 100 Ω to 25 kΩ with an applied current of 1 mA, results in an SNR of 34 dB. This is a reasonable result proving that the noise will not cause extreme negative effects to the measured data [50]. Furthermore, for a minimum expected load resistance of 100 Ω, and an applied current amplitude of 1 mA, a system that has a noise level that lies well below 0.1 [V] is deemed suitable to measure the lowest expected change in impedance caused by the introduction of a 100 Ω anomaly. As such, the noise level is 4 % of the lowest required measured voltage, which is nearly insignificant. Consequently, the system measurement accuracy is 0.045 %, for the designed system which can detect voltages in the range of ±5 [V], using a voltage threshold of 45 [mV].

Figure 5- 4: Image showing the measured zero-input noise level for the EIT system. It shows a noise level with a peak-to-peak voltage of 8mV; by observing the voltage division scale and counting the number of divisions to the peak of the waveform.

5.6.2 DC-bias and low frequency drift analysis

DC-Bias Analysis:

The previous ADC test concluded that there was a zero DC-offset voltage present in the measured results. In contrast, when assembling the EIT system, it is expected that the test tank will introduce a DC offset voltage caused by the introduction of a medium between the supply current and the measured boundary voltages, with a varied impedance along the path through which current flows. However, this DC-offset is created by the internal impedance distribution within the tank and as such is deemed important, and should not be removed from the measured data when reconstructing images.

Low Frequency Drift:

A peak current of 1 mA DC was injected into the test tank over a complete measurement frame to check if the system suffers from low-frequency drift. The recorded plot is shown in Appendix B Figure B- 4.

The plot in Figure B- 4 shows the measured voltage on each channel when a 1mA-peak is injected through the first channel. It shows that the measured voltages remained constant; no low frequency drift in the signal occurred over the complete measurement frame. This process was repeated for all channels.

5.6.3 Voltage profile: U-curve

Several pieces of literature, [36] and [51], have shown a U-shaped plot of the measured boundary voltages, to suggest that the EIT system functions successfully, as it was designed to function. This curve is formed from the basis that, in a simple case, current is applied across two adjacent electrodes. This causes the current to travel through the medium from source to sink electrode. Several current paths will result within the medium which sets up equipotential lines passing perpendicular to these paths, shown in Figure 5- 5. These equipotential lines will then establish voltages at the boundary of the medium.

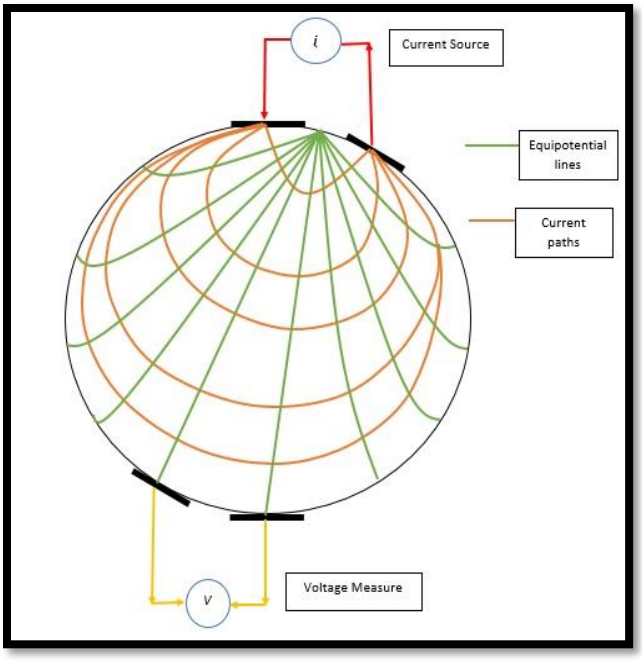

Figure 5- 5: Image of the current patterns and equipotential lines within a medium of miniscule height. The boundary potentials will form a symmetrical U-shaped profile.

Additionally, for a 2D surface of height infinitesimally small, all current flows within the measurement plane and a purely symmetrical boundary voltage U-curve will be established; with the peaks of the U-curve occurring at the current source electrodes. However, as the height and diameter of the test tank increases, so does the current tend to disperse throughout the medium, shown in Figure 5- 6, instead of being confined within the measurement plane. This results in a distorted U-curve. When the height and the diameter of the tank increases, with the same applied current, the less symmetrical the boundary voltage curve becomes.

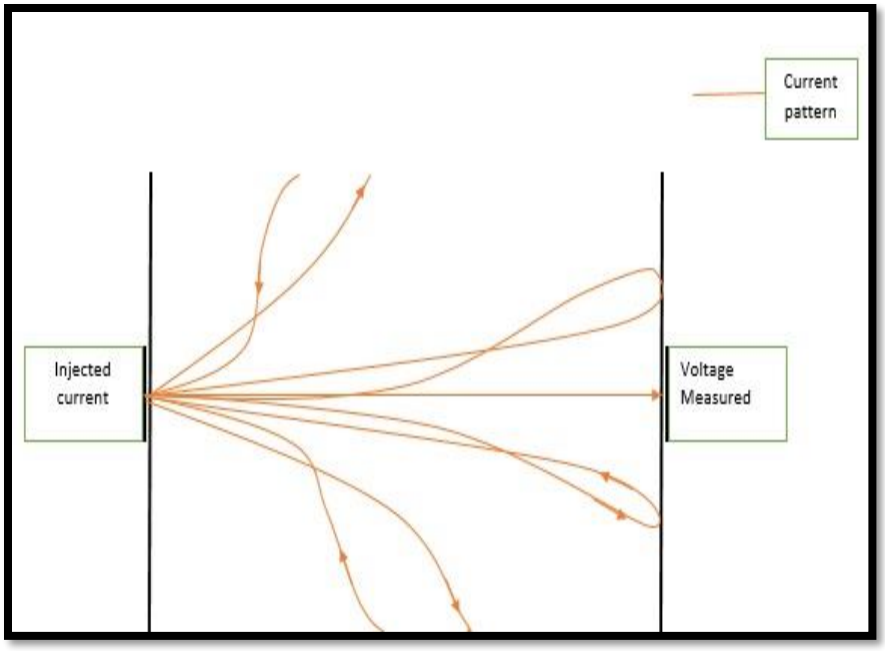

Figure 5- 6: Image showing current dispersions in a test tank [side view of the animated test tank shown]. These dispersions cause a non-symmetrical voltage profile at the boundary of the tank.

It has been shown, [52], that CT scans and X-ray image modalities produce superior images to EIT. This is due to the radiation intensity which is strong enough to directly propagate through the test medium in a straight line. These energy waves begin to scatter throughout the medium as the input signal frequency is reduced. This scattering results in distorted measured voltage profiles which further introduces artifacts within the reconstructed images. Consequently, the more scattering occurs, the more distorted the voltage profile from the measured data becomes, causing more artifacts to appear in the images. As quoted from W. Lionheart *et al* [1], “As the frequency decreases, this non-local effect becomes more pronounced until we reach the case of direct current, in which a change in conductivity would have a small effect on any measurement of surface voltages when any current pattern is applied”.

Furthermore, it must be shown that a reduction in the height and diameter of the test tank will cause fewer current dispersions; which is concluded from the observation of a slightly more symmetrical and less exaggerated voltage profile as compared to the larger tank. This test introduces an additional test tank of height = 2cm and diameter = 7cm, shown in Figure 5- 7.

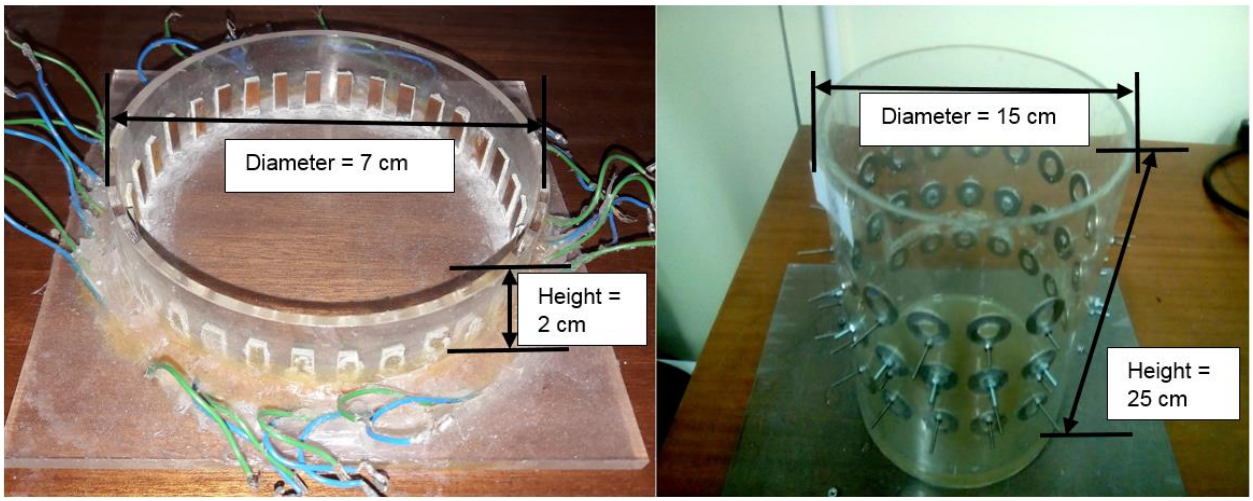

Figure 5- 7: Two test tanks that will be used to show the increase in distortion in the measured data, caused by an increase in current dispersions.

Additionally, to observe the effects of current dispersion, eight independent voltage differences will be measured for each test tank. As opposed to the usual case, where voltage is measured between adjacent electrodes, instead here, the following measuring strategy, shown in Figure 5-8, is used to reduce the number of measurements. Note that reducing the amount of measurements will not affect the overall shape of the voltage profile; only the smoothness of the profile, which is not tested. Furthermore, both tanks were filled with distilled water at room temperature; the test conditions remained the same for both tanks.

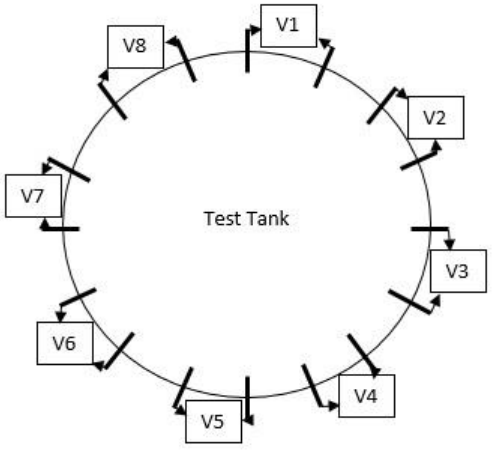

Figure 5- 8: Measurement Protocol to measure the voltage profile per test tank. It shows that eight independent voltage differences are measured.

The voltage per channel from the 7 cm diameter tank is shown in Appendix B Figure B- 5 and a plot of the voltage per channel from the 15 cm diameter tank is shown in Figure B- 6, when an adjacent current stimulation pattern is applied at channel zero.

From Figure B- 5 and Figure B- 6, the peak to peak amplitude was computed and a plot of these amplitudes were used to observe the voltage profile per test tank, shown in Figure 5- 9.

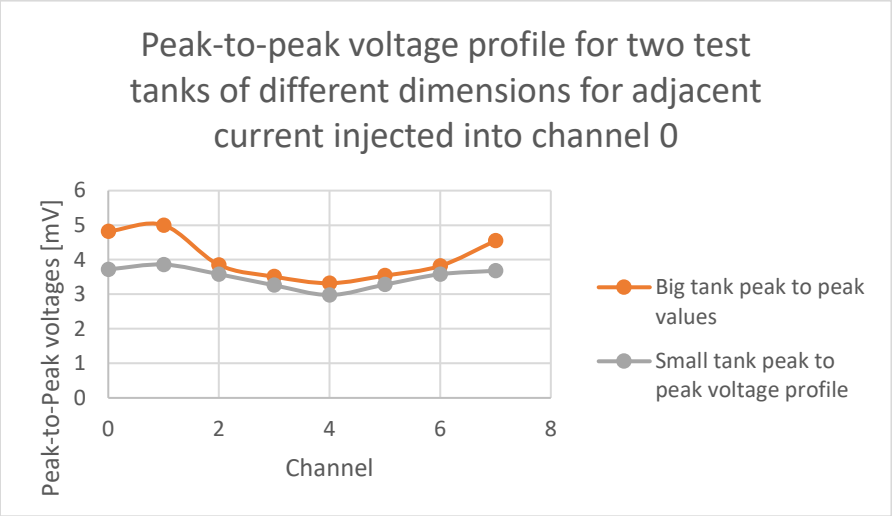

Figure 5- 9: Plot of the voltage profile per test tank. It shows that the larger tank required the VCCS to supply more voltage to keep the current constant as the resistance of the tank was high, causing more current dispersions. Second tanks profile is symmetrical

From Figure 5- 9, it is clear that the voltage profile becomes more exaggerated as the physical parameters of the tank increases, which is caused by the DC offsets (and degree current dispersions) for each tank. The following figure shows the voltage profile for a complete measurement frame, when multiplexing the application of a 1 mA current at 1 kHz to the large test tank.

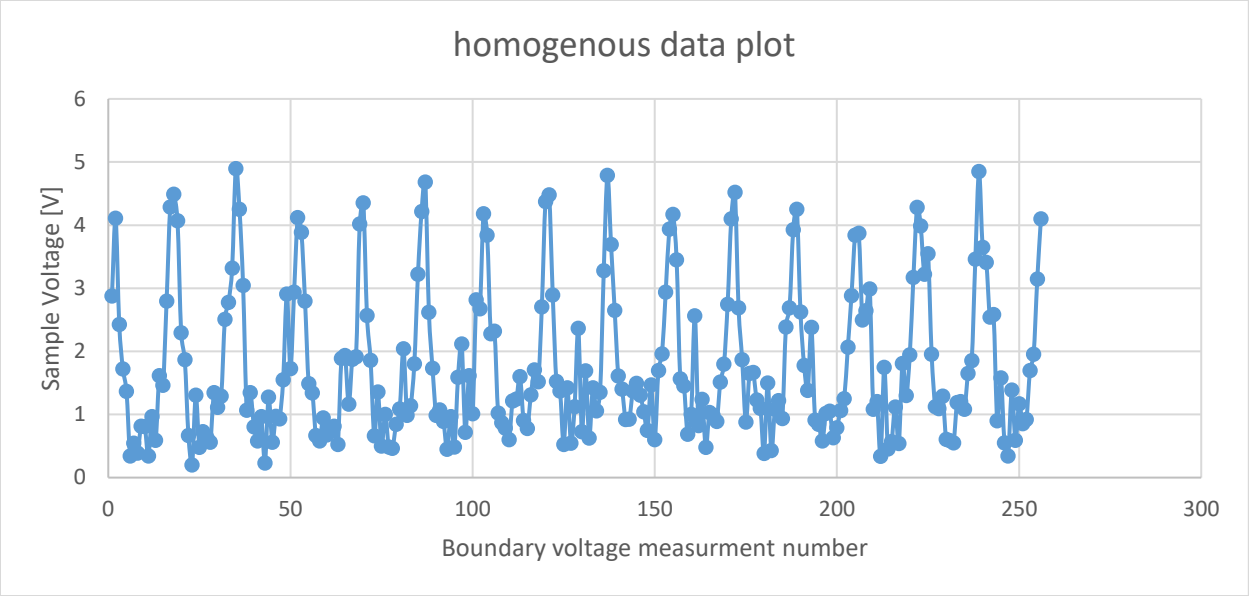

Figure 5- 10: Plot of the voltage profile for a complete measurement frame.

Figure 5- 10 shows that, although the voltage profile is slightly distorted for the large test tank, a U-curve can still be observed. This result is comparable to the voltage profile in [51].

5.6.4 System detectability

An anomaly was placed inside the test tank, when the tank was filled with pure distilled water of volume 942.3 cm^3 at room temperature, and a measurement frame was recorded. The difference between this new data and those in Figure 5- 11 is shown below.

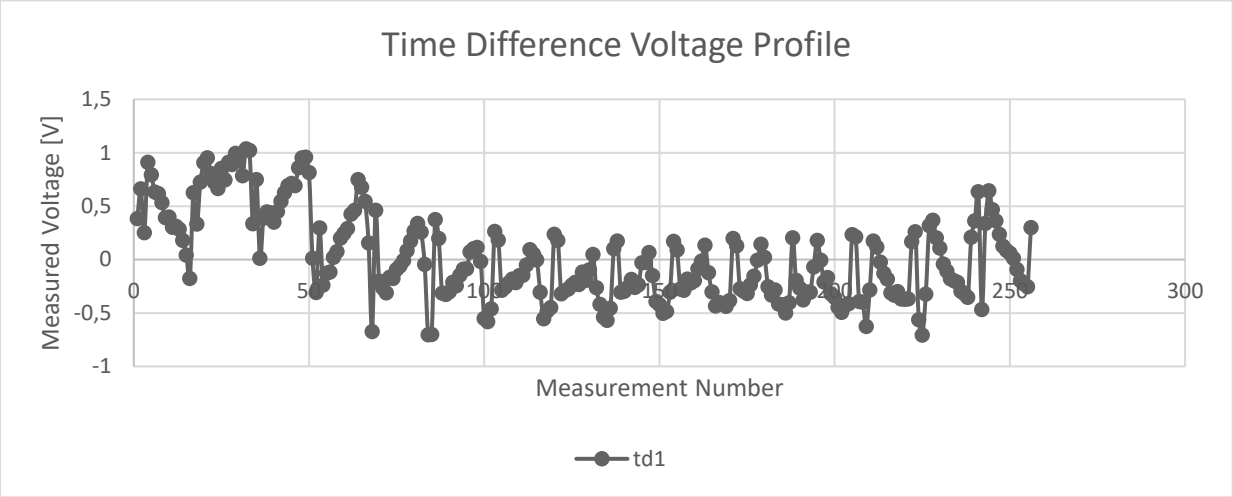

Figure 5- 11: Shows the time difference data between the homogeneous data and data recorded when an anomaly was placed at electrode 3. The graph shows clear difference data and distinguishability.

Figure 5- 11 shows the time difference data when adding an anomaly at electrode 3. The graph clearly shows that there has been a change in the internal impedance distribution of the test tank, and that this change occurred approximately at electrode 3; biggest changes occurred during the third injection cycle. This shows that the system is able to accurately distinguish between a homogeneous medium and an inhomogeneous medium. It also shows that the system has accurate localization properties and the change in data has a peak difference at electrode 3. This agrees with the fact that a peak in the measured voltage time-difference profile will occur when injecting current through the electrode that is closest to the anomaly (when considering Maxwell's equations and observing how a change in impedance will affect the measured potentials at the boundary closest to the anomaly), which is in this case electrode 3.

Below are a few time difference data plots for an anomaly placed at different positions. These additional plots are here to justify that, indeed, the final assembled system is able to detect a change in impedance in the test tank.

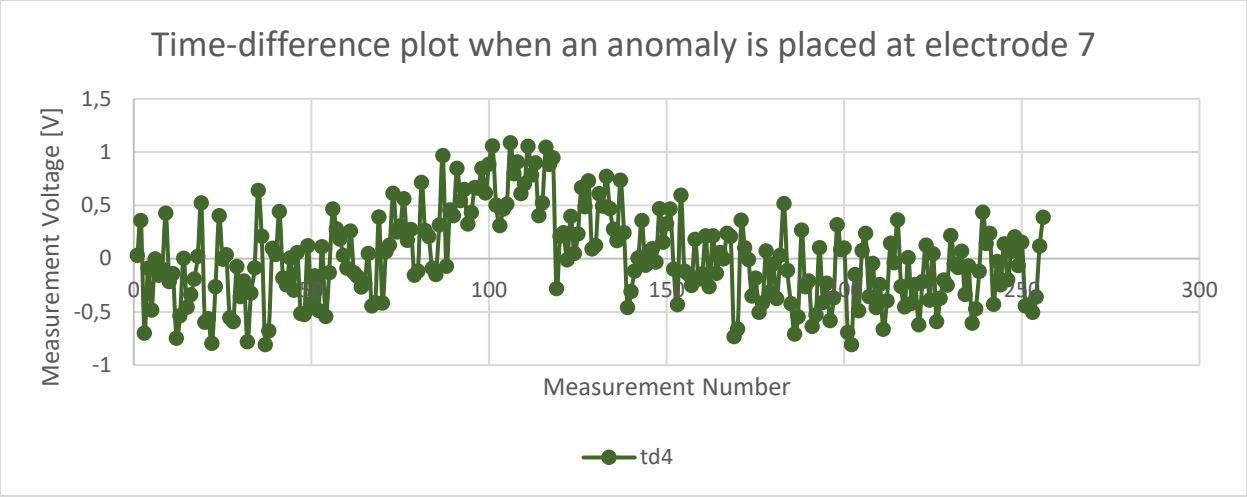

Figure 5- 12: Shows the time difference voltage graph when the anomaly is placed at electrode 7.

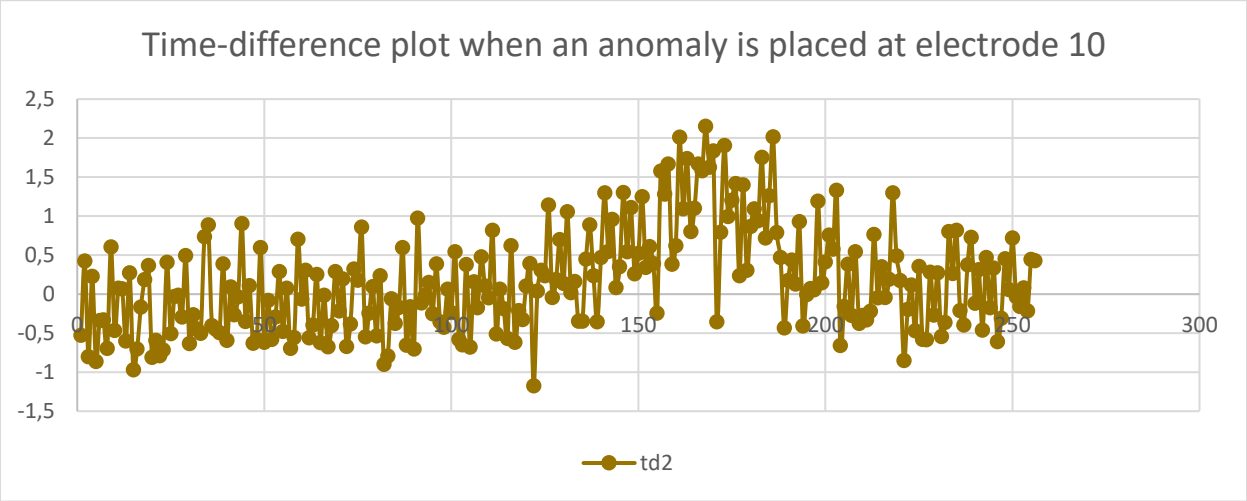

Figure 5- 13: Shows the time difference voltage graph when the anomaly is placed at electrode 10.

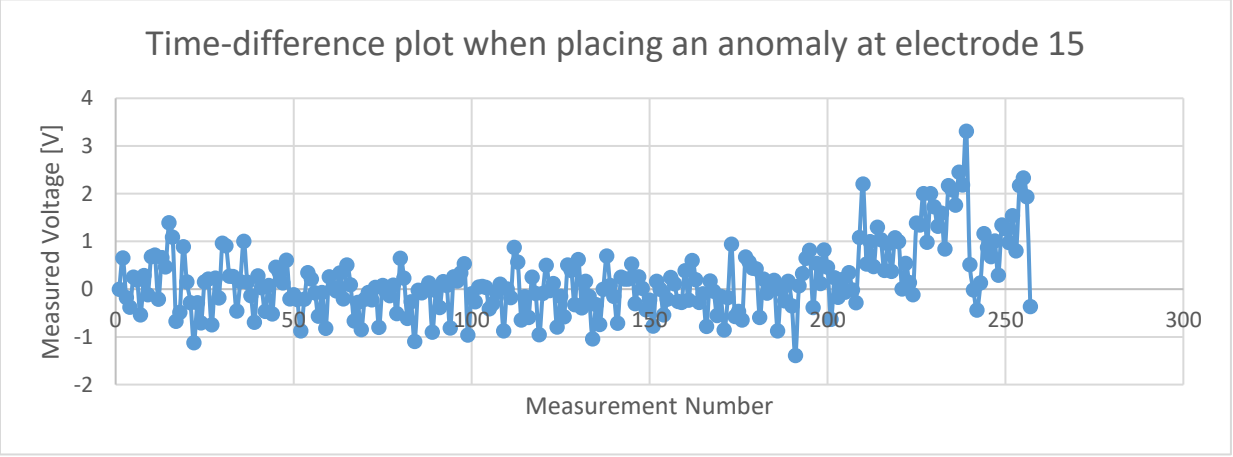

Figure 5- 14: Shows the time difference voltage graph when the anomaly is placed at electrode 15.

From the graphs above, it is evident that the system can detect an anomaly at random positions within the test tank. Furthermore, these plots were obtained by using an adjacent current stimulus pattern in the center plane only and simultaneously measuring the boundary potentials. On the other hand, there is no need to redo this test for the cross plane injections or for a 90 degree stimulus pattern, because those additional tests will not provide any new information about the system hardware. Instead, it will only show how well the anomaly is detected, which is reserved for a separate chapter. Moreover, the peaks in the measured time-difference plots, above, all occur when injecting current at the electrodes that are closest to the anomaly.

In addition, to account for the non-symmetrical nature of the test tank caused by errors in the electrode positions, 3D imaging could be employed. However, the scope of the research is limited to 2D imaging and to answer the question on the effects of dual current injections on the reconstructed images, a three plane tank is essential. Additionally, filters, difference imaging and weighting methods will be applied to the measured data to reduce the effects of scattered current paths.

5.7 Summary

This chapter dealt with the system hardware performance tests, discussed in Chapter 2, that were executed to conclude that a working EIT system was successfully designed and assembled. Each subsystem, passed the tests that were applied, to ensure correct operation. These subsystems are: Mirrored Modified Howland Current Source (MMHCS), Current Multiplexer circuits, Phantom Test Tank, Instrument Amplifiers and Analog-to-Digital Conversion Units. All tests were designed to check how closely the system compares to the results of the simulations done in Chapter 4. The following conclusions were drawn from these tests.

Table 5- 2: Table of the tests and the results from these test that were applied to the subsystems and assembled EIT system.

Subsystem	Reason for test	Result
MMHCS	To test that the current remained constant over a load resistance range that is above the expected test tank load.	Passed. Produced a constant supply current of 1mA for resistances up to 25kΩ and frequency of 0.93MHz
Current Multiplexer Circuit	To test that the multiplexer outputs the supplied current to the correct channel, as selected by the multiplexer switching code.	Passed. Output signal was identical to the multiplexer input signal. All channels work as expected.
Phantom Test Tank	To test for water leaks, noise levels in the wires, electrode position errors and the homogeneous solution resistance.	Passed. No water leaks. 4mm electrode position error. Acceptable noise from the wires.
Instrument Amplifier	To test that the correct gain is applied to the difference between the input signals, irrespective of the signal signs and to check that the input current is zero.	Passed. Correct gain of three was observed for various input combinations. Zero input current was observed.
ADC	To test input noise and DC-offset voltages and to observe that the correct voltage is measured, given a known input voltage.	Passed. Acceptable noise identical to the noise from the wires. Which means that the noise is primarily from the wires. The correct input voltage waveform was measured.
Assembled EIT System	To test the overall noise and DC-offset voltage and to check that a U-curve voltage profile is established for a single measurement frame; when using adjacent current stimulation.	Passed. Acceptable noise and DC-offset voltage. Observable U-curve established.

The assembled EIT 16-bit and 24-bit systems are shown in Appendix B, Figure B- 7 and Figure B- 8.

6 Image reconstruction algorithm

This chapter covers the program flow for the control module and the reconstruction algorithm. The Arduino Due has been selected as the control module of the system. Furthermore, the job of the control module is to send communication bits to the multiplexers and the ADC units, and send the samples from the ADC to the PC for image reconstruction. Therefore, it must ensure that the system operates without error. The flow chart of the C program that is flashed to the controller is shown in Figure 6- 1.

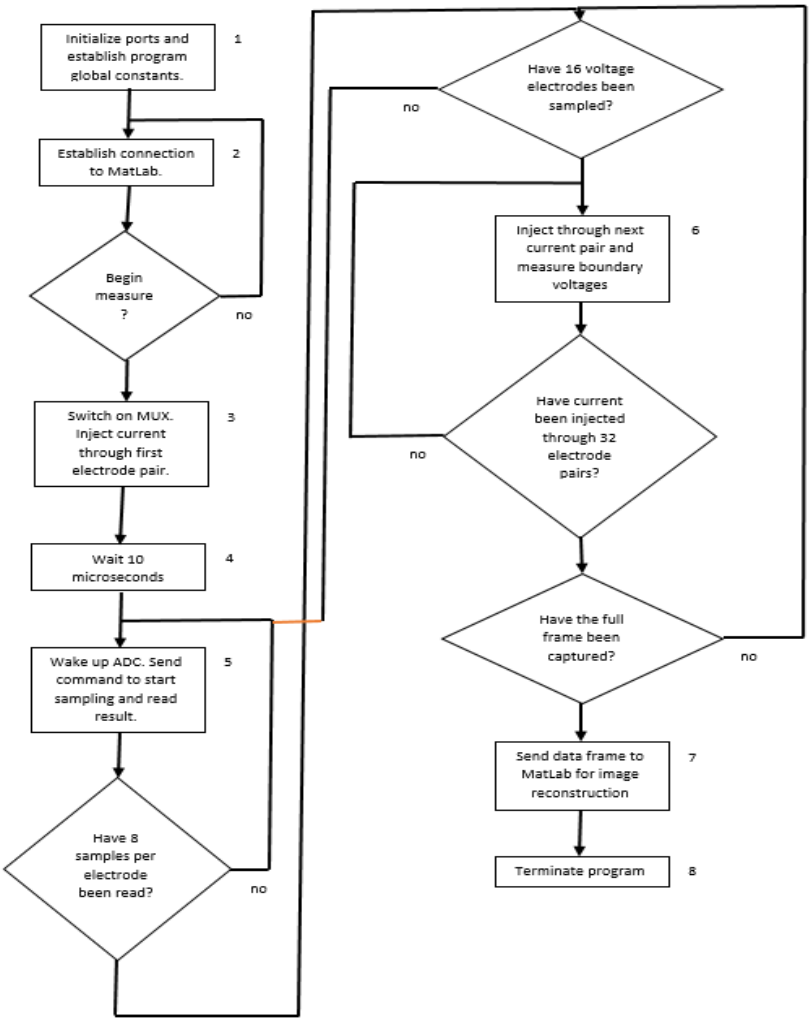

Figure 6- 1: Arduino Program flow chart. It shows the different states within the program and the paths of logical decisions that are made to ensure that the program allows the board to correctly control the system.

Figure 6- 1 shows the program flow chart used to correctly control the Arduino board and to ensure that the EIT system functions synchronously. State 1 sets up all ports and pins of the Arduino to digital, analog, input or output states and initializes the onboard SPI and sets global constants such as the least significant bit and DC-offset compensation for the ADC. State 2 opens the serial monitor to establish a connection between the board and MATLAB. It also initially turns off all circuits to reduce power consumption. Before moving to state 3, the board first has to check if the MATLAB code has instructed it to begin the measurement process. State 3 switches on the multiplexers and injects current through the first current pair. State 4 places the system in a wait state, to allow the transients of the system to settle before taking measurements. State 5 wakes up the ADC and sends a command to start sampling the measured boundary voltages and read the result. Before executing state 6, the board must first check if 8 samples per measured signal have been captured, to ensure that sufficient data is measured to determine the amplitude and phase of each measured signal; for 16 measurement electrodes. State 6 injects current through the next current electrode pair and measures the boundary voltages for this injection. Following state 6, the system checks if current has been injected through all possible current electrode pairs, for both current injection patterns, and if a full measurement frame has been recorded. State 7 sends the complete measured frame of data to a PC for image reconstruction. State 8 terminates the program and waits for a wake up byte from MATLAB; when a new frame needs to be measured. After completing a measurement frame, the program restarts the system into state 1 and the process, explained above, is repeated.

After completing the control code, a reconstruction algorithm is coded in MATLAB using EIDORS image reconstruction libraries. The duty of this algorithm is to connect to the Arduino, send a ‘begin measure’ byte, read the samples and save these samples to a .csv file. This file is then called, and the samples are saved to appropriate variables which are used to compute the internal impedance distribution of the phantom test tank, and to reconstruct images from these samples. This forms a solution to the EIT problem.

To solve the EIT problem involves five steps:

1. Generate a forward model.
2. Produce an image of this forward model.
3. Measure and sort the data from the EIT system.
4. Generate an inverse model, and link it to the forward model image and the measured data.
5. Display the reconstructed image, by solving the inverse problem.

The forward model uses the FEM to generate a triangular mesh network of the test phantom, using Delaunay meshing [23]. An image of the forward model is produced from the physical model's parameters, which is the same image used in the inverse model, including the inhomogeneity. The data is collected from the EIT system and sent to MATLAB via a serial port, and MATLAB sorts this data into an array and saves it to a .csv sheet. Following the data sorting process, the inverse model is then generated from the homogeneous and nonhomogeneous data and the result is used to reconstruct an image.

6.1 Solving the forward problem of EIT

EIDORS together with NetGen provides several pre-written libraries that aid the user in generating a forward model, which may later be used to generate the inverse model. But, first one needs to measure the parameters of the real phantom test tank. The following table lists these parameters.

Table 6- 1: Physical Test Tank Parameters

Physical Tank Parameter	Parameter Value
radius	7.5 cm
Number of electrodes (n_elec)	16
Number of voltage measurement rings (n_rings)	1
Height (height)	25 cm
Voltage electrode radius (elec_radius)	0.25 cm
Applied current (current)	1 mA
Contact Impedance (Zc)	Negligible (the current and voltage electrodes are independent)

In addition, the user-desired simulation parameters are tabulated below.

Table 6- 2: User-defined simulation parameters

User-defined simulation parameter	Value
Mesh refinement (mesh_refine)	0.15
Electrode refinement (elec_refine)	0.005
Homogenous conductivity	1 (general assumption) normalized to 0

Based on the parameters above, the following function is called in MATLAB.

$$fmdl = ng\_mk\_cyl\_models([height, radius, mesh\_refine], [n\_elec, n\_rings], [elec\_radius]) \quad (6.1)$$

The function above is used to generate a forward model for the problem, based on a common cylinder model. In this function, the physical dimensions of the test tank is defined.

Assigning the user-defined conductivity, results in the following forward model image.

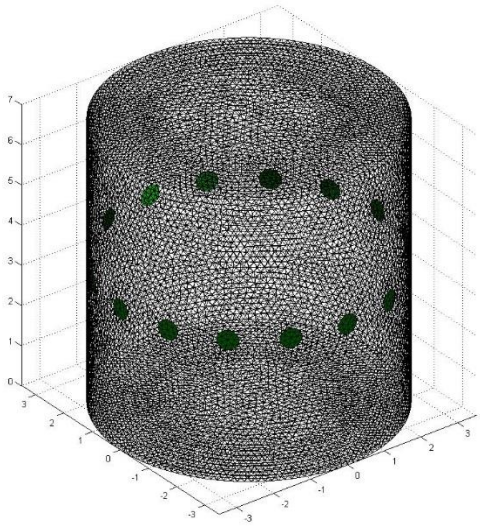

Figure 6- 2: Generated Forward Model. This model only includes the voltage measurement electrodes.

Figure 6- 2, above, shows the forward model which was generated (within EIDORS using NetGen) to represent a discrete model of the phantom test tank. EIDORS creates a mesh image, based on the FEM, which is filled with the values of a user-defined conductivity to generate a homogeneous forward model. The mesh refinement, electrode dimensions, electrode spacing and current injection method was chosen to produce a model that is a good representation of the physical tank. Furthermore, a 2D model of this forward model was designed, to restrict the problem to two dimensions.

Following the mesh generation step. The next step focuses on solving the inverse problem of EIT.

6.2 Solving the inverse problem of EIT

After generating a forward model, then acquiring the data from the test phantom, the next step involves producing an inverse model which is then used to reconstruct images of the test tank; known as the *inverse problem* of EIT. There are two primary algorithms that are used to solve the inverse problem; *Static imaging* and *Difference imaging*. Static imaging attempts to reconstruct an image of the internal impedance of an object, by estimating the absolute impedance of that object at an instant in time. Difference imaging attempts to reconstruct an image of the internal impedance layout of the object, by using the measured time or frequency difference boundary potentials. Difference imaging has the advantage, over static imaging, of being able to observe how the internal impedance of an object changes over time or frequency; which is relevant for biological applications of EIT.

Furthermore, it was established (in chapter 2) that the forward model produces a mesh of *n* triangular elements, with each element holding a single impedance value. However, the amount of boundary voltages that one may measure is limited by the boundary of the object. Which means that the problem of estimating *n* internal impedance values, using *m* (where *m* << *n*) measured voltages, is a severely ill-conditioned problem. These types of problems are highly unstable and require pre-conditioning to achieve a desired level of output stability; to overcome the ill-posed nature of the problem. A common method to solve this problem is to use prior information, such as assumptions and problem constraints, while carefully introducing a tradeoff between solution accuracy and system stability; a method commonly called *Regularization* [9]. The solution to the forward problem provides the prior information and a regularization hyper-parameter may be used to regularize the problem.

In addition, the EIDORS libraries have several functions that can aid the user in creating the inverse model and later solving the inverse problem.

Hence, calling the following function, returns the inverse model of the EIT problem.

$$imdl = mk\_common\_model('a2d2c', [n\_elec, n\_rings]) \quad (6.2)$$

In the function above, an inverse model of the EIT problem is generated from a library of common 2D models. The type of the model is defined by the string '*a2d2c*', which corresponds to a 1024 element mesh, 2D model with point voltage measuring electrodes.

The next step is to link the inverse model with the forward model (previously produced), shown below.

$$imdl.fwd\_model = fmdl \quad (6.3)$$

After producing a forward and inverse model, the next step is to select the stimulation and measurement patterns followed by computing the Jacobian; the details of which have been discussed in Chapter 2. In MATLAB, the following function should be called to compute the Jacobian, given the inverse model.

$$J = calc\_jacobian(calc\_jacobian\_bkgnd(imdl)) \quad (6.4)$$

And, the prior matrix:

$$iRtR = inv(prior\_noser(imdl)) \quad (6.5)$$

A Noser prior filter was selected, based on the need to filter interferences that may appear within the reconstructed images. Other filters were tested such as the Tikhonov, Laplace and High-Pass filters. However, these filters either produced poor localization properties or required too much computer RAM space. The Noser filter provided the best trade-off between artefact filtering and detectability.

After choosing a prior filter, the next step is to select a hyper-parameter for the regularization process. The value of the hyper-parameter is used to regularize the problem or remove some artefacts. The method used in this paper is the Heuristic Selection method described in Chapter 2. This method involved choosing an initial hyper-parameter value of 1 (one) and reconstructing an image from the measured data. By inspection of the reconstructed image, the hyper-parameter was varied until the image correctly presented the detection of an anomaly and presented the least amount of image artefacts. This process was repeated for each subsequent anomaly position (total of eight positions) and the average of all selected hyper-parameters was 0.8. This value was then used as a fixed hyper-parameter for further image reconstruction.

Consequently, the next steps involved reconstructing an image using measured data and the selected averaged hyper-parameter. To test the code, the average of 20 (time-differenced)

homogeneous data sets were used to reconstruct an image, to show the amount of variation in the measured frames, shown in Figure 6- 3.

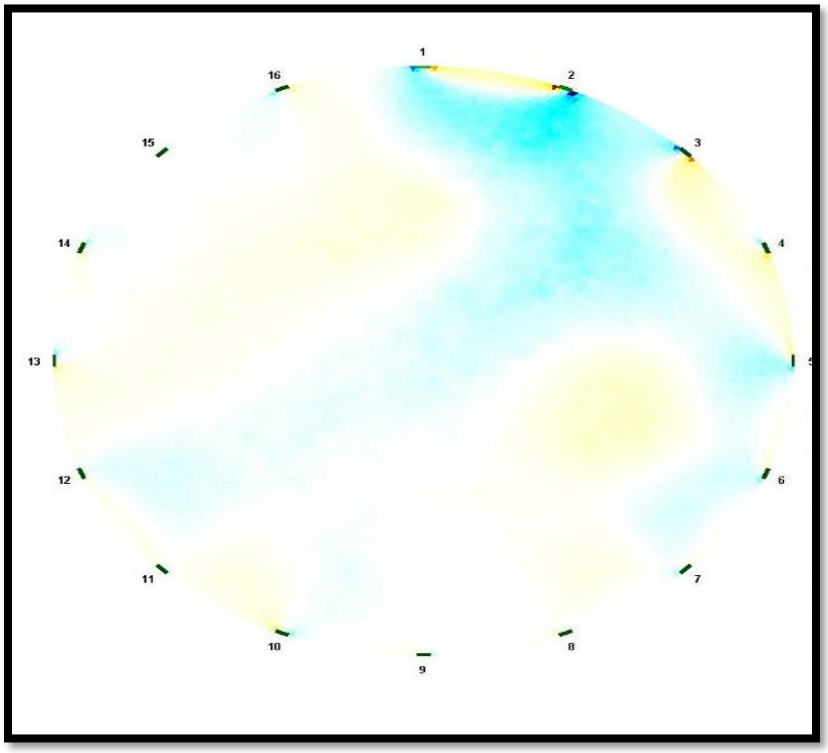

Figure 6- 3: Reconstructed image of the time difference between homogeneous measurements. It shows how closely the measurements are to one another; by producing a near complete white image.

Figure 6- 3 shows the reconstructed image from the homogeneous data sets, obtained when applying a 1 mA current at 1 kHz into a tank filled with 942.3 cm^3 of distilled water at room temperature. It clearly shows that the complete EIT system together with the MATLAB image reconstruction algorithm, produce repeatable measurements as there are no distinctive artefacts, in the image, caused by a variation in the measured data for a homogeneous medium.

6.3 System symmetry, accuracy and repeatability

To further prove that the system is able to produce repeatable results, the following images were generated from multiple measurements, from a selection of anomaly positions using the 24-bit ADC. The diameter of the anomaly was 26.6 % of the diameter of the test tank.

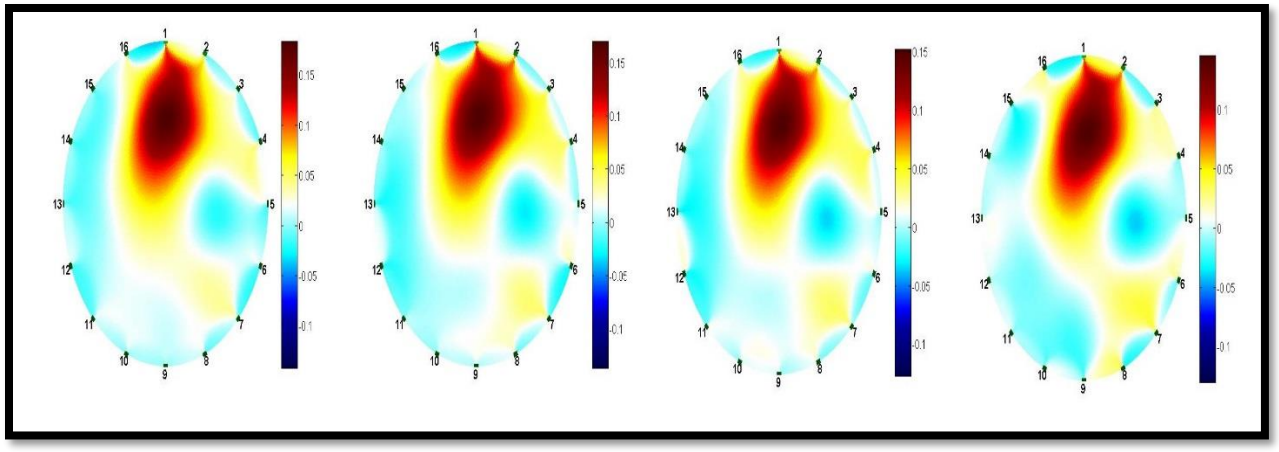

Figure 6- 4: These images were reconstructed using four time difference datasets. Recorded at different instances for an anomaly placed at electrode 1.

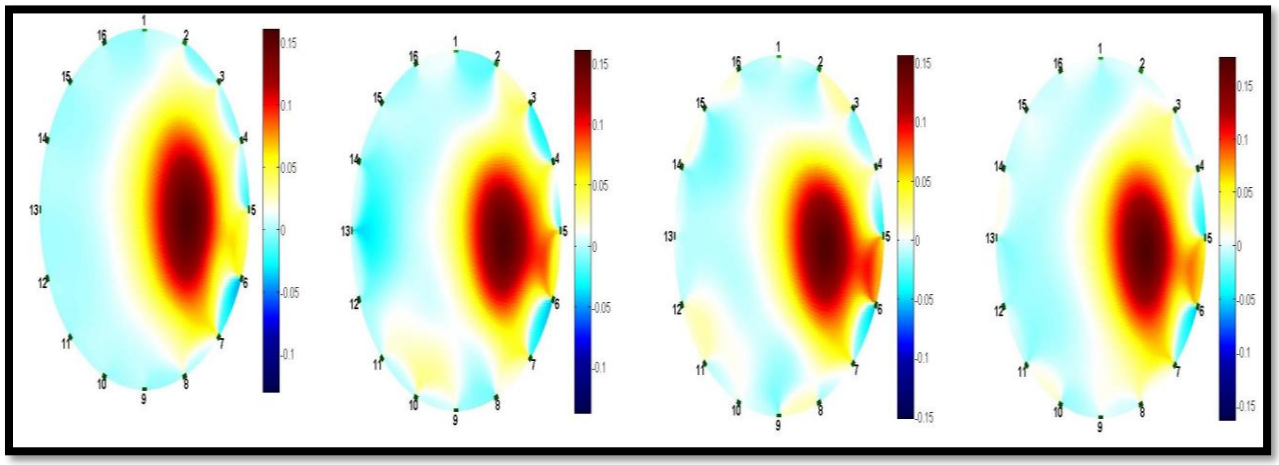

Figure 6- 5: These images were reconstructed using four time difference datasets. Recorded at different instances for an anomaly placed at electrode 5.

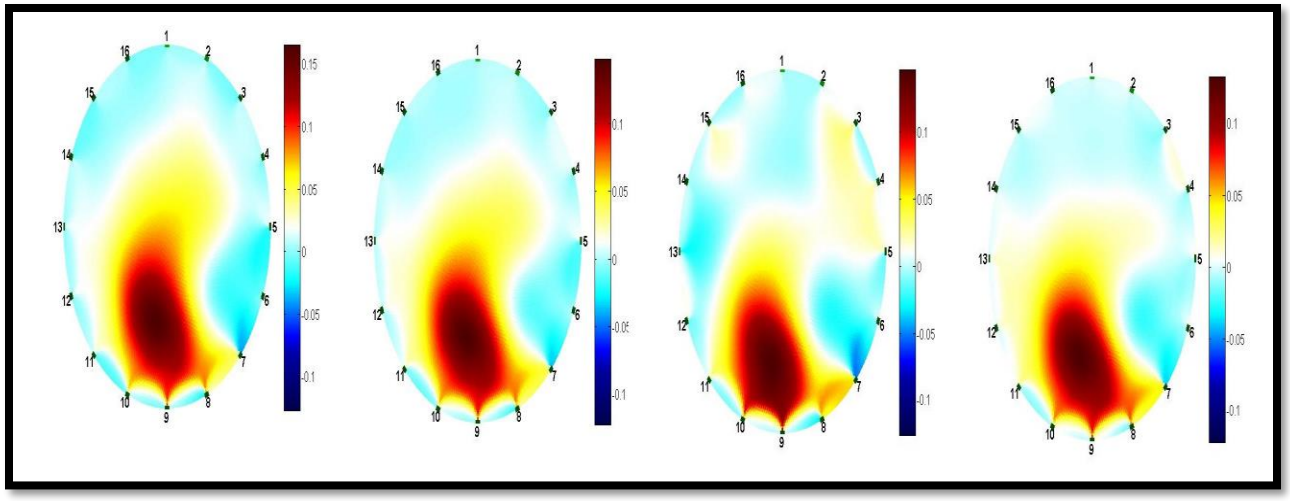

Figure 6- 6: These images were reconstructed using four time difference datasets. Recorded at different instances for an anomaly placed at electrode 9.

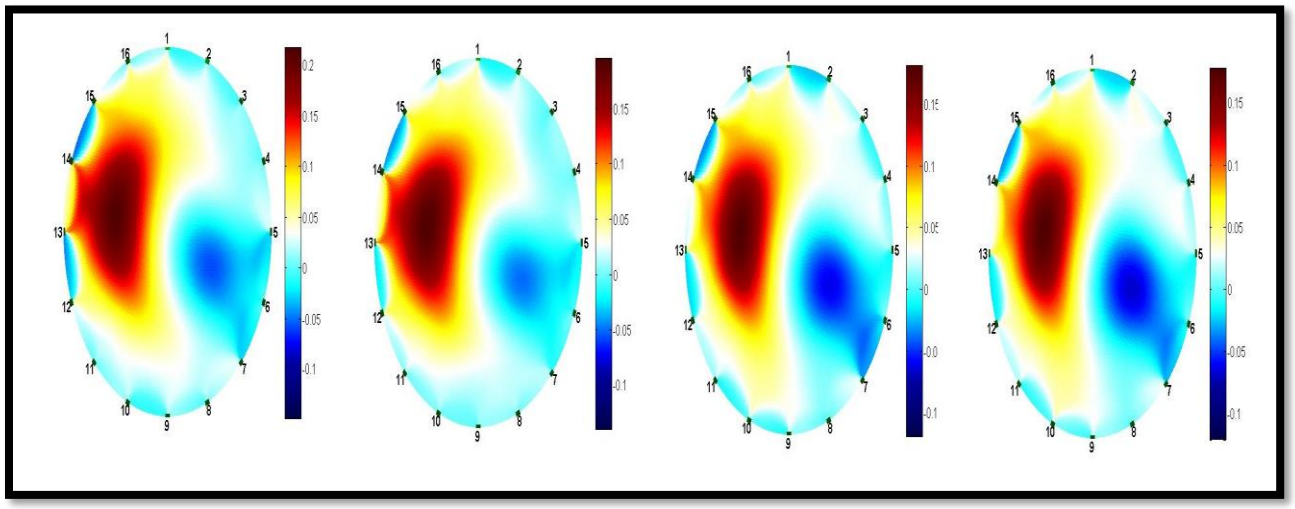

Figure 6- 7: These images were reconstructed using four time difference datasets. Recorded at different instances for an anomaly placed at electrode 13.

The four figures above show four reconstructed images, per figure, for the selected anomaly positions. These images were generated from independent measurement frames at different times. The images, for a given anomaly placement, are identical. This is observed in the color scales which are identical for each image, irrespective of the anomaly placement, and that the location and size of the detected anomaly are identical in each image. This shows that the same anomaly impedance was measured during all frames.

Furthermore, the images show adequate system symmetry, which means that the image reconstruction of an anomaly placed in a given position should be the mirror image of that which is reconstructed to show an anomaly that is placed diametrically opposite. For the images presented above, Figure 6- 4 and Figure 6- 6 are mirror images and Figure 6- 5 and Figure 6- 7 are mirror images. Obviously, these images are not an exact mirror of each other (due to an error in the electrode positions), however, the images do show adequate symmetry. Furthermore, some images have visible artefacts such as the dark blue circle in Figure 6- 7. This is caused by the inclusion of unreliable data; data which is embedded in the measured noise signal amplitude. To remove this false positive anomaly location, is to place a lower threshold on the measured data. Consequently, placing a threshold on the measured data will not reduce its integrity. Instead, it is used to remove all recorded values that fall below a user-defined magnitude. This defined magnitude is chosen to lie slightly above the expected noise level, shown in Chapter 5. In addition, the images above show that, for the given anomaly, the maximum amplitude of the time difference data for the different anomaly positions is 0.15 [V]. Furthermore, the expected amplitude of the noise signal is 4 mV_p, as shown in Chapter 5. This means that the lower threshold should be slightly above 4 mV_p to remove all measured amplitudes that lie within the noise signal, and thus, is not considered a reliable reading. From this point onwards, a threshold of ±45 mV will be incorporated into all data frames to be measured and used for image reconstruction (Chapter 7). This is a reasonable threshold value, based on the quarter maximum threshold used in [42]. Consequently, any measured time-difference data point that lies below 4.5 mV will be included in the data frame as a zero magnitude point and as such, places a limit of the minimum impedance detection capabilities of the system. Additionally, for the EIT system which is designed to measure voltage differences in the range of ±5 [V], has a system measurement accuracy of 0.045 %. This is well within the system design constraints, which is 0.9% as shown in Chapter 4. Furthermore, the 16 bit resolution system required a higher threshold because more noise was present in the 16 bit resolution dataset (approximately 25 mV_p noise was measured, hence, a threshold of 30 mV_p was selected), compared to the 24-bit dataset. This is due to the filters that were used in the system design. The 16-bit ADC system did not incorporate any filters and the 24-bit ADC used a notch filter, which attenuates more noise.

6.4 Summary

This chapter focused on the control and image reconstruction algorithms that were implemented onto the DCS EIT system. First, the control code flow was presented, to show the different control states of the system, which include the method used to sample the measured voltage signals and to inject current through the correct electrode pair. Secondly, the image reconstruction algorithm was presented. It was shown that standard EIDORS libraries were used to generate forward and inverse models of the problem, and the Heuristic Selection method was used to select the best performing hyper-parameter from a set of chosen values. Finally, a few images, of the actual impedance distribution of the system, were reconstructed. The first image showed that there were no significant differences between 20 time-differenced data frames of the homogeneous solution in the tank. Further images were presented to show the repeatability of the system, when detecting anomalies. These images showed that the system recorded identical impedance, location and size of a selected anomaly. Artefacts were present in some images, and a method of thresholding was proposed to eliminate them. This thresholding of the measured data was then used to compute the systems measurement accuracy, which is 0.045 % and 0.6 % for the 24-bit and 16-bit systems (respectively); well below the system design requirements. It was then stated that different threshold values were used for the 16 and 24 bit-resolution systems, which only proves that more noise was present in the 16 bit system, compared to the 24 bit system; as the 16-bit ADC did not incorporate any filters and the 24-bit ADC incorporated a notch filter, which attenuated the measured noise. To this point, the physical system and its algorithms were thoroughly tested. The system passed all tests and showed a good level of reliability and measurement accuracy. Hence, the next step is to analyze the results of the experiments.

7 Experimental results

The results obtained from the complete operation of the EIT systems are presented in this chapter. First, comparisons will be made between the images reconstructed from 16- and 24-bit systems. The result of this comparison will dictate which ADC data acquisition module is adequate for further testing of the hypothesis. These tests are to identify which of these two systems will produce the least reconstruction errors in the size and position of an anomaly, placed at different positions. After selecting the preferred option of the two acquisition modules, a comparison of the image quality will be made between single plane stimulation and dual current stimulation (DCS) protocols. Finally, the errors in the reconstructed images from the DCS system will be compared to the errors in the reconstructed images from other modern research papers, which employ a single plane stimulation protocol. A conclusion will then be drawn from these comparisons to answer the research questions and to confirm or reject the research hypothesis.

7.1 24-bit versus 16-bit data acquisition

In this section, a 24-bit data acquisition system will be compared to a 16-bit data acquisition system. The only differences between these two systems, is that the 24-bit system uses a LTC2418 24-bit ADC, by Linear Technology, which is controlled by an Arduino Due microcontroller, and the 16-bit system uses a µDAQ data acquisition board by Eagle Technology, which plugs directly into the computer and is controlled by MATLAB. Furthermore, both systems performed adjacent single plane current stimulation using a 1 mA current with a 1 kHz frequency.

Furthermore, the 16-bit system has 65535 voltage measurement levels and the 24-bit system as 16777215 voltage measurement levels, which means that the 16-bit system can measure voltages as low as 152.59 µV and the 24-bit system can measure voltages as low as 0.60 µV; for a measurement range of ±5 V. However, as stated in Chapter 6, due to the noise levels in the system, a threshold is used to remove all unreliable data; data that is embedded in the noise signal. From chapter 5, the voltage measurement threshold is 0.0045 V and 0.03 V for the 24-bit and 16-bit systems, respectively. These thresholds are above the minimum measurable voltages for either system. Therefore, it is predicted that, due to the measurement voltage thresholds used, the two systems will produce identical image qualities. Furthermore, if the thresholds were not

used, then more noise will be included into the measurements, and it will be a difficult task to compare the reconstructed images. Moreover, for measurements above the threshold, the percentage difference between the measurements of the two systems is:

$$\frac{V_{24bit(min)} - V_{16bit(min)}}{V_{span}} * 100 = \left(\frac{152.59\,V - 0.6\,V}{10\,V}\right) * 10^{-6} * 100 = \ 0.00152\ \% \qquad (7.1)$$

This result is too small to make any significant improvement in the images, because the measurement accuracy (based on selected voltage thresholds) is 0.045 % and 0.6 % for the 24 and 16-bit systems (respectively).

In addition, to compute the size and position errors for the reconstructed images, from these two systems, the method used in [6] will be used, because it provides a good representation of the manual measurements that were used in this research; to obtain the image reconstruction errors. In [6], the reconstructed image is read in MATLAB, converted to grayscale (no information is lost in this conversion because the grayscale image includes all RGB data from the original image) and inverted to set all pixel intensities that did not detect an anomaly or image artefact, close to zero, and all other pixel intensities to a scalar multiple (a scalar of less than 1) of 255. The image pixels were then plotted along a center horizontal (x-axis) or vertical (y-axis) line; extracted from the image matrix. From the pixel intensity plot, the diameter and centroids of the anomaly and tank can be estimated. This data is then used to compute the size and position errors for the reconstructed image.

The results of this experiment is shown below.

An anomaly was placed in the following positions:

a) Actual Anomaly Position b) 16-bit Reconstructed Image c) 24-bit Reconstructed Image

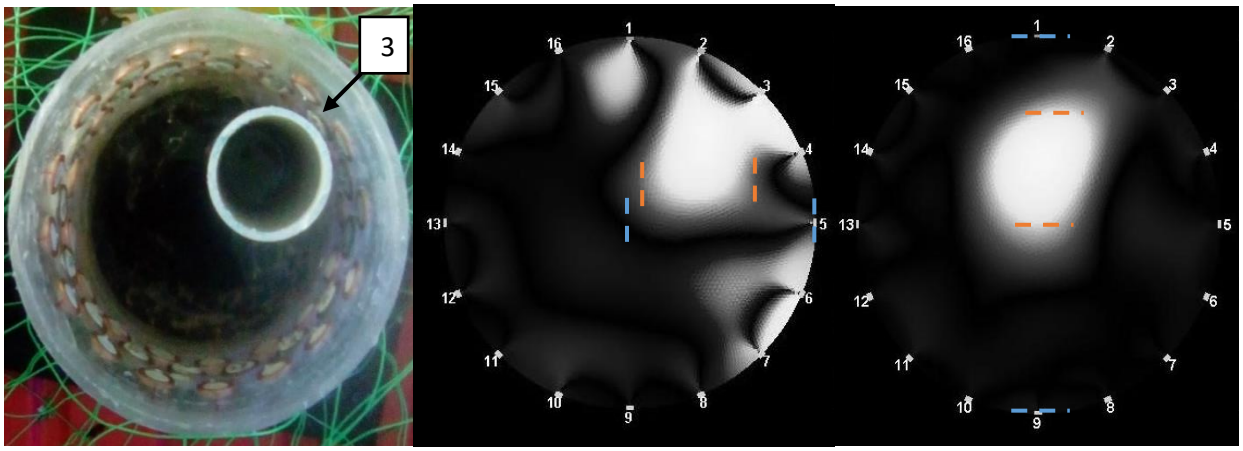

Figure 7- 1: shows the actual anomaly position at electrode 3 and the 16-bit and 24-bit reconstructed Images using an inverted grayscale.

a) Actual Anomaly Position b) 16-bit Reconstructed Image c) 24-bit Reconstructed Image

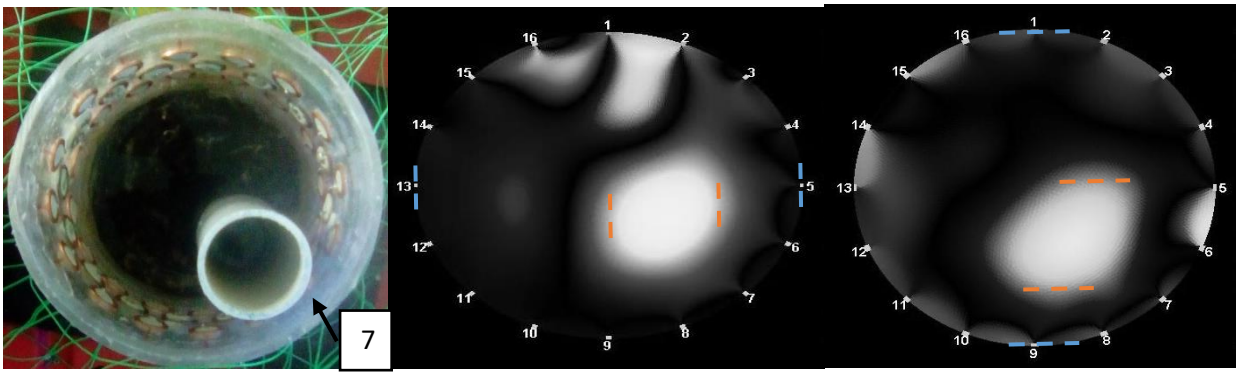

Figure 7- 2: shows the actual anomaly position at electrode 7 and the 16-bit and 24-bit reconstructed Images using an inverted grayscale.

a) Actual Anomaly Position b) 16-bit Reconstructed Image c) 24-bit Reconstructed Image

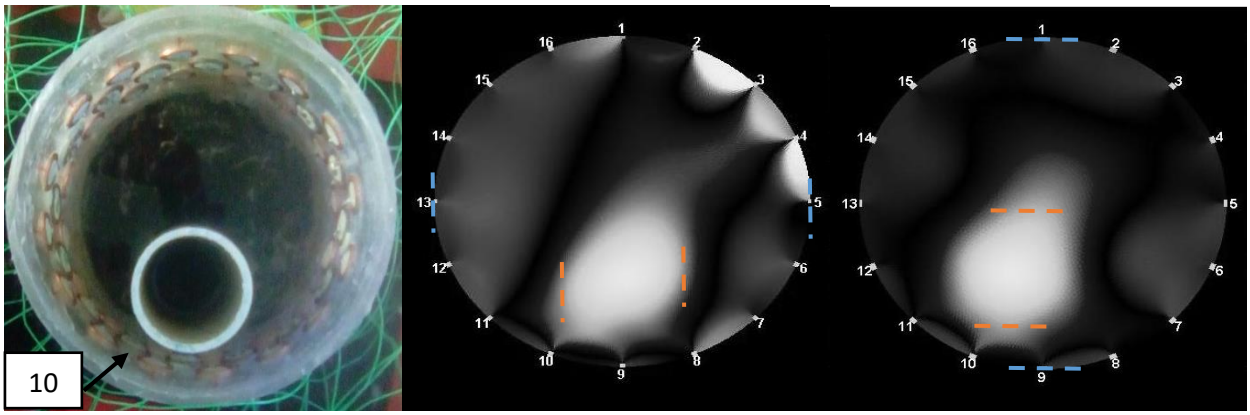

Figure 7- 3: shows the actual anomaly position at electrode 10 and the 16-bit and 24-bit reconstructed Images using an inverted grayscale.

a) Actual Anomaly Position b) 16-bit Reconstructed Image c) 24-bit Reconstructed Image

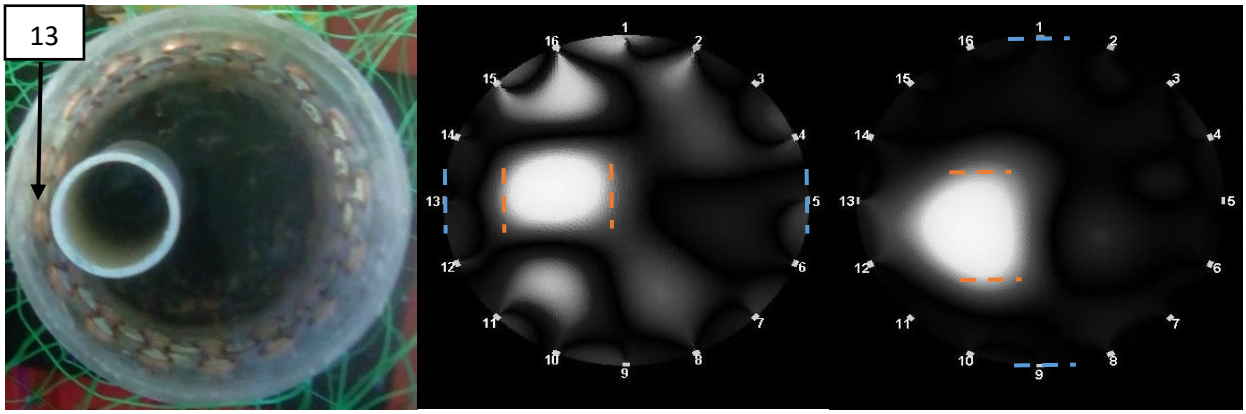

Figure 0-1: shows the actual anomaly position at electrode 13 and the 16-bit and 24-bit reconstructed Images using an inverted grayscale.

From the pixel intensity plots in Appendix C (Figure C- 1 to Figure C- 8), the two outer data points (accompanied by blue dashed lines) are used to estimate the diameter and the center of the test tank. The two inner points (accompanied by orange dashed lines) are used to estimate the diameter of the anomaly and the third point is an estimation of the centroid of the anomaly. These estimates are then substituted into the equations for size and position error, given in Chapter 2. The following table summarizes the computed errors for each system.

Table 7- 1: Error table for the 16-bit resolution system.

	Anomaly Positions				
Error	At electrode 3	At electrode 7	At electrode 10	At electrode 13	Average Error
Size Error [%]	8.49	7.69	15.26	2.15	8.40 %
Position Error [%]	28.93	6.61	0.98	14.49	13.13 %
Noise Error Ratio [%]	32.44	28.95	31.38	35.21	32.00 %

Table 7- 2: Error table for the 24-bit resolution system.

	Anomaly Positions				
Error	At electrode 3	At electrode 7	At electrode 10	At electrode 13	Average Error
Size Error [%]	1.29	7.52	5.44	4.8	4.76 %
Position Error [%]	10.885	6.036	8.46	3.8	7.30 %
Noise Error Ratio [%]	9.38	11.21	9.67	6.01	9.07 %

The positions of the anomaly within the test tank was chosen to test the ability of these systems to detect anomalies, and to provide an adequate amount of tests to confidently draw conclusive comparisons between the two systems.

From the reconstructed images, and measured data, it was observed that both systems were able to detect anomalies that were placed near the boundary; images were not reconstructed for anomalies at the center because an adjacent current pattern was injected, and based on the results from Chapter 3, it was assumed that poor images would be produced for objects at the center of the tank. As for the capability of these systems, clearly from the tables above, the 24-bit system produced images with a higher image quality compared to the 16-bit system.

Furthermore, as previously stated, based on the measurement accuracy of the two systems, there should not be any significant differences in the reconstructed images. However, the tables above show that the 16-bit system produced images that had size and position errors that were 56.72% and 55.57 %, respectively, greater than those from the 24-bit system. This is a result of the noise levels in the two systems. The 24-bit system used a notch filter in the ADC which allowed much more noise attenuation prior to measurement, compared to the 16-bit ADC, which did not have any filters in the design. It is also noted that, although, a voltage threshold was placed on the measurements, it does not guarantee complete noise immunity. As shown in Chapter 5, the threshold was selected based on the measured and expected noise levels in the system. However, some measurements will have more noise than others, and other noise levels may

exceed the threshold. The latter case explains the added noise in the images. Furthermore, the results show that the notch filter in the 24-bit ADC was able to attenuate an adequate amount of the unexpected noise levels that exceeded the threshold, whereas the 16-bit system did not attenuate the noise. From the average noise error ratios for the two systems, in Table 7- 1 and Table 7- 2, the 16-bit and 24-bit systems contained an average of 32 % and 9.07 % noise, respectively, in the measured signals per channel. This shows that indeed, the amount of noise attenuation in the system affects the quality of the reconstructed images, irrespective of the bit resolution.

Furthermore, placing filters at the output of the 16-bit system is logically assumed to enhance image quality. Hypothetically, if one should design filters for the 16-bit system that will attenuate noise levels to 9.07 % of the measured signals, as was achieved using the 24-bit module, then (as aforementioned) the expected improvement in the image quality will be 0.00152 % lower than the 24-bit reconstructed images. In each regard, the 24-bit system will not provide any significant improvement in the image quality, compared to the 16-bit system, if both systems were able to attenuate the same level of noise. However, it is quite difficult to ensure that both systems are able to attenuate the same amount of noise, exactly.

In addition, several filters having a sharp roll-off is required to attenuate an adequate amount of noise, which translates to several additional months of design, simulations, testing, acquisition, assembly and cost. Accordingly, the hypothesis of this paper does not place any emphasis on the bit resolution, hence, from the results, it is decided that the 24-bit resolution module will be used to sample data for the succeeding tests.

7.2 Single current stimulation versus DCS protocol

From Chapter 3, it is expected that the image quality of the reconstructed images of a dual current stimulation (DCS) protocol is greater than that for a single plane stimulation protocol. It was shown that the DCS protocol was able to detect anomalies at any position inside the test phantom as compared to the single stimulation systems which require a certain injection pattern to enhance the current distribution in a region, so that anomalies can be detected in that region. As stated previously, there is not a single current pattern that produces a uniform current distribution throughout a medium. Some patterns have good current densities in one region, while having

lower current densities in other regions. For this reason, the question on "*whether or not introducing a second current pattern will provide a more uniform current density"*, was put forth.

Intuitively, if a current density has become more uniform throughout the tank, then the size error, position error and distinguishability should improve. Therefore, these quantities will be measured to test that the spatial resolution and image quality have been improved when using a DCS protocol.

Consequently, this section proceeds as follows.

1. The single plane reconstructed images for eight anomaly positions along the boundary of the tank will be presented, and the inverted grayscale image with the corresponding pixel intensity plots will be used to compute the errors. A table will be generated to summarize the size and position errors and the noise error ratio.
2. As above, the size and position error for cross plane stimulation image reconstruction will be computed and tabulated.
3. Based on the errors for the reconstructed images that used single and cross plane stimulation, a weighted average of the datasets for each protocol will be used to produce dual stimulation images. Again, the size and position errors and noise error ratio for the DCS protocol will be tabulated.
4. Objects having non-circular shapes will be placed into the phantom tank and images will be reconstructed using single and dual stimulation protocols.
5. Several objects will be positioned at fixed radii inside the tank and the images will be reconstructed.
6. From all tests, the best protocol will be chosen, and the chapter concluded.

7.2.1 Single plane stimulation

Here images will be reconstructed for eight anomaly positions. The selected center plane stimulation pattern is the perpendicular injection pattern. The test tank was filled with distilled water with volume = 942.3 cm^3. The applied current was 1 mA-peak at 1 kHz. The anomaly material is PVC with a circular hollow cross-section and a diameter of 26.6 % of the diameter of the tank.

a) Actual Anomaly Position b) Reconstructed Image c) Inverted Gray-scale Image

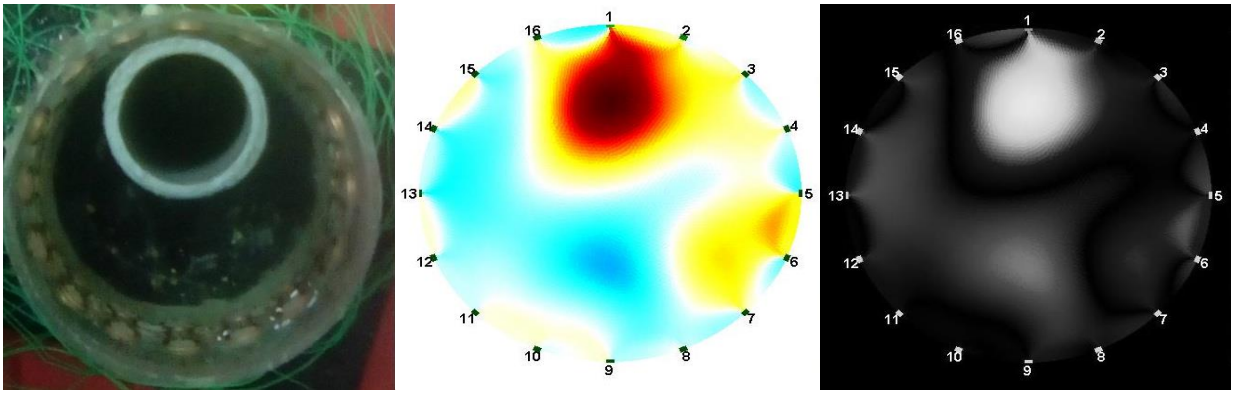

Figure 7- 4: shows the actual anomaly position at electrode 1 and the reconstructed Image and inverted grayscale image.

a) Actual Anomaly Position b) Reconstructed Image c) Inverted Gray-scale Image

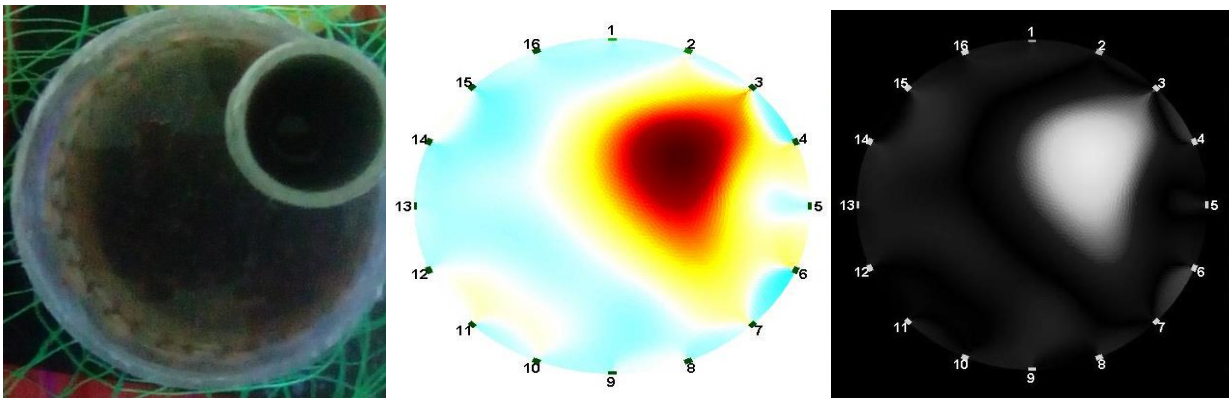

Figure 7- 5: shows the actual anomaly position at electrode 3 and the reconstructed Image and inverted grayscale image.

a) Actual Anomaly Position b) Reconstructed Image c) Inverted Gray-scale Image

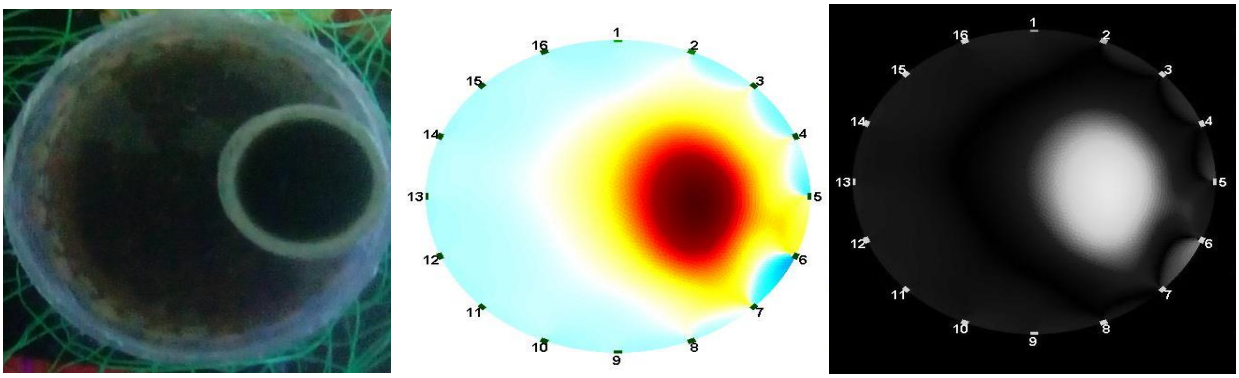

Figure 7- 6: shows the actual anomaly position at electrode 5 and the reconstructed Image and inverted grayscale image.

a) Actual Anomaly Position b) Reconstructed Image c) Inverted Gray-scale Image

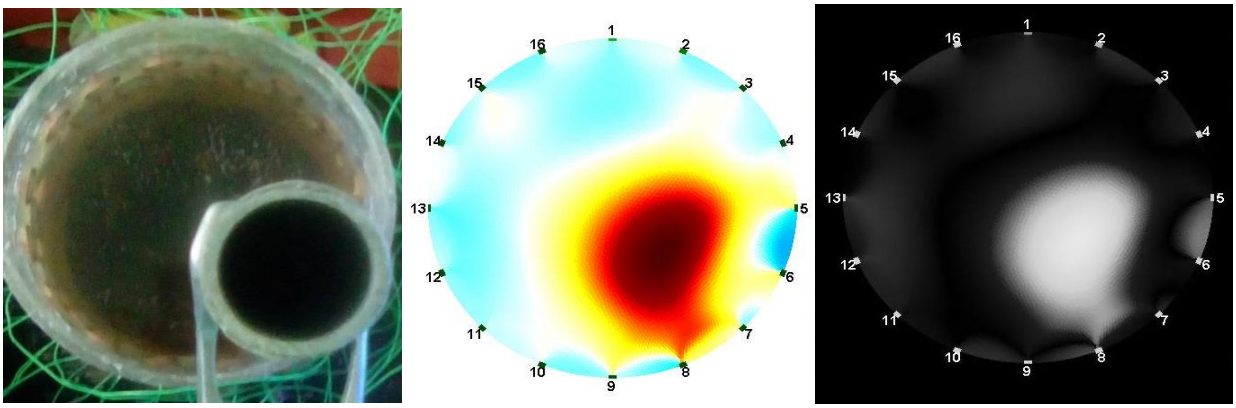

Figure 7- 7: shows the actual anomaly position at electrode 7 and the reconstructed Image and inverted grayscale image.

a) Actual Anomaly Position b) Reconstructed Image c) Inverted Gray-scale Image

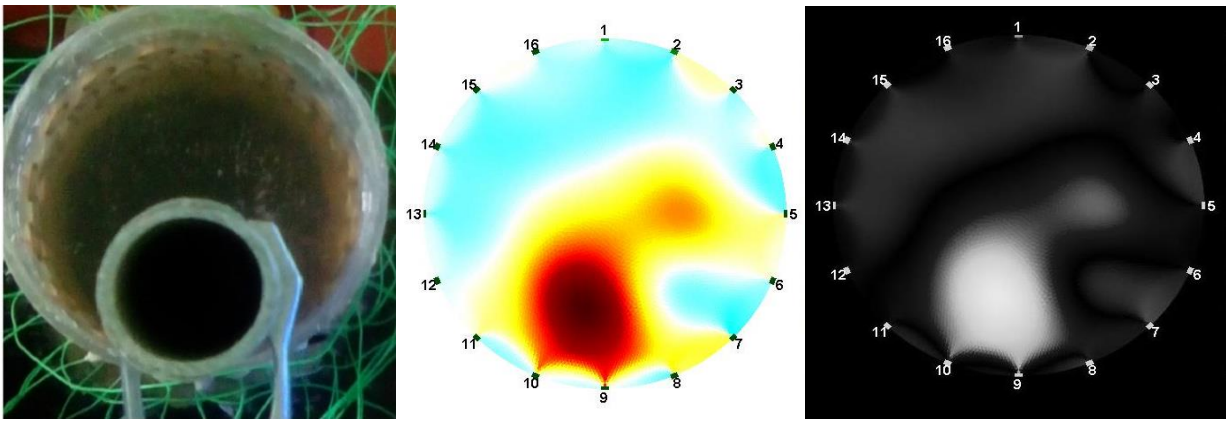

Figure 7- 8: shows the actual anomaly position at electrode 9 and the reconstructed Image and inverted grayscale image.

a) Actual Anomaly Position b) Reconstructed Image c) Inverted Gray-scale Image

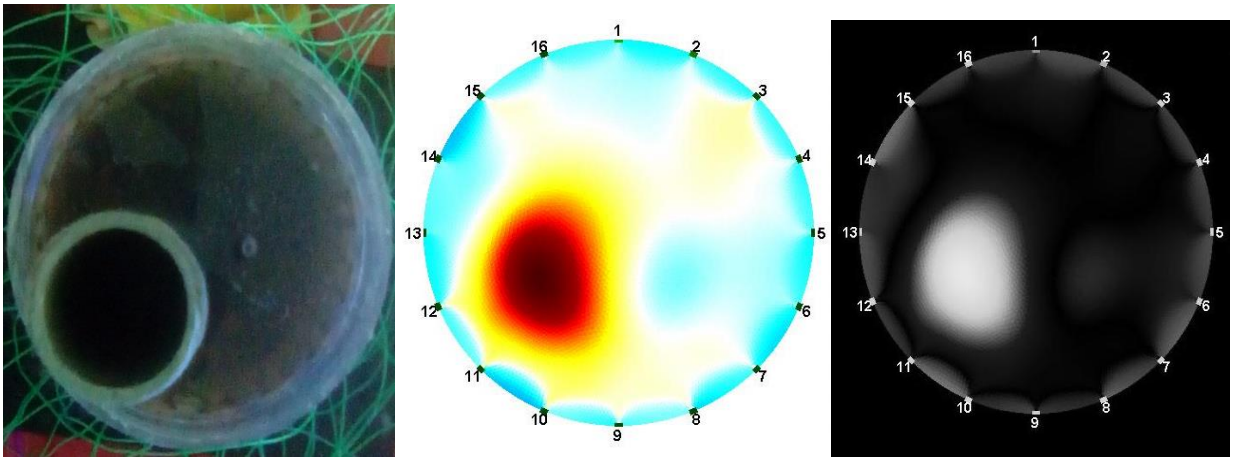

Figure 7- 9: shows the actual anomaly position at electrode 11 and the reconstructed Image and inverted grayscale image.

a) Actual Anomaly Position b) Reconstructed Image c) Inverted Gray-scale Image

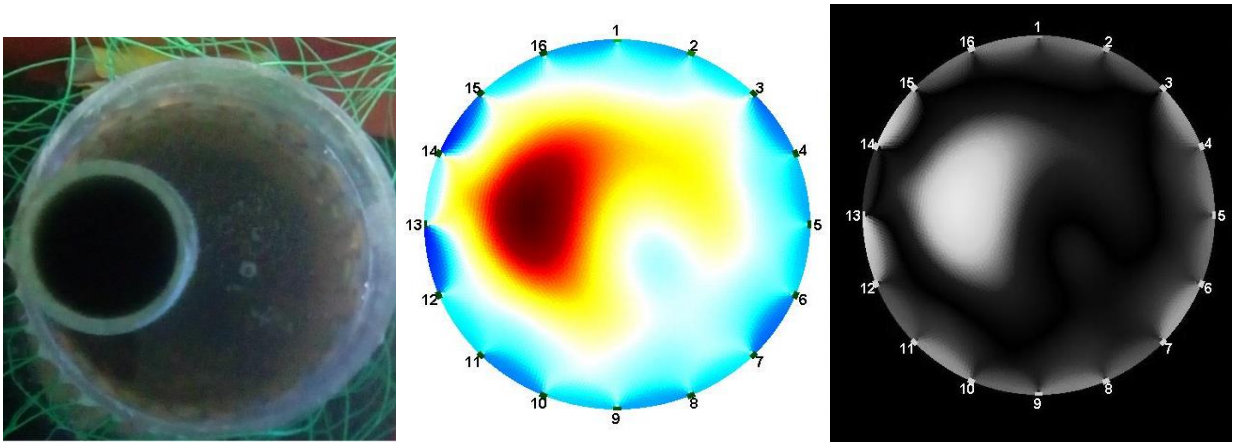

Figure 7- 10: shows the actual anomaly position at electrode 13 and the reconstructed Image and inverted grayscale image.

a) Actual Anomaly Position b) Reconstructed Image c) Inverted Gray-scale Image

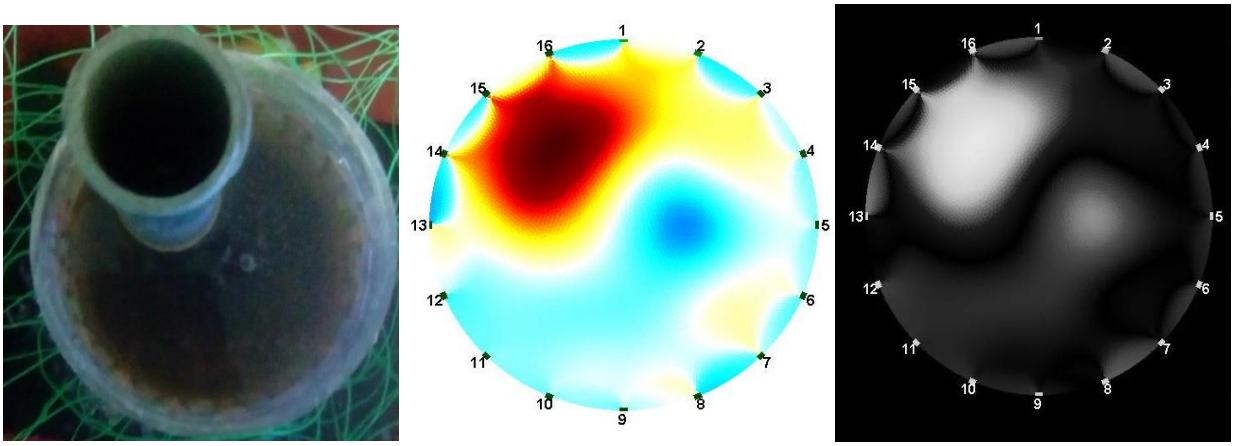

Figure 7- 11: shows the actual anomaly position at electrode 15 and the reconstructed Image and inverted grayscale image.

From the corresponding figures in Appendix C (Figure C- 9 to Figure C- 16), the position and size error and noise error ratio are computed for each reconstructed image. This is summarized in the table below:

Table 7- 3: Shows Size and Position errors in the reconstructed images for eight different positions of the anomaly, using single plane stimulation.

Error	At electrode 1	At electrode 3	At electrode 5	At electrode 7	At electrode 9	At electrode 11	At electrode 13	At electrode 15	Average Error [%]
Size Error [%]	11.37	5.41	7.79	19.13	12.96	4.61	8.00	8.59	9.73 %
Position Error [%]	23.46	10.54	1.79	12.43	17.10	10.54	3.88	13.52	11.66 %
Noise Error Ratio [%]	17.58	9.52	8.00	10.20	5.25	10.01	12.12	12.95	10.70 %

From the results in the table above, the average size error is 9.73 %, the average position error is 11.66 % and the average noise error ratio is 10.70 %. These errors show that the system operates as it was designed to operate. Furthermore, the NER shows that the recorded data was reliable, because the average noise level is well below 20 % (a design required established in Chapter 4) of the measured voltage. Also, the size and position errors are comparative to some complex systems from the reviewed papers; to be discussed later.

Additionally, to test the symmetry of the reconstructed images, the size and position errors need to be compared. The table below shows the symmetry of the system, based on the size and position errors of Table 7- 3. In Table 7- 4, the anomaly position number refers to the position of the anomaly inside the tank. Position 1 refers to electrode 1, position 2 refers to electrode 3, position 3 refers electrode 5, and so on. Each subsequent position number (n) refers to electrode number (n+i), where *i* is the index in the position sequence (i.e. i = 0, 1, 2, 3…7).

Table 7- 4: Shows the difference in the size and position errors for diametrically opposite anomaly position pairs, for the single plane stimulated system images.

Difference in position and size errors between diametrically opposite anomaly positions					
Anomaly position number	1 and 5	2 and 6	3 and 7	4 and 8	Average error [%]
Size error difference [%]	1.59	0.8	0.21	10.54	3.29
Position error difference [%]	6.36	0	2.09	1.09	2.39

Table 7- 4 shows the differences in the position and size errors for images that show anomaly positions that are diametrically opposite one another. This table aims to show if the size and position errors remained consistent when an anomaly was placed in one position, imaged, then placed in a position diametrically opposite the first position, and imaged. The table above shows that the most inconsistencies occur when an anomaly is placed at position 4 and 8. This is caused by electrode position errors at those positions in the center plane. Furthermore, the average (difference) size and position errors, 3.29 % and 2.39 %, are adequate.

7.2.2 Cross plane stimulation

This section presents the images that were reconstructed from the boundary voltage measurements, when current propagated from the top plane to the bottom plane; cross plane current stimulation pattern. Furthermore, the same test conditions, from the tests in the previous section, were kept. The results of this experiment follows.

a) Actual Anomaly Position b) Reconstructed Image c) Inverted Gray-scale Image

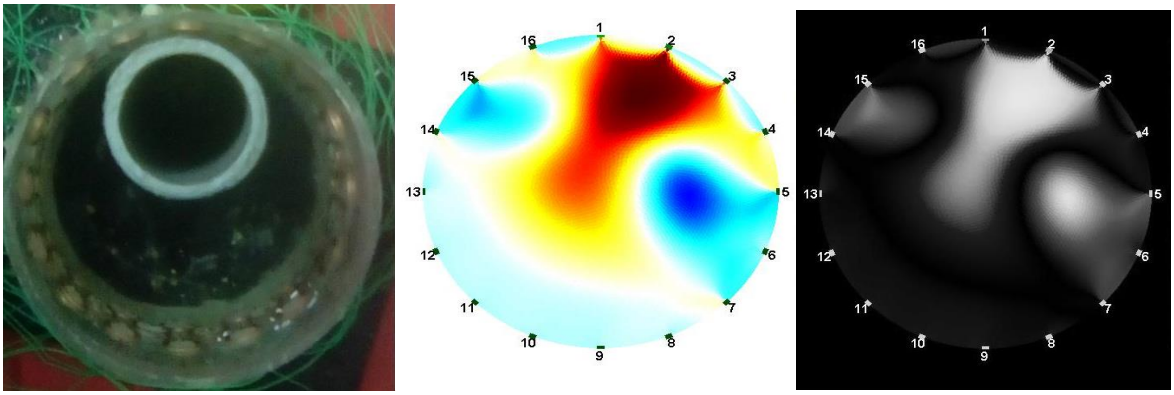

Figure 7- 12: shows the actual anomaly position at electrode 1 and the reconstructed Image and inverted grayscale image; using cross plane stimulation.

a) Actual Anomaly Position b) Reconstructed Image c) Inverted Gray-scale Image

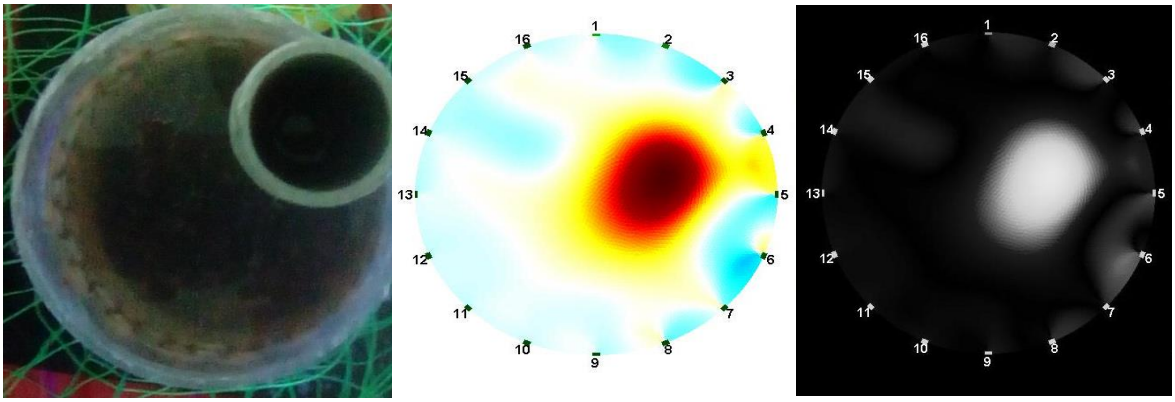

Figure 7- 13: shows the actual anomaly position at electrode 3 and the reconstructed Image and inverted grayscale image; using cross plane stimulation.

a) Actual Anomaly Position b) Reconstructed Image c) Inverted Gray-scale Image

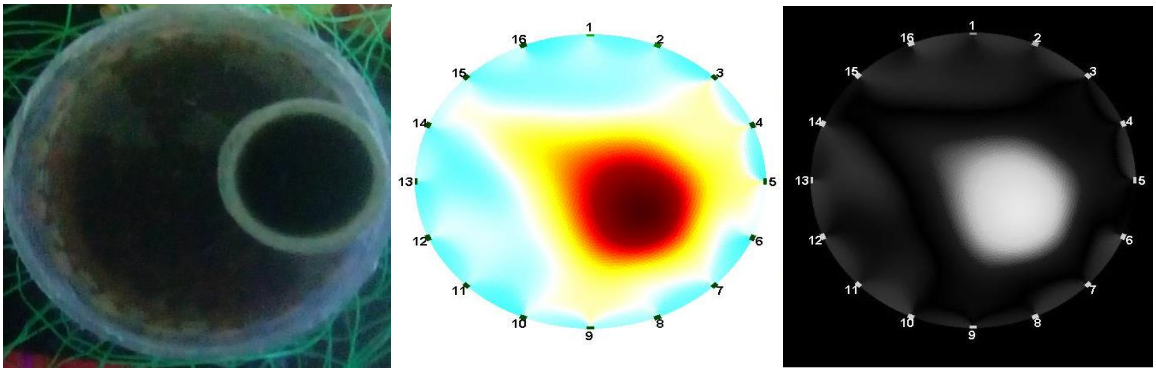

Figure 7- 14: shows the actual anomaly position at electrode 5 and the reconstructed Image and inverted grayscale image; using cross plane stimulation.

a) Actual Anomaly Position b) Reconstructed Image c) Inverted Gray-scale Image

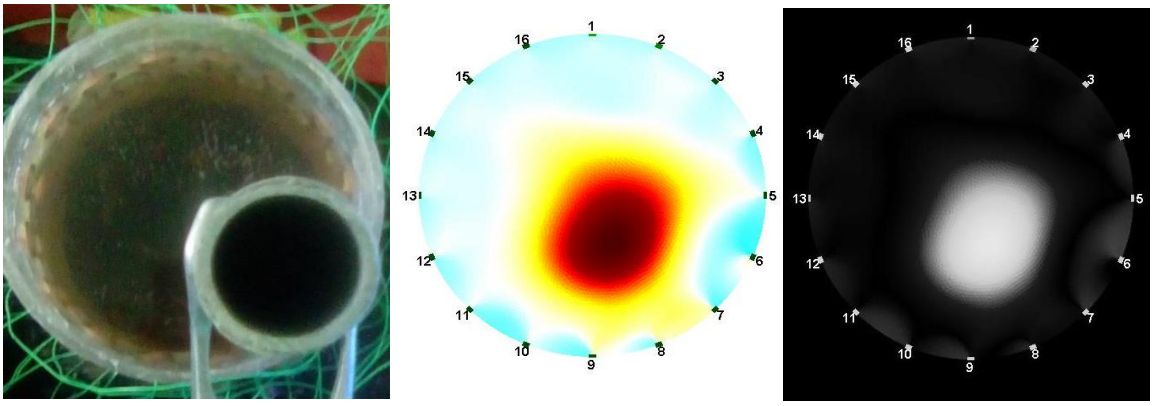

Figure 7- 15: shows the actual anomaly position at electrode 7 and the reconstructed Image and inverted grayscale image; using cross plane stimulation.

a) Actual Anomaly Position b) Reconstructed Image c) Inverted Gray-scale Image

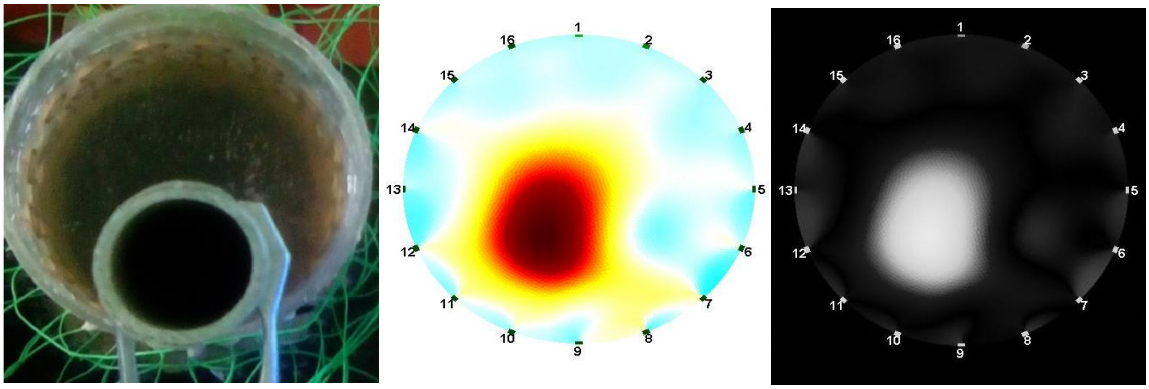

Figure 7- 16: shows the actual anomaly position at electrode 5 and the reconstructed Image and inverted grayscale image; using cross plane stimulation.

a) Actual Anomaly Position b) Reconstructed Image c) Inverted Gray-scale Image

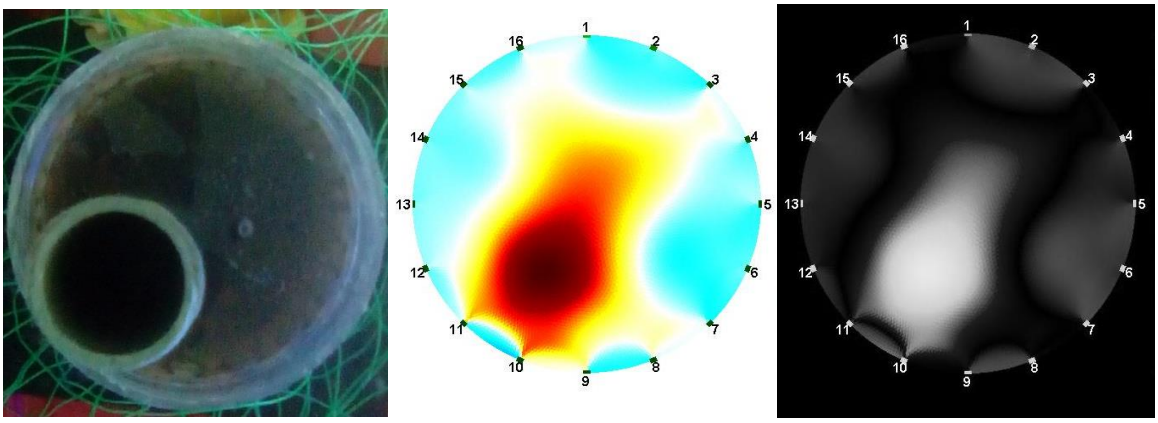

Figure 7- 17: shows the actual anomaly position at electrode 11 and the reconstructed Image and inverted grayscale image; using cross plane stimulation.

a) Actual Anomaly Position b) Reconstructed Image c) Inverted Gray-scale Image

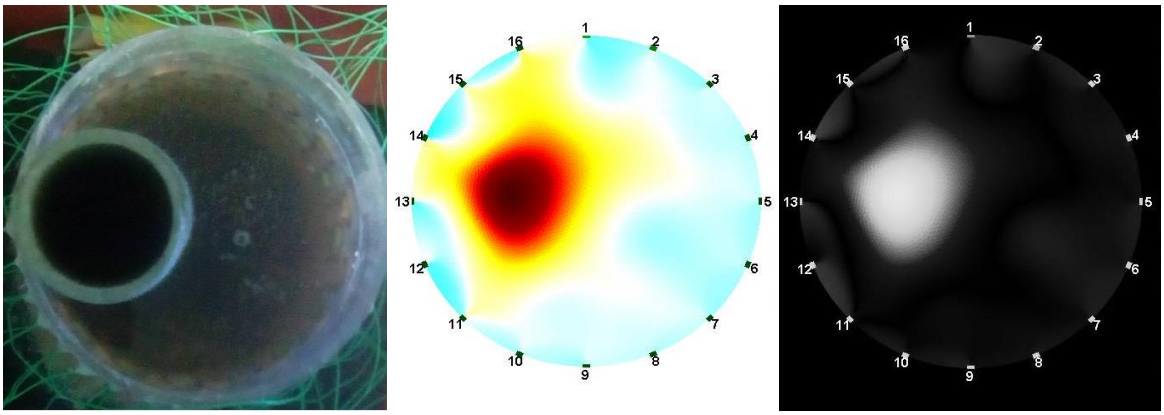

Figure 7- 18: shows the actual anomaly position at electrode 13 and the reconstructed Image and inverted grayscale image; using cross plane stimulation.

a) Actual Anomaly Position b) Reconstructed Image c) Inverted Gray-scale Image

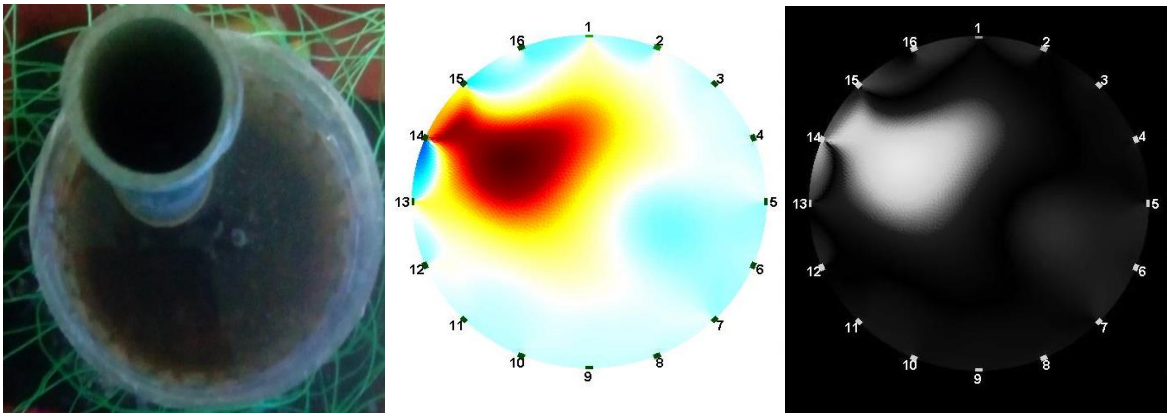

Figure 7- 19: shows the actual anomaly position at electrode 15 and the reconstructed Image and inverted grayscale image; using cross plane stimulation.

Table 7- 5: Shows Size and Position errors in the reconstructed images for eight different positions of the anomaly, using cross plane stimulation.

Error	At electrode 1	At electrode 3	At electrode 5	At electrode 7	At electrode 9	At electrode 11	At electrode 13	At electrode 15	Average Error [%]
Size Error [%]	3.42	4.22	9.19	10.98	4.25	6.33	6.18	6.63	6.40 %
Position Error [%]	1.24	2.58	3.88	7.36	9.61	7.38	9.13	8.16	6.17 %

From the results in the table (computed from the corresponding data points in the figures in Appendix C; Figure C- 17 to Figure C- 24) above, it is concluded that the cross plane data provides an improvement on the size and position accuracy of the reconstructed images, when compared to the results from the single plane stimulation protocol. This is true, because the anomalies were placed at the boundary and, as stated in Chapter 3, the cross plane injection pattern introduces a current density in the center plane that is identical to an adjacent current stimulation pattern. This means that it was expected that the reconstruction errors will be reduced when using cross-plane injections, because it produces a higher current density at the boundary; compared to the 90-degree injection pattern used in the center plane. Additionally, the noise error ratio was not computed for the cross-plane data. This is because any extra noise introduced by cross-plane current stimulation, although it is expected to be negligable, will be observed in the NER results for the DCS system.

Table 7- 6: Shows the difference in the size and position errors for diametrically opposite anomaly position pairs, for the cross plane stimulated system images.

	Difference in position and size errors between diametrically opposite anomaly positions				
Anomaly position number	1 and 5	2 and 6	3 and 7	4 and 8	Average error [%]
Size error difference [%]	0.83	2.11	3.01	4.35	2.58
Position error difference [%]	8.37	4.8	5.25	0.8	4.81

Table 7- 6 above, shows the differenced position and size errors for the different images, for cross-plane stimulation. This table aims to show if the size and position errors remained consistent when an anomaly was placed in one position, imaged, then placed in a position diametrically opposite the first position, and imaged. The table above shows that the most inconsistencies occur when an anomaly is placed at position 3 and 7. This is caused by cross

plane electrode position errors at those positions. Furthermore, the average (difference) size and position errors, 2.58 % and 4.81 %, are adequate.

7.2.3 Dual current stimulation

The weighted average of the single and cross plane stimulation data is needed to reconstruct images for the DCS system. The weights were fixed at 0, 0.25, 0.5, 0.75 and 1. These weights were chosen as follows. If one image for a given anomaly position has a much poorer image quality compared to the other (extreme case), then the first image bears no weight (i.e. multiplied by 0) and the DCS image is an exact copy of the other image. Furthermore, if one image is poorer than another, but, the average reconstruction errors are below 20 %, then that image is given a weight of 0.25 while the enhanced image is given a weight of 0.75. If both images have similar errors, then both are given a weight of 0.5. Based on the error tables from the previous two sections, the following weight table is presented.

Table 7- 7: Weight per injection protocol for different anomaly positions.

	Anomaly Positions							
Injection Protocol	Elec 1	Elec 3	Elec 5	Elec 7	Elec 9	Elec 11	Elec 13	Elec 15
Single	0.25	0.5	0.5	0.25	0.25	0.5	0.5	0.25
Cross	0.75	0.5	0.5	0.75	0.75	0.5	0.5	0.75

The results of this experiment follows this page.

a) Actual Anomaly Position b) Reconstructed Image c) Inverted Gray-scale Image

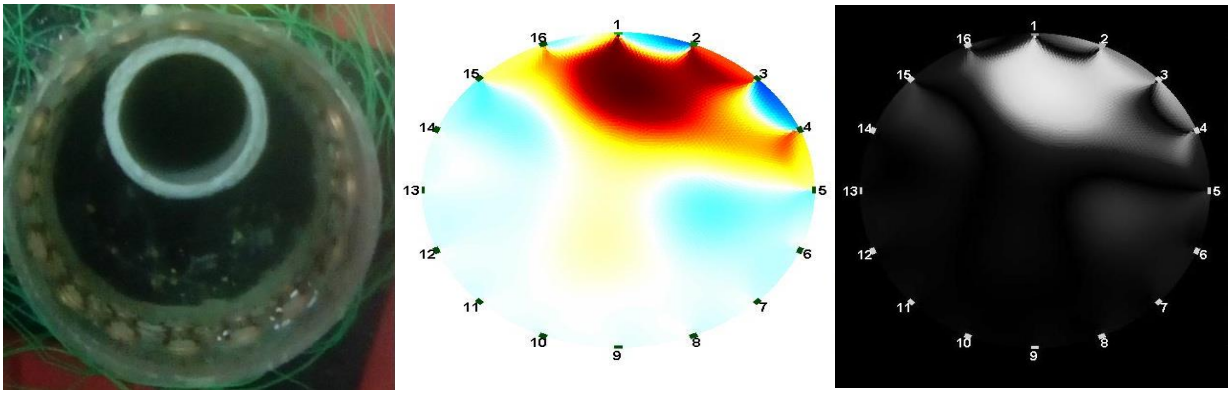

Figure 7- 20: shows the actual anomaly position at electrode 1 and the reconstructed Image and inverted grayscale image; using dual current stimulation.

a) Actual Anomaly Position b) Reconstructed Image c) Inverted Gray-scale Image

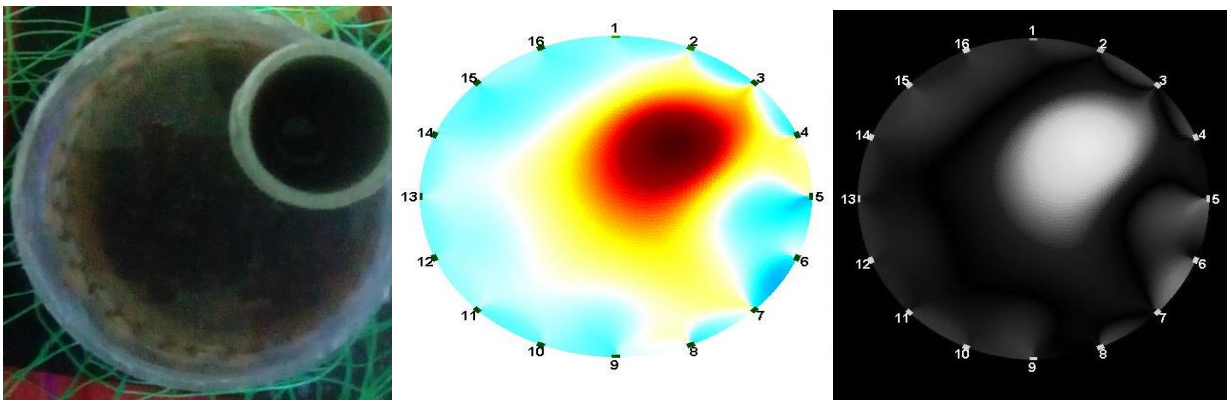

Figure 7- 21: shows the actual anomaly position at electrode 3 and the reconstructed Image and inverted grayscale image; using dual current stimulation.

a) Actual Anomaly Position b) Reconstructed Image c) Inverted Gray-scale Image

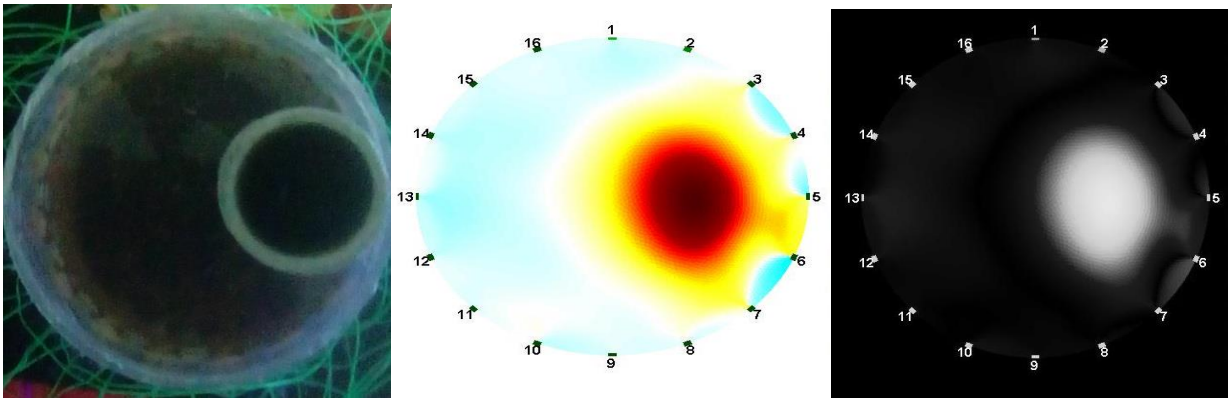

Figure 7- 22: shows the actual anomaly position at electrode 5 and the reconstructed Image and inverted grayscale image; using dual current stimulation.

a) Actual Anomaly Position b) Reconstructed Image c) Inverted Gray-scale Image

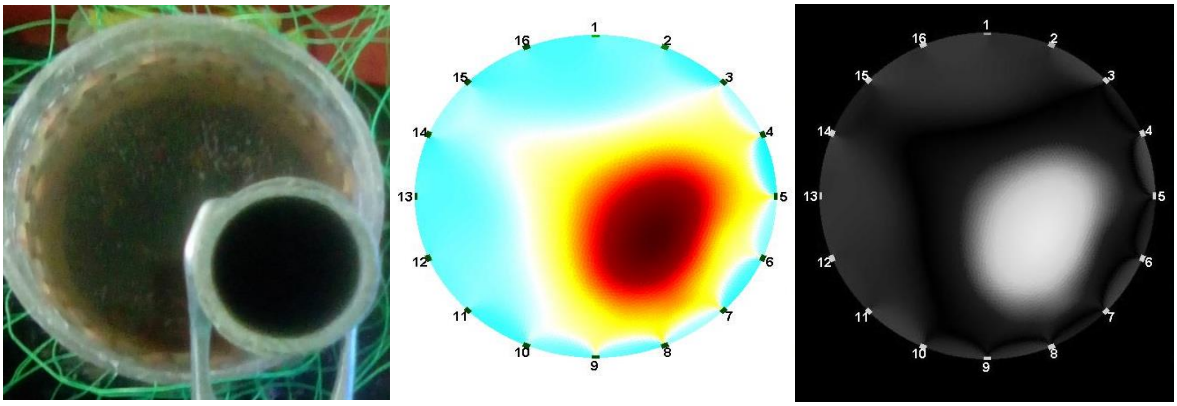

Figure 7- 23: shows the actual anomaly position at electrode 7 and the reconstructed Image and inverted grayscale image; using dual current stimulation.

a) Actual Anomaly Position b) Reconstructed Image c) Inverted Gray-scale Image

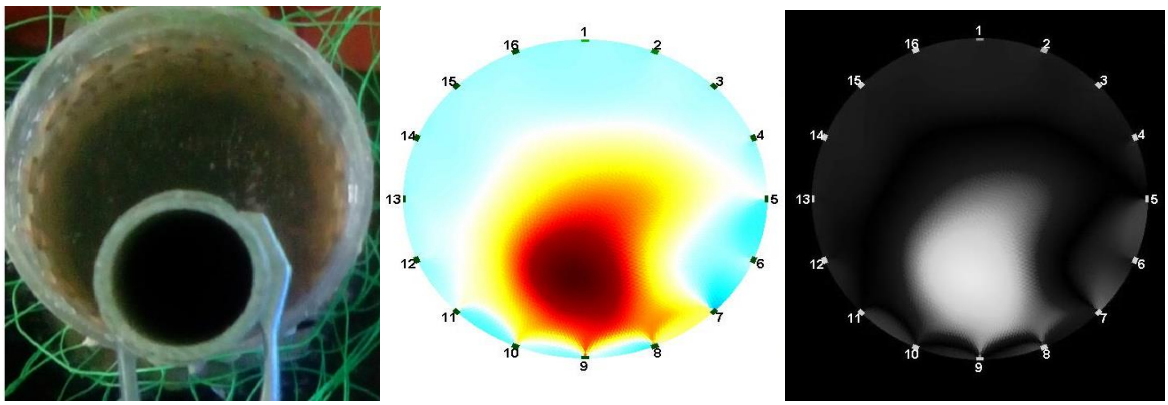

Figure 7- 24: shows the actual anomaly position at electrode 9 and the reconstructed Image and inverted grayscale image; using dual current stimulation.

a) Actual Anomaly Position b) Reconstructed Image c) Inverted Gray-scale Image

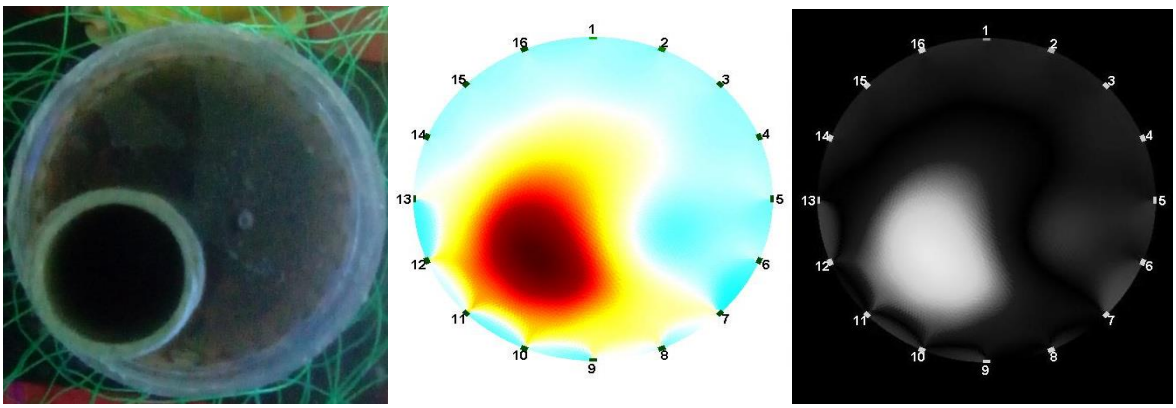

Figure 7- 25: shows the actual anomaly position at electrode 11 and the reconstructed Image and inverted grayscale image; using dual current stimulation.

a) Actual Anomaly Position b) Reconstructed Image c) Inverted Gray-scale Image

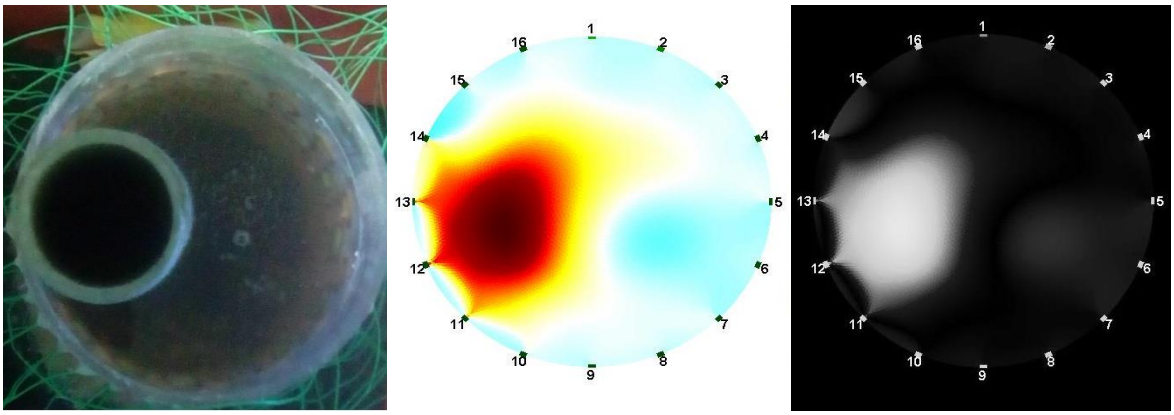

Figure 7- 26: shows the actual anomaly position at electrode 13 and the reconstructed Image and inverted grayscale image; using dual current stimulation.

a) Actual Anomaly Position b) Reconstructed Image c) Inverted Gray-scale Image

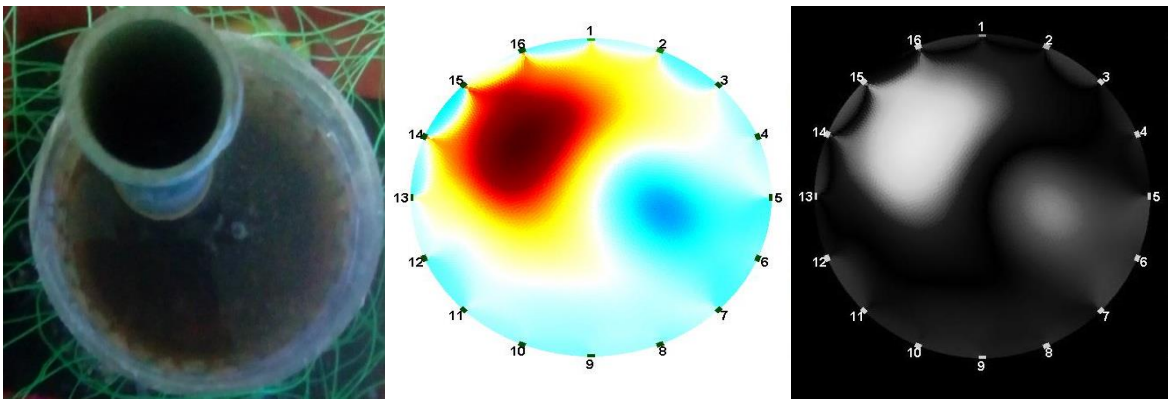

Figure 7- 27: shows the actual anomaly position at electrode 15 and the reconstructed Image and inverted grayscale image; using dual current stimulation.

The position and size errors for the above reconstructed images, computed from Appendix C Figure C- 25 to Figure C- 32, are tabulated below.

Table 7- 8: Size and position errors in the reconstructed images, which used dual current stimulation, for eight different anomaly positions.

Error	At electrode 1	At electrode 3	At electrode 5	At electrode 7	At electrode 9	At electrode 11	At electrode 13	At electrode 15	Average Error [%]
Size Error [%]	1.35	4.22	2.16	2.46	3.95	5.59	1.41	1.46	2.82%
Position Error [%]	0.25	0.89	7.53	5.37	2.76	10.77	4.81	15.08	5.93%
Noise Error Ratio [%]	17.22	10.00	7.43	9.20	5.69	9.61	14.08	12.72	10.74 %

The table above shows that, when compared to the error tables for single and cross plane stimulation, the size and positions errors have significantly been reduced; which shows that the DCS system has a more uniform current distribution compared to either single plane or cross plane injection patterns; individually. In addition, a cucumber and an industrial PVC anomaly (of 30 % the diameter of the test tank) was imaged, as was done with the plastic tube in eight equidistant positions relative to the center of the tank, and the results were identical to those in Table 7- 8. Furthermore, the noise error ratio is identical to that achieved using single plane stimulation, because there is no difference in the hardware setup for either injection pattern; only a switch function in the code is implemented to multiplex from the center plane to the cross plane current electrodes. A summary of the symmetrical characteristics of the DCS EIT system is tabulated below.

Table 7- 9: Shows the difference in the size and position errors for diametrically opposite anomaly position pairs, for the dual plane stimulation system images.

	Difference in position and size errors between diametrically opposite anomaly positions				
Anomaly position number	1 and 5	2 and 6	3 and 7	4 and 8	Average error [%]
Size error difference [%]	2.6	1.37	0.75	1	1.43
Position error difference [%]	2.51	9.88	2.72	9.71	6.21

Table 7- 9 above, shows the differenced position and size errors for the different images, for dual current stimulation. This table aims to show if the size and position errors remained consistent when an anomaly was placed in one position, imaged, then placed in a position diametrically opposite the first position, and imaged. The table above shows that the most inconsistencies occur when an anomaly is placed at position 2 and 6. This is caused by the electrode position errors in all three electrode planes. Furthermore, the average (difference) size and position errors, 1.43 % and 6.21 %, are adequate. Moreover, to draw conclusive statements on the image quality of the two systems, the distinguishability needs to be analyzed.

7.2.4 Distinguishability

To analyze the distinguishability between the single plane and DCS systems, the following images are inspected.

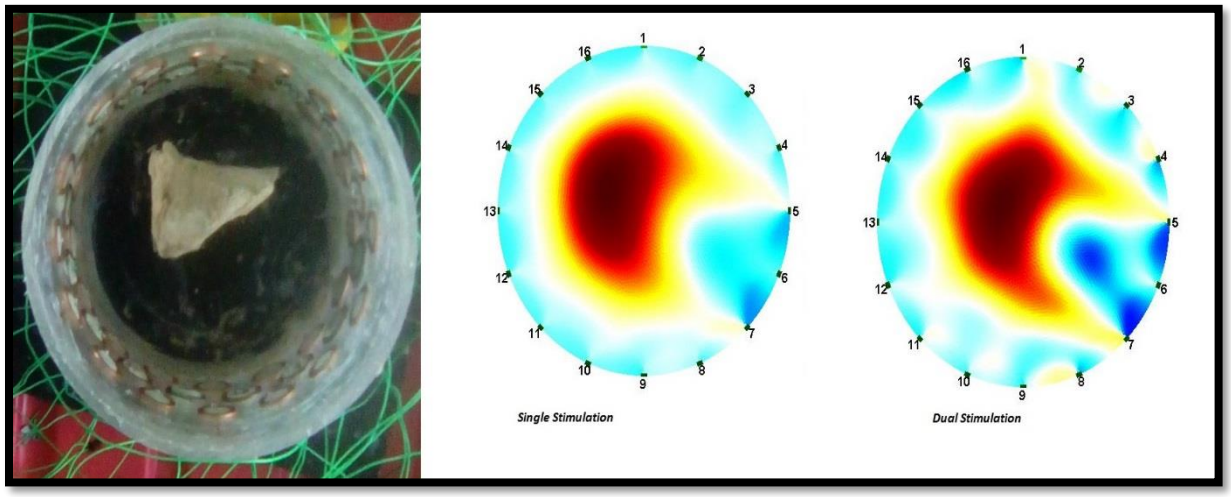

Figure 7- 28: Shows the reconstructed images for the single plane and DCS systems, when a triangular cross-section anomaly, made of clay, is inserted into the phantom tank. It clearly shows that the DCS system was able to detect sharper edges and, thus, producing a more reliable reconstructed image.

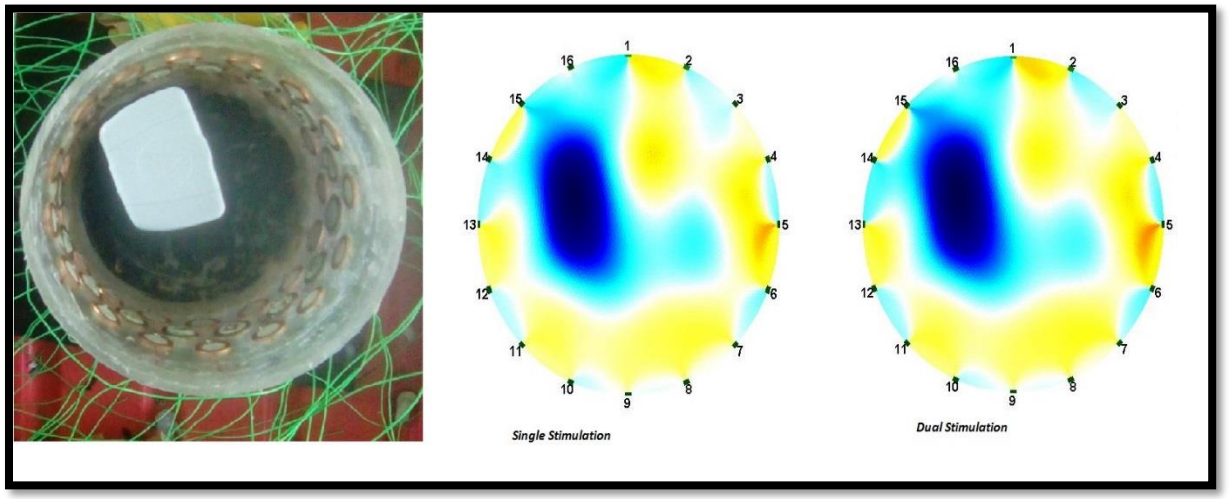

Figure 7- 29: Shows the reconstructed images for the single and DCS systems, when an irregular shaped cross-section anomaly, made of high density PVC, is inserted into the phantom tank. It clearly shows that the DCS system was able to detect sharper edges and less blurring and, thus, producing a more reliable reconstructed image.

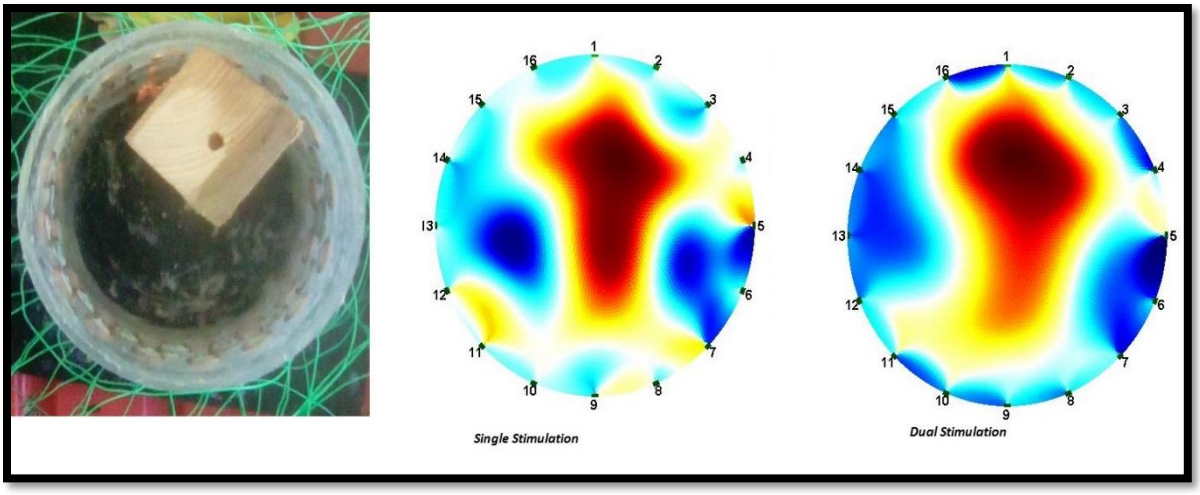

Figure 7- 30: Shows the reconstructed images for the single and DCS systems, when a rectangular cross-section anomaly, made of wood, is inserted into the phantom tank. It clearly shows that the DCS system was able to detect fewer false-positive causing artefacts and more defined edges that closely resemble a rectangle and, thus, producing a more reliable reconstructed image.

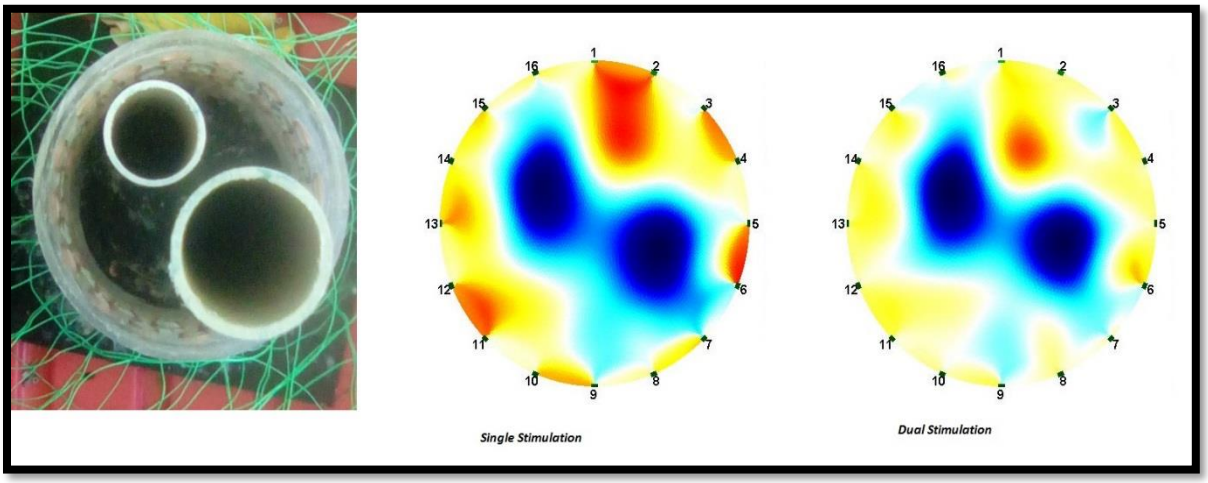

Figure 7- 31: Shows the reconstructed images for the single and DCS systems, when two circular cross-section anomalies, made of hollow industrial standard PVC, is inserted into the phantom tank. It clearly shows that the DCS system was able to detect both anomalies while preserving the size difference between the two objects and, thus, producing a more reliable reconstructed image.

From these figures, it is clear that the DCS system has a superior ability to detect different anomaly shapes and to distinguish between several anomalies that are placed inside the test tank. The images, reconstructed from the DCS EIT system, were sharper and preserved shapes and distances better between anomalies, when compared to the single plane stimulated images.

Size Error Comparisons:

This subsection provides size error comparisons between the results from the DCS system and the reported results from a few papers that used single plane current stimulation. In this paper, the size error was computed by analyzing the pixel intensity plots of the reconstructed images. These plots show the number of pixels which have detected an anomaly. The range of pixels which have detected an anomaly is divided by the total number of pixels to estimate the percentage of the size of the anomaly to the size of the test tank. The absolute difference between this percentage and the ratio between the actual size of the anomaly and the test tank is computed to give the size error. The results of the DCS EIT system is comparable to the results stated by Tšoeu, M in [6], which reported a size error of 6.2 %, for a 2D Code Division Multiplexed System. Other reviewed papers have estimated average size errors of:

- 14 % obtained by Tong In Oh *et al* in [53].
- 20 % obtained by A McEwan *et al* in [44].
- 35 % obtained by M. Nahvi *et al* in [54].
- 40 % obtained by F. Satter in [48].
- 30 % obtained by D. S. Holder in [55].

Furthermore, the author did not find any reported image errors for 2.5D EIT systems. Therefore, the DCS images cannot be compared to a 2.5D EIT system, without any reported image quality.

Position Error Comparisons:

This subsection provides position error comparisons between the results from the DCS system and the reported results from a few papers that used single plane current stimulation. The position error was computed using the pixel intensity plots of the reconstructed images. By plotting the pixel intensity plot along a vertical or horizontal line within the vicinity where the anomaly was placed (i.e. plotted along the x-axis or y-axis if the anomaly was placed on the x-axis or y-axis, or plotted along a line in the quadrant in which the anomaly was placed), one can extract the radial position of the centroid of an anomaly in the reconstructed image relative to the center of the test tank. The average position error of the results from this paper is comparable to Tšoeu, M in [6], which reported an average position error of 3.5 %.

Other reviewed papers have an estimated position error of:

- 12 % obtained by A. McEwan in [44].
- 25 % obtained by R. Yerworth in [56].
- 25 % obtained by D. S. Holder *et al* in [55].

7.3 Summary

From the results presented in this chapter, it is concluded that a 24-bit resolution EIT system did not provide any significant improvement in the measurement accuracy, when compared to a 16-bit resolution system (based on the bit resolution alone). However, the 24-bit ADC technology was able to attenuate noise because it had a built-in filter, while the 16-bit ADC did not attenuate noise. This resulted in the 24-bit ADC producing improved image detail compared to the 16-bit ADC.

Furthermore, when comparing the single plane stimulation to the DCS system, the DCS system produced images with a higher spatial resolution and an enhanced image quality. It was better able to define the edges of several anomalies and their shapes, irrespective of the position of the anomaly inside the test tank. Thus, it is concluded that the DCS system does in fact enhance image reconstructions.

In addition, it was shown that the single plane and cross plane systems were able to directly compete with the results of more expensive and complicated systems, from the reviewed papers, that incorporated more complex algorithms and injection protocols. It is therefore hypothesised (based on the results from this report) that the DCS system can reliably outperform some of the more advanced systems, given more precise instruments.

8 Conclusions, recommendations and future work

This chapter draws conclusions based on the research hypothesis, questions, simulation results and experimental results. Subsequently, recommendations are made to improve the EIT system and future works are discussed.

8.1 Hypothesis confirmation

The research hypothesis, which stated that a DCS protocol can be used to reconstruct images that have a higher image quality, compared to those produced from a single plane current stimulation protocol EIT system (which uses time difference imaging), was confirmed. Two different current patterns were chosen to provide a more uniform current distribution in the medium, compared to the single plane system. Both systems used stainless steel compound electrodes with optimized size and positions. Furthermore, the DCS EIT system produced images with a spatial resolution twice that of the single plane EIT reproduced images, as computed in chapter 3. Additionally, the reproduced images, from the DCS EIT system, have a size error of 2.82 % and position error of 5.93 %, which is more than half that from the single plane EIT images (SE = 9.37 % and PE = 11.66 %), and is comparable to the stated results of a 2-dimensional Code Division Multiplexed EITS system, proposed in [6]. The achievable advantages of DCS EIT systems over single plane stimulated, time difference, EIT systems is an improved image quality. However, the DCS EIT system requires three times the number of electrodes and has a lower temporal resolution. This makes it challenging, when scaling the system to 3-dimensional applications. In contrast, a 3-dimensional EIT system that incorporates the DCS protocol on the centre plane is hypothesised to provide promising results.

8.2 Prototype DCS EIT system

The prototype DCS EIT system was successfully designed and tested. The system uses 48 compound electrodes divided over three planes, to establish two independent current stimulation patterns, which improves the current distribution in a medium. The prototype system has adequate noise levels which are reduced, using voltage thresholding and a notch filter on-board

a 24-bit ADC. The aggregate noise error ratio is 10.74 %, which is much less than the design constraint of 20 %. The system measurement accuracy is 0.045 % and the system showed no low frequency drift. Moreover, the DCS system is able to distinguish between different anomaly shapes and sizes, and between several anomalies. Furthermore, the system produced repeatable results and significantly reduced ringing. However, the system has symmetry issues, due to electrode position errors, and a low temporal resolution of 1 frame/minute.

8.3 Recommendations

Based on the limitations of the designed prototype system, the following recommendations are made:

- Use parallel voltage measurement channels and faster sampling rates to improve the temporal resolution.
- Configure the device to incorporate frequency difference or code division multiplexing over a wide frequency band, to account for fast changing, frequency dependent specimens.
- Test the device on real biomedical applications after including device isolation circuit breakers.
- Use shielded cables to reduce measurement noise.
- Use band-pass filters instead of notch filters, to capture signals in a selected frequency range.
- Design a more accurate and stable VCCS.
- Use a digital synchronous voltmeter.

8.4 Future works

From the success of this work, future research that is aimed at improving the system is outlined below.

- A fully parallel, real-time image reconstruction using the DCS protocol will be designed, to improve the temporal resolution.
- Time and frequency difference and code division multiplexing will be incorporated into the system design, to produce a system that accounts for all types of biological specimen.

- To increase the image processing speed, custom image reconstruction software will be developed.
- A three-dimensional system that only uses the DCS protocol for centre plane measurement will be considered.

References

[1] D. S. Holder, Electrical Impedance Tomography: Methods, History and Applications, London: Institute of Physics Publishing, 2005.

[2] K. Arti, "Electrical Impedance Tomography," 27 August 2017. [Online]. Available: https://pdfs.semanticscholar.org/7bfc/03763a57e435c656f0cb8926653060354f56.pdf?_ga=2.250040833.623296811.1529397257-1323705390.1529397257. [Accessed 2 April 2016].

[3] C. Gomez-Laberge and A. Adler, "Direct EIT Jacobian calculations for conductivity change and electrode movement," *Physiological Measurement,* vol. 29, no. 6, 2008.

[4] L. Brancik, "Comparative Study of Jacobian Calculation Techniques in Electrical Impedance Tomography," cpee, Purkynova, 2004.

[5] B. Gong, B. Schullcke, S. Krueger-Ziolek and K. Moeller, "EIT Imaging Regularization Based on Spectral Graph Wavelets," *Springer International Publishing Switzerland,* vol. 57, no. 10, pp. 1280-1281, 2016.

[6] M. S. Tsoeu, "Electrical Impedance Tomography/Spectroscopy (EITS)," UCT, Cape Town, 2016.

[7] A. Wilkinson, E. Randall, J. Cilliers, D. Durrett, T. Naidoo and T. Lonh, "A 1000-measurement frame/second ERT data capture system with real-time visualization," *IEEE Sensors Journal,* vol. 5, no. 2, pp. 300-307, 2005.

[8] H. Koo, K. Lee, T. Oh, S. Kim, J. Lee, S. Kim, J. Seo and E. Woo, "Validation of a multi-frequency electrical; impedance tomography (mfEIT) system KHU Mark1: impedance spectroscopy and time-difference imaging," *Physiological Measurement,* no. 29, pp. 295-307, 2008.

[9] M. Goharian, M. J. Bruwer, A. Jegatheesan, G. R. Moran and J. F. MacGregor, "A noval approach for EIT regularization via spatial and spectral principle component analysis," *Physiological Measurement,* vol. 28, no. 9, pp. 1001-1016, 2007.

[10] M. Vauhkonen, D. Vadasz, P. A. Karjalainen, E. Somersalo and J. P. Kaipio, "Tikhonov regularization and prior information in electrical impedance tomography," *IEEE Transaction on Medical Imaging,* vol. 17, no. 2, pp. 285-293, 1998.

[11] N. Bahrani and A. Adler, *2.5D Finite Element Method for Electrical Impedance Tomography Considering the Complete Electrode Model,* Canada: Carleton University , 2012.

[12] R. K. Y. Chin and T. A. York, "Improving spatial resolution for EIT reconstructed images through measurement strategies," University of Manchester, Manchester, 2013.

[13] FDA, "What is Computed Tomography," U.S. FOOD & DRUG Administration, 2014. [Online]. Available: www.fda.gov/radiation-emittingproducts/radiationemittingproductsandprocedures/medicalimaging/medicalx-rays/ucm115318.htm. [Accessed 2 5 2017].

[14] E. Zimmermann, J. A. Huisman, W. Glaas and S. van Waasen, "Fast EIT data acquisition for geophysical applications," ResearchGate, Julich, 2013.

[15] C. Wei and W. Chang, "Electrical Impedance Tomography (E.I.T.) Measurement System," University of Cape Town, Cape Town, 2003.

[16] D. Fleisch, A Student's Guide to Maxwell's Equations, Cambridge: Cambridge University Press, 2008.

[17] B. M. Graham, "Enhancements in Electrical Impedance Tomography (EIT) Image Reconstruction for 3D Lung Imaging," University of Ottawa, Canada, 2007.

[18] W. R. B. Lionheart, "EIT reconstruction algorithms: pitfalls, challenges and recent developments," *Physiological Measurement,* vol. 25, no. 1, pp. 125-142, 2004.

[19] A. Mejia-Aguilar and R. Pallas-Areny, "Electrical Impedance Measurement Using Voltage/Cureent Pulse Excitation," XIX IMEKO World Congress, Lisbon, 2009.

[20] J.-F. Abascal, S. Arridge, R. Bayfor and D. Holder, "Comparison of methods for optimal choice of the regularization parameter for linear electrical impedance tomography of brain function," *Physiological Measurment,* vol. 29, no. 11, pp. 1319-1334, 2008.

[21] S. I. Kabanikhin, "Definitions and examples of inverse and ill-posed problems," de Gruyter, Sobolov, 2008.

[22] G. Boverman, B. S. Kim, D. Isaacson and J. C. Newell, "The Complete Electrode Model for Imaging and Electrode Contact Compensation in Electrical Impedance Tomography," in *29th Annual International Conference of the IEEE EMBS*, Lyon, 2007.

[23] Z. Cendes, D. Shenton and H. Shahnasser, "Adaptive finite element mesh generation using the delaunay algorithm," Carnegie Mellon University Research Showcase @ CMU, Pittsburgh, 1982.

[24] E. J. Woo, P. Hua, J. G. Webster and W. J. Tompkins, "Finite-element method in electrical impedance tomography," Medical physics and imaging, Korea, 1994.

[25] S. Pursiainen and H. Hakula, "A High-order Finite Element Method for Electrical Impedance Tomography," *PIERS 2006,* vol. 2, no. 3, pp. 260-264, 2006.

[26] D. C. Barber, B. H. Brown and N. J. Avis, "Image Reconstruction in Electrical Impedance Tomography Using Filtered Back-Projection," University of Sheffield, Sheffield, 2008.

[27] G. Teague, "Mass Flow Measurement of Multi-Phase Mistures by means of Tomographic Techniques," University of Cape Town, Cape Town, 2002.

[28] J. P. Morucci, P. M. Marsili, M. Granie, Y. Shi, M. Lei and W. W. Dai, "A direct sensitivity matrix approach for fast reconstruction in electrical impedance tomography," Physiological Measurement, France, 1994.

[29] Y. Pei, Y. Xu and F. Dong, "A modified L-curve method for choosing regularization paramter in electrical impedance tomography," IEEE, Tianjin, 2015.

[30] M. Jansen, "Generalized Cross Validation in variable selection with and without shrinkage," Universite Libre de Bruxelles, Belgium, 2015.

[31] Anritsu, Noise Figure Measurement Methods, Japan: Anritsu, 2016.

[32] D. Garg and V. Goel, "Design and development of electrical impedance tomography (EIT) based system," *International Jouranl of Computer Applications,* vol. 74, no. 7, pp. 33-36, 2013.

[33] M. Osypka and E. Gersing, "Tissue impedance spectra and the appropriate frequencies for EIT," Physiological Measurement, Gottingen, 1995.

[34] N. Li, H. Xu, Z. Zhou, J. Xin, Z. Sun and X. Xu, "Reconfigurable Bioimpedance Emulation System for electrical impedance tomography system validation," *IEEE TRANSACTIONS ON BIOMEDICAL CIRCUITS AND SYSTEMS,* vol. 7, no. 4, pp. 460-468, 2013.

[35] A. Hartinger, H. Gagnon and R. Guardo, "A method for modelling and optimizing an electrical impedance tomography system," *Physiological Measurement,* vol. 27, no. 5, pp. S52-S64, 2006.

[36] T. Bera and J. Nagaraju, "A multifrequency electrical impedance tomography (EIT) system for biomedical imaging," in *2010 International Conference on Systems in Medicine and Biology (ICSMB)*, Bangalore, 2010.

[37] AGH, *Copper as electrical conductive material with above-standard performacne properties,* European Copper Institute, 2017.

[38] E. T. McAdams, P. Henry, J. M. Anderson and J. Jossinet, "Optimal electrolytic chloriding of silver ink electrodes for use in electrical impedance tomography," *Clinical Physics and Physiological Measurement,* vol. 13, no. Suppl A, pp. 19-23, 1992.

[39] SGL Group, *Carbon Electrodes - performance products for non-ferrous arc furnace applications,* Meitingen: SGL Group, 2009.

[40] H. Sudhakaran, "Application of electrical resistance tomography in evaluating the influence of nozzle design on the gas hold-up in boiling bubble column reactors," UCT, Cape Town, 2012.

[41] W. Yan, S. Hong, Z. Shu and R. Chaoshi, "Influences of Compound Electrode Parameter on Measurement Sensitivity and Reconstruction Quality in Electrical Impedance Tomography," in *IFMBE*, Tianjin, 2009.

[42] A. Adler, J. H. Arnold, R. Bayfor, A. Borsie, B. Brown, P. Dixon, T. J. C. Faes, I. Frerishs, H. Gagnon, Y. Garber, B. Grychtol, G. Hahn, W. R. B. Lionheart, A. Malik, R. P. Patterson, J. Stocks, A. Tizzardr, N. Weiler and G. K. Wolf, "GREIT: a unified approach to 2D linear EIT reconstruction of lung images," *Physiological Measurement,* vol. 30, no. 6, pp. S35-S55, 2009.

[43] M. Yasin, S. Bohm, P. O' Gaggero and A. Adler, "Evaluation of EIT system performance," *Physiological Measurement,* vol. 32, no. 7, pp. 851-865, 2011.

[44] A. McEwan, A. Romsauerova, R. Yerworth, L. Horesh and R. H. H. Bayfor, "Design and Calibration of a compact multi-frequency EIT system for acute stroke imaging," *Physiological Measurement,* vol. 27, no. 5, pp. 199-210, 2006.

[45] J. Irish, *Lecture on Instrumentation Specifications,* WHOI, 2005.

[46] N. Bahrani and A. Adler, "2.5D FEM for EIT considering the Complete Electrode Model," in *25th IEEE Canadian Conference*, Ottawa, 2012.

[47] A. Boyle and A. Adler, "The impact of electrode area, contact impedance and boundary shape on EIT images," *Physiological Measurement,* vol. 32, no. 7, pp. 745-754, 2011.

[48] F. A. Sattar, "Rot Detection in Wooden Poles using Electrical Impedance Tomography," UCT, Cape Town, 2005.

[49] J. Avery, T. Dowrick, M. Faulkner, N. Goren and D. Holder, "A Versatile and Resproducible Mutli-Frequency Electrical Impedance Tomography System," *Sensors (Basel),* vol. 17, no. 2, pp. 1-20, 31 January 2017.

[50] A. Adler, "EIDORS: Electrical Impedance Tomography and Diffuse Optical Tomography Reconstruction Software," SourceForge, 28 February 2017. [Online]. Available: eidors3d.sourceforge.net/tutorial/tutorial.shtml. [Accessed 5 April 2017].

[51] S. Russo, S. Neft-Meziani, N. Carbonaro and A. Tognetti, "Development of a high-speed current injection and voltage measurement system for electrical impedance tomography-based stretchable sensors," *Technologies,* vol. 5, no. 3, 2017.

[52] H. Wrigge, J. Zinserling, T. Muders, D. Varelmann, U. Gunther, C. von der Groeben, A. Magnusson, G. Hedenstierna and C. Putensen, "Electrical impedance tomography compared with thoracic computed tomography during a slow inflation maneuver in experimental models of lung injury," *Crit Care Med,* vol. 36, no. 3, pp. 903-909, 2008.

[53] B. Harrach, J. K. Seo and E. J. Woo, "Factorization Method and its Physical Justification in Frequency_difference EIT," *IEEE Transactions on Medical Imaging,* vol. 11, no. 29, pp. 1918-1926, 2010.

[54] M. Nahvi and B. S. Hoyle, "Wideband electrical impedance tomography," *Measurement Science and Technology,* vol. 19, no. 9, pp. 94-110, 2008.

[55] T. I. Oh, E. J. Woo and D. S. Holder, "Multi-frequency EIT system with radially symmetric architecture: KHU Mark 1," *Physiological Measurement,* no. 28, pp. 183-196, 2007.

[56] R. J. Yerworth, R. H. Bayford, B. Brown, P. Milnes, M. Conway and D. S. Holder, "Electrical Impedance Tomography Spectroscopy (EITS) for human head imaging," *Physiological Measurement,* vol. 24, no. 2, p. 477, 2003.

[57] Physiological Measurement, "Electrical Impedance Tomography," 7 January 2015. [Online]. Available: www.eit.org.uk. [Accessed 15 March 2016].

[58] M. Neumayer, M. Flatscher and T. Bretterklieber, "What is Electrical Capacitance Tomography (ECT)," Institute of Electrical Measurement and Measurement Signal Processing, [Online]. Available: www.tugraz.at/en/institutes/emt/forschung/instrumentation-measurement/electrical-capacitnace-tomography/. [Accessed 6 March 2016].

[59] the American Physiological Society, "Detection of local lung air content by electrical impedance tomography compared with electron beam CT," *Journal of Applied Physiology,* vol. 93, no. 2, pp. 660-666, 2002.

[60] J. H. P. H. G. W. G. H. T. D. M. Q. G. H. Inéz Frerichs, "Detection of local lung air content by electrical impedance tomography compared with electron beam CT," *Journal of Applied Physiology,* vol. 93, no. 2, pp. 660-666, 2002.

[61] N. Polydorides and H. McCann, "Electrode configurations for improved spatial resolution in electrical impedance tomography," *Measurement Science and Technology,* vol. 13, no. 12, p. 1862, 2002.

Appendix A: Hardware schematics and simulations

This appendix contains all system schematics used and simulations conducted when designing the EIT system.

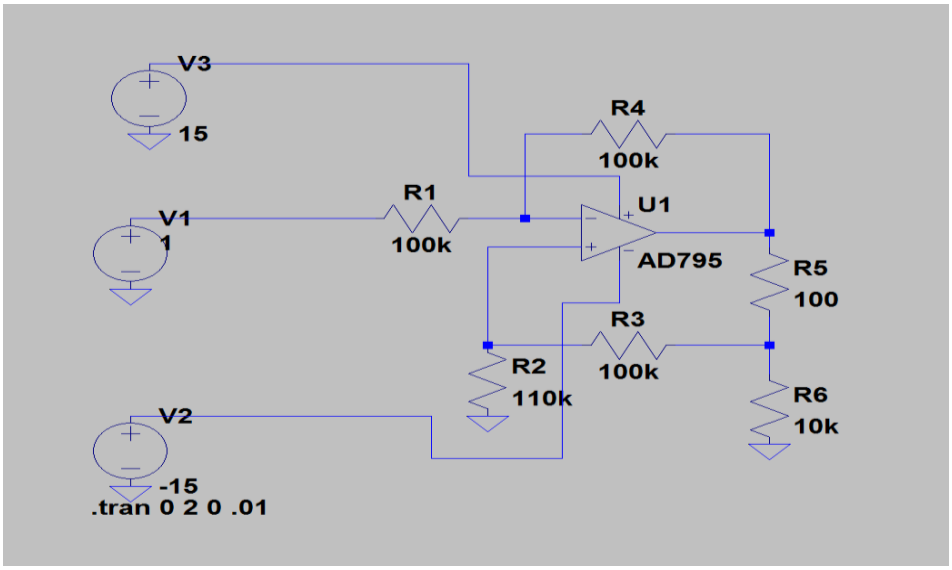

Figure A- 1: Schematic diagram of a modified Howland voltage controlled constant current source. The image shows the resistor values needed to provide the appropriate current to voltage ratio gain and the resistor R6 is used to represent the test tank.

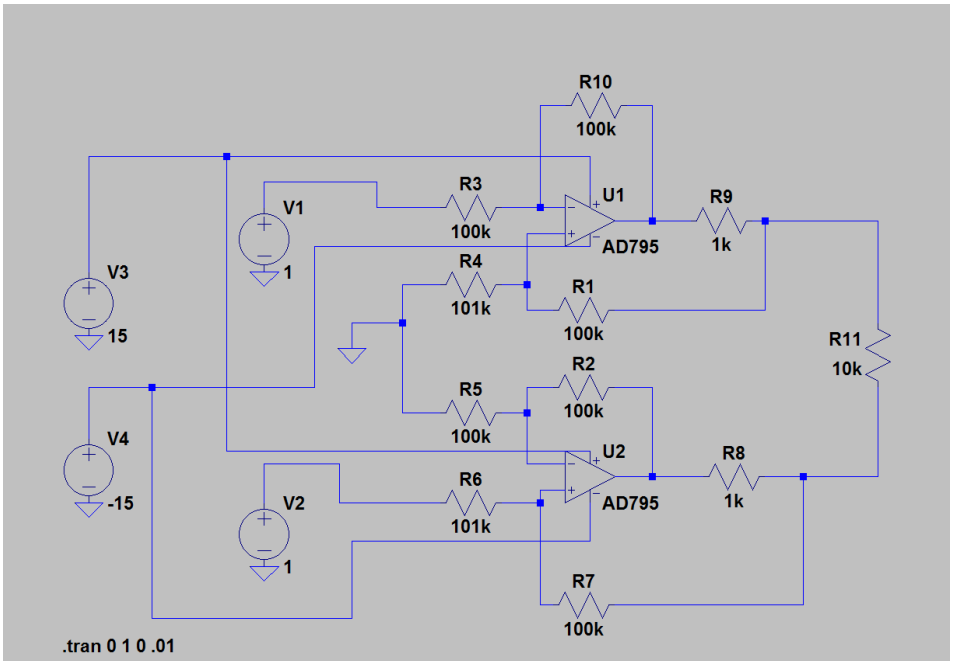

Figure A- 2: Mirrored Modified Howland Current Source. Resistor R11 acts as the test tank load.

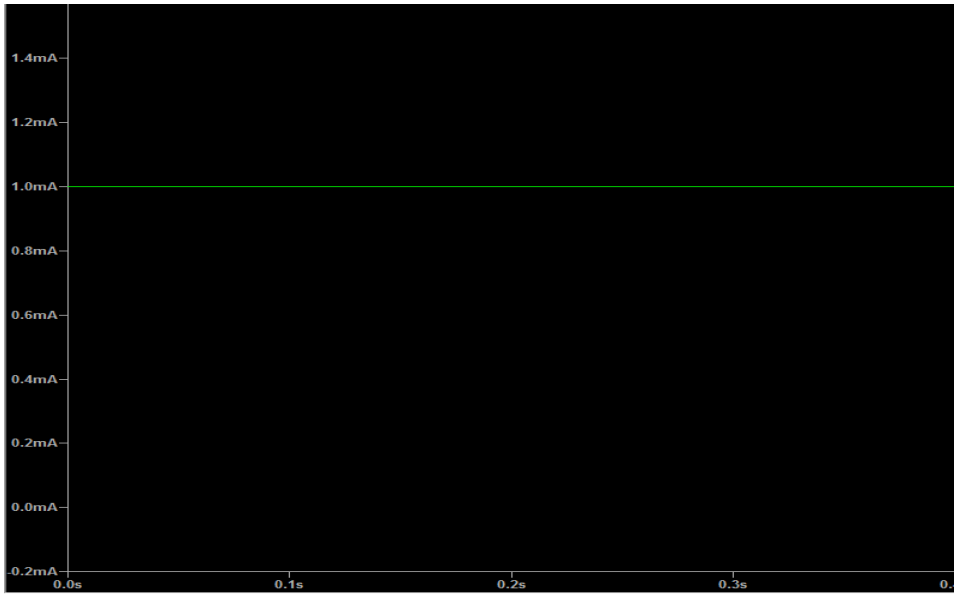

Figure A- 3: Plot of the load current over the load resistor range of 1-10 kilo-ohms. It shows that the current is held at 1mA

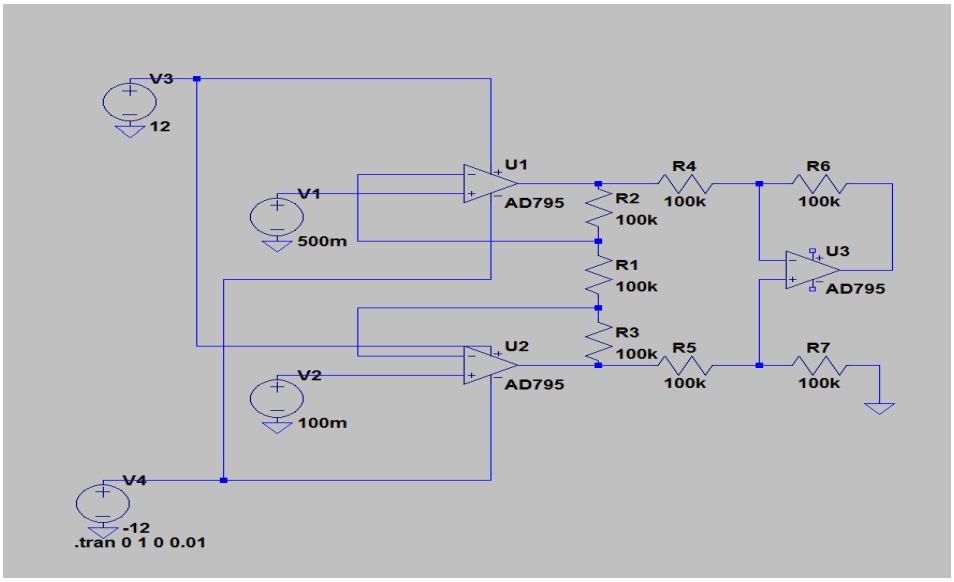

Figure A- 4: Instrument amplifier made from three operational amplifiers within the LM7041N and external 1% resistors. The resistors set an amplifier gain of 3.

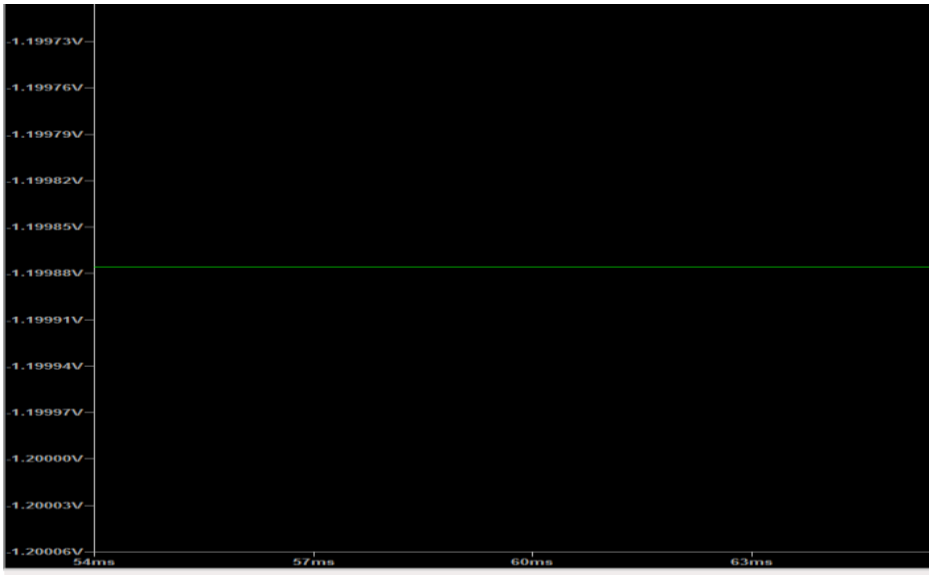

Figure A- 5: Plot of output voltage of the instrument op-amp configuration. It shows that the output voltage matches the expected value of 1.2.

Appendix B: Prototype verification

This appendix contains the graphs used to verify the operations of the prototype EIT system.

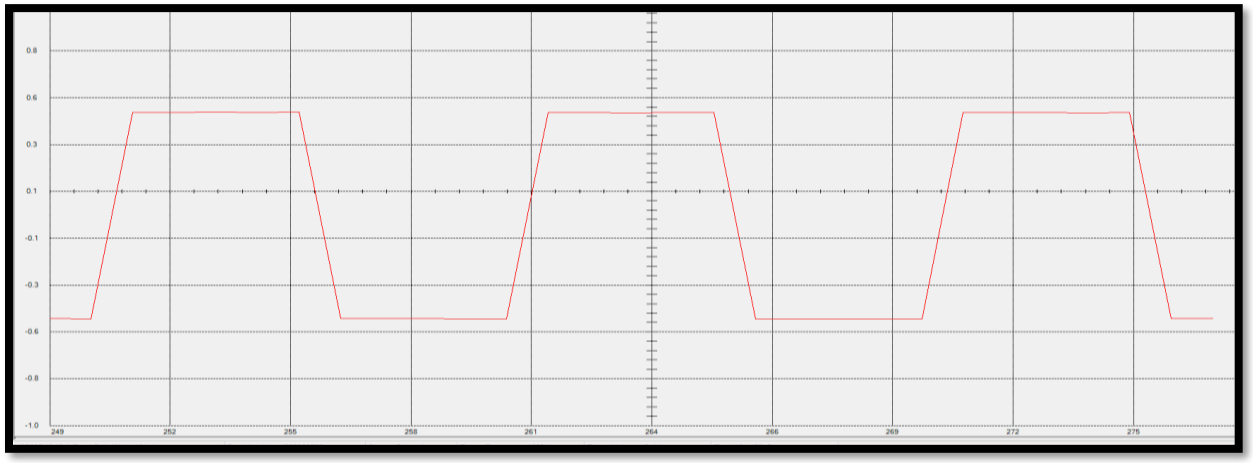

Figure B- 1: Plot of the measured analogue signal. It shows that the input signal, which was 250mV, was amplified by two. The image shows that the peak voltage is 500mV

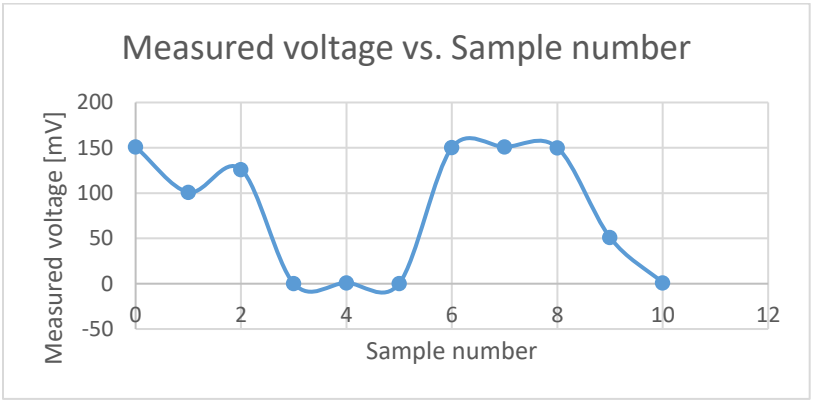

Figure B- 2: Plot of the voltage that was measured by the 24-bit ADC. The plot shows a distorted curve with a DC-offset voltage. Further calibration is needed.

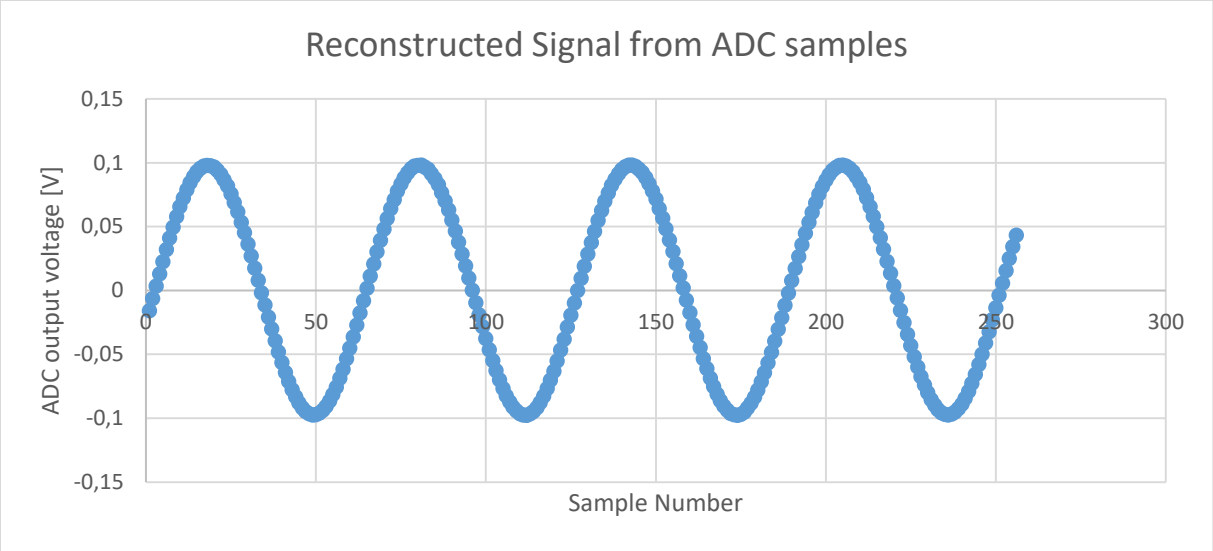

Figure B- 3: Plot of the measured voltage after correcting the operation mode. Plot shows that the 100 mV, 1 kHz sinusoidal signal was correctly sampled and plotted.

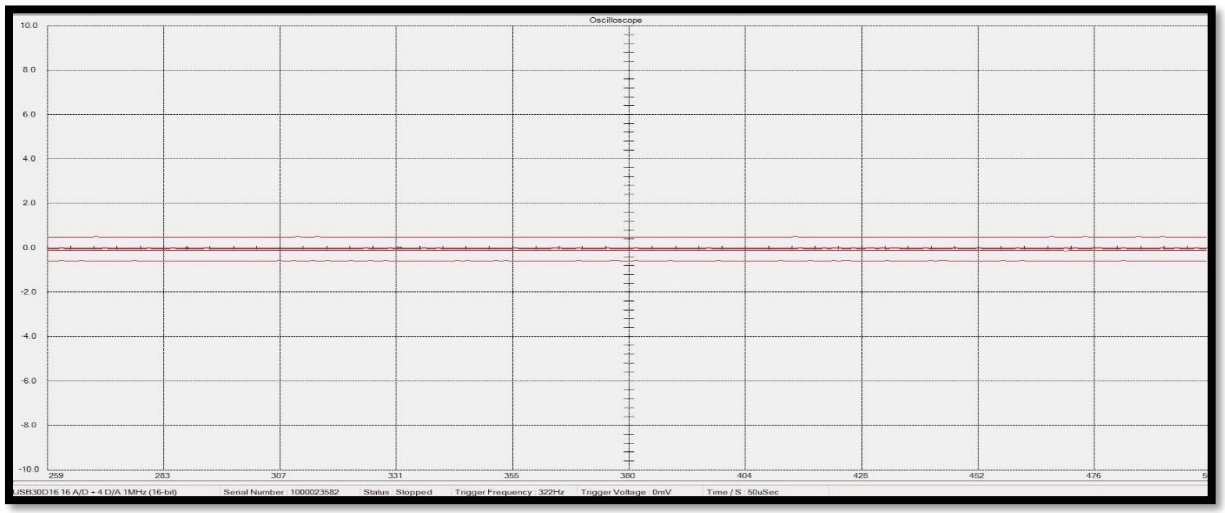

Figure B- 4: Shows the measured signals on each channel when a 1 mA-peak DC signal is applied to the test tank at channel 0. The image shows no evidence of low-frequency drift

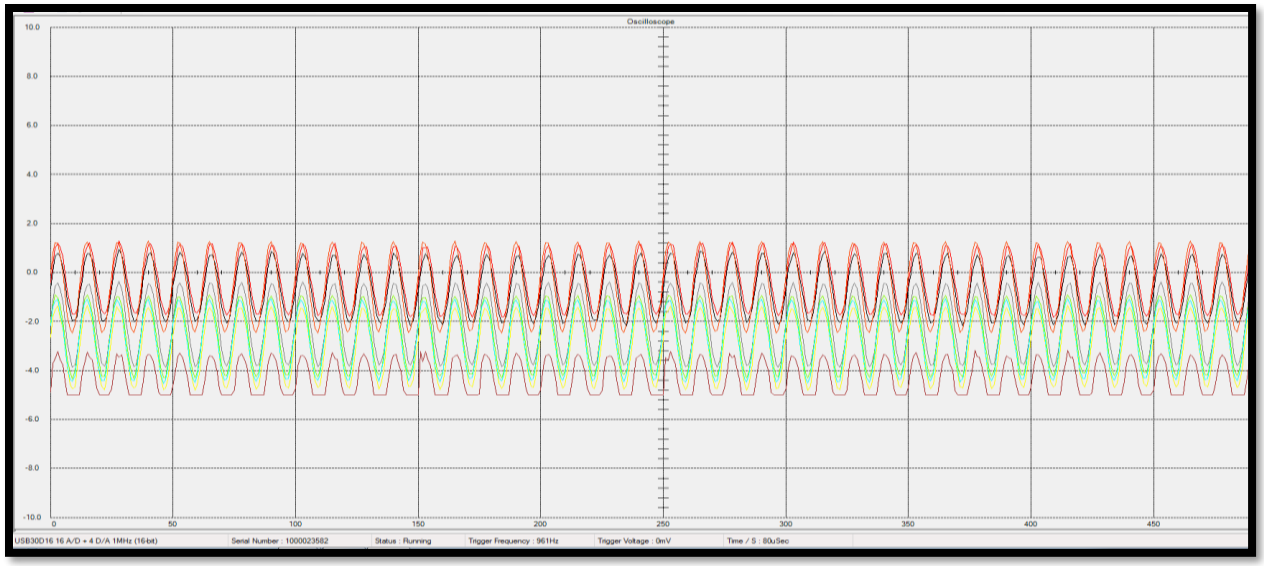

Figure B- 5: Plot of the measured voltage differences per channel, using the 7cm diameter test tank. There are amplitude distinguishable voltage sinusoidal curves at each channel.

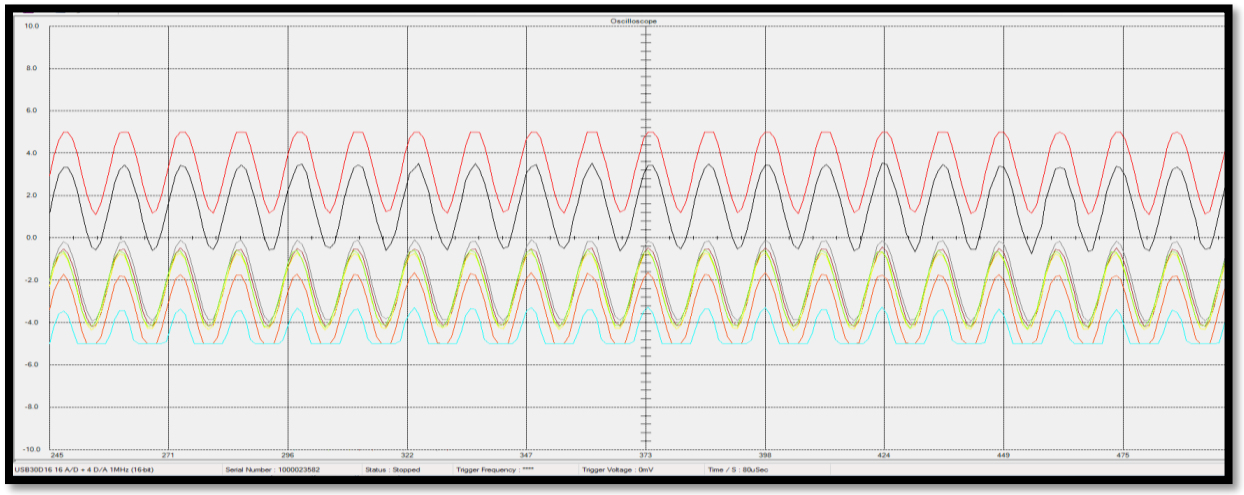

Figure B- 6: Plot of the measured voltage differences per channel, using the 15cm diameter test tank. There are amplitude distinguishable voltage sinusoidal curves at each channel.

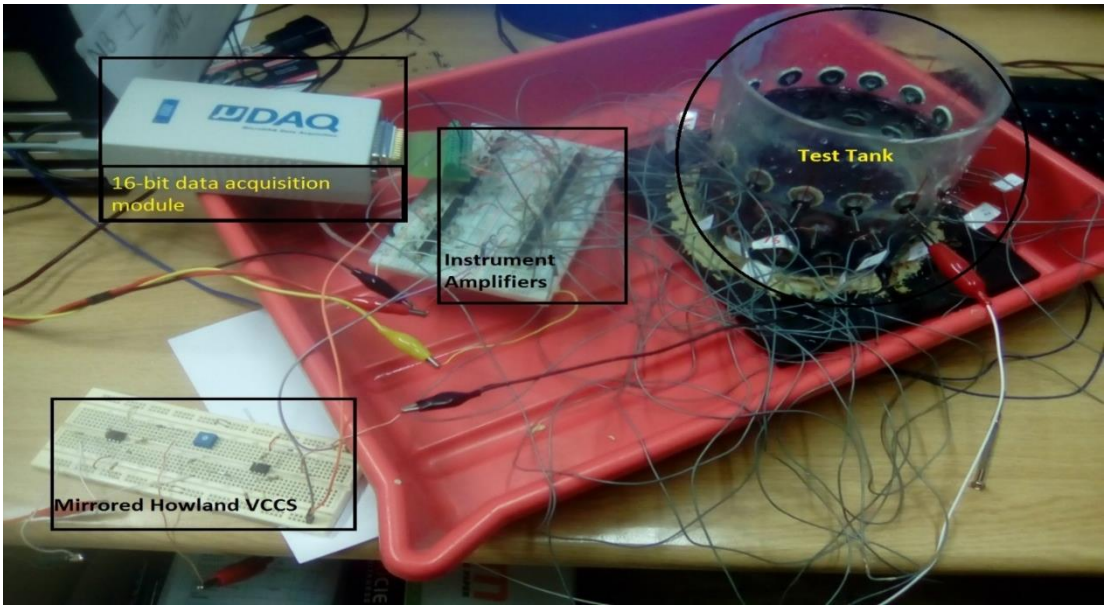

Figure B- 7: 16-bit assembled data acquisition system.

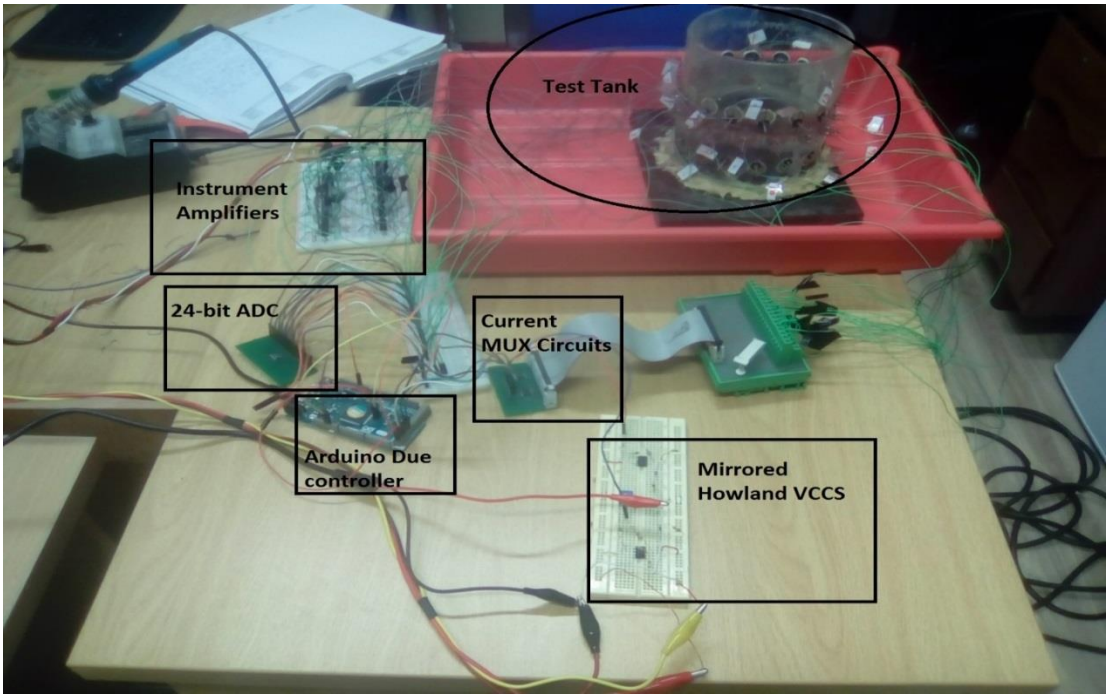

Figure B- 8: Assembled 24-bit EIT system.

Appendix C: Raw test results

This appendix includes the graphs of all raw test results.

The following graphs were recorded during the 24- vs 16-bit tests described in Chapter 7.1

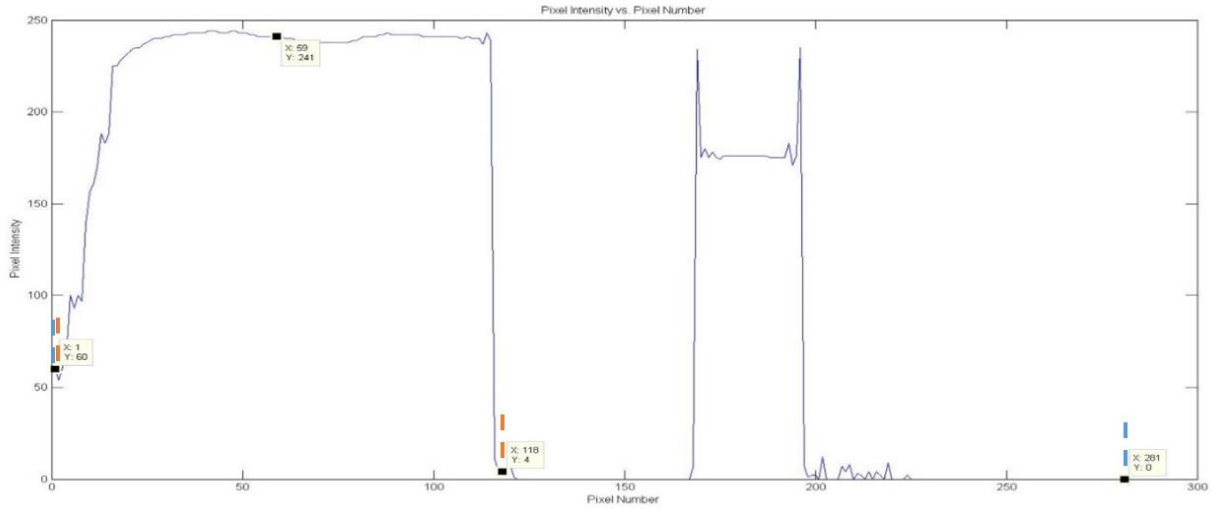

Figure C- 1: Pixel intensity vs. pixel number plot for the 16-bit reconstructed image, showing the relevant points that were used to compute the position and size errors. X values from the left of the plot: 1, 59, 118, and 281.

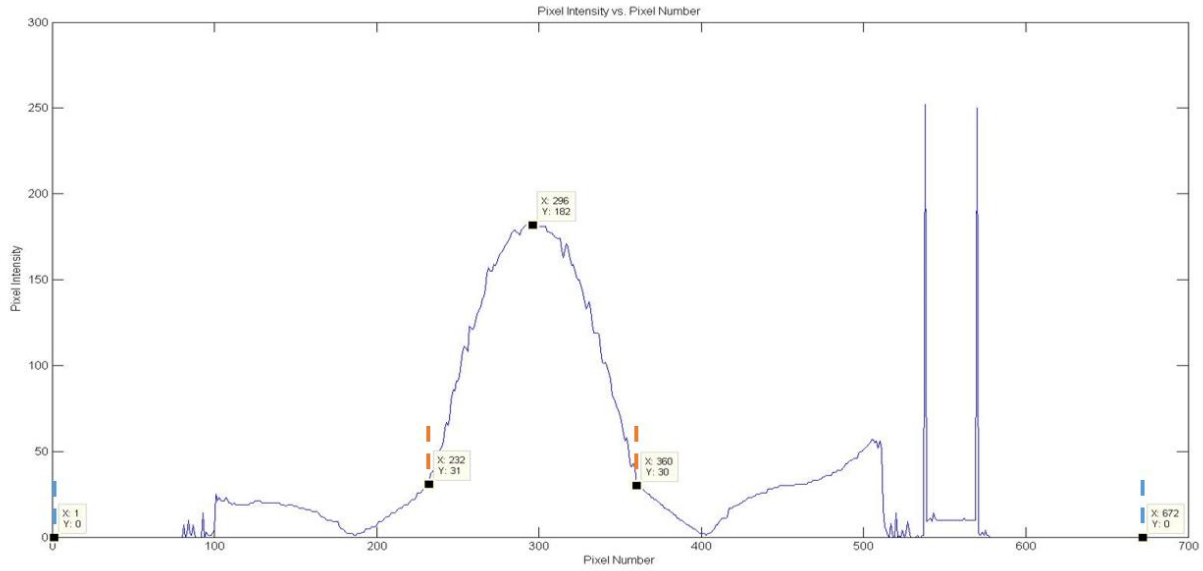

Figure C- 2: Pixel intensity vs. pixel number plot for the 24-bit reconstructed image, showing the relevant points that were used to compute the position and size errors. X values from the left of the plot: 1, 232, 296, 360, 672.

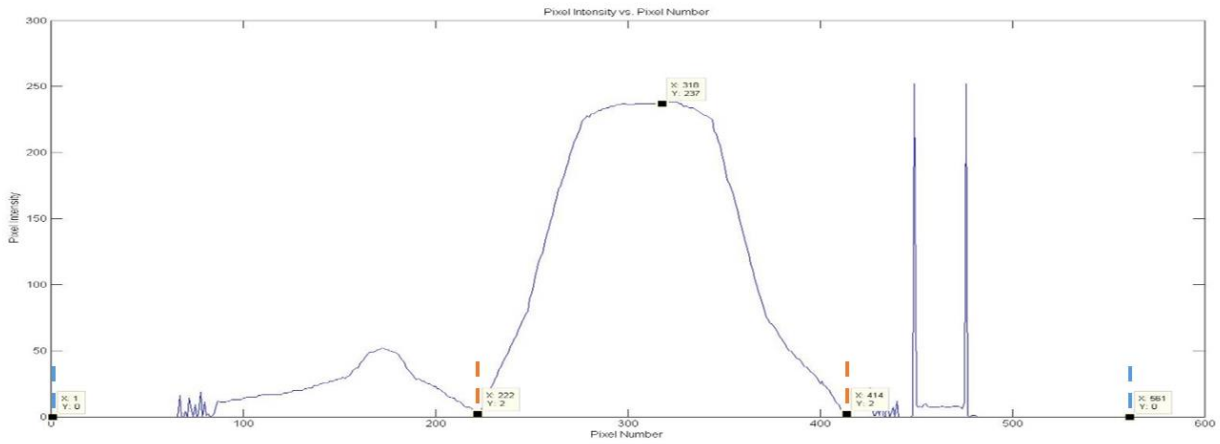

Figure C- 3: Pixel intensity vs. pixel number plot for the 16-bit reconstructed image, showing the relevant points that were used to compute the position and size errors. X values from the left of the plot: 1,222,318,414,561.

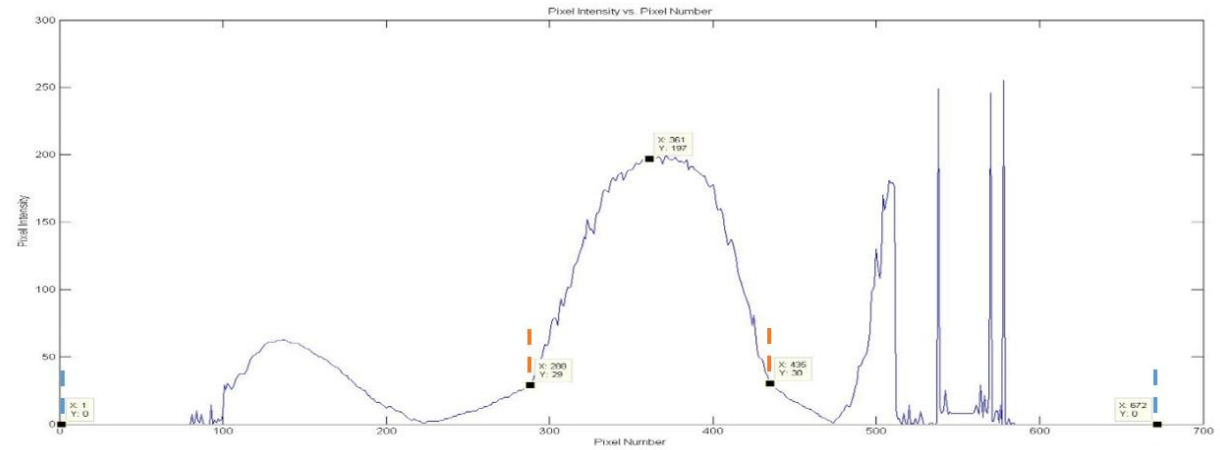

Figure C- 4: Pixel intensity vs. pixel number plot for the 24-bit reconstructed image, showing the relevant points that were used to compute the position and size errors. X values from the left of the plot: 1, 288, 361, 435, and 672.

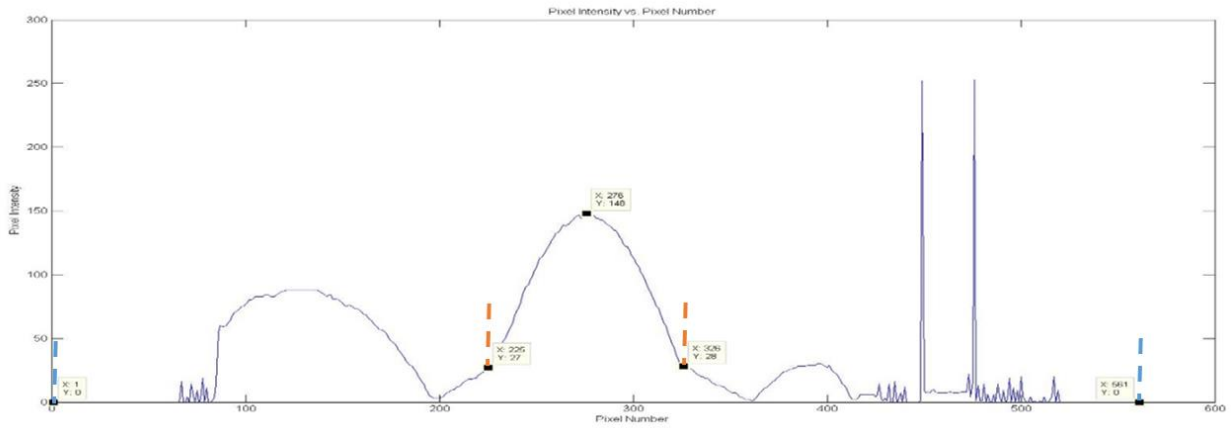

Figure C- 5: Pixel intensity vs. pixel number plot for the 16-bit reconstructed image, showing the relevant points that were used to compute the position and size errors. X values from the left of the plot: 1, 225, 276, 326 and 561.

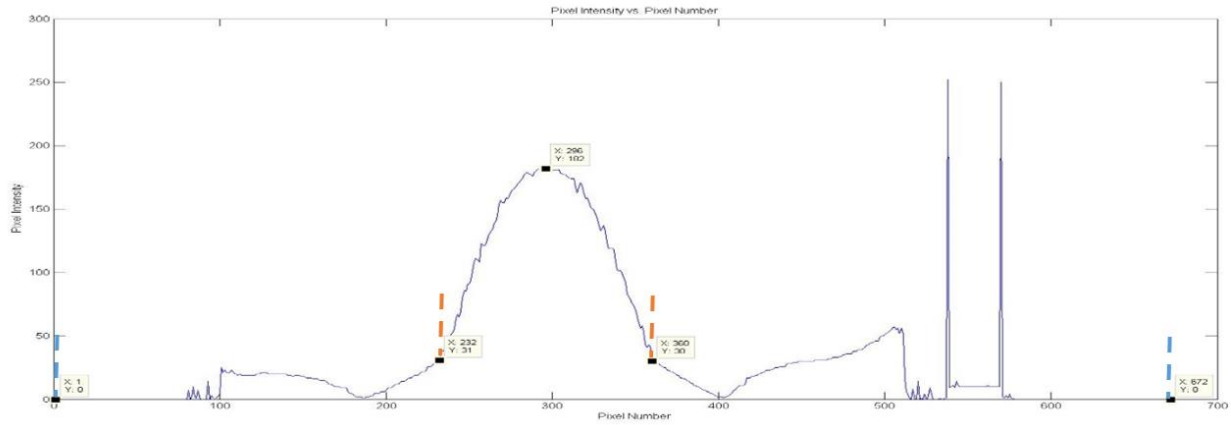

Figure C- 6: Pixel intensity vs. pixel number plot for the 24-bit reconstructed image, showing the relevant points that were used to compute the position and size errors. X values from the left of the plot: 1, 232, 296, 360 and 672.

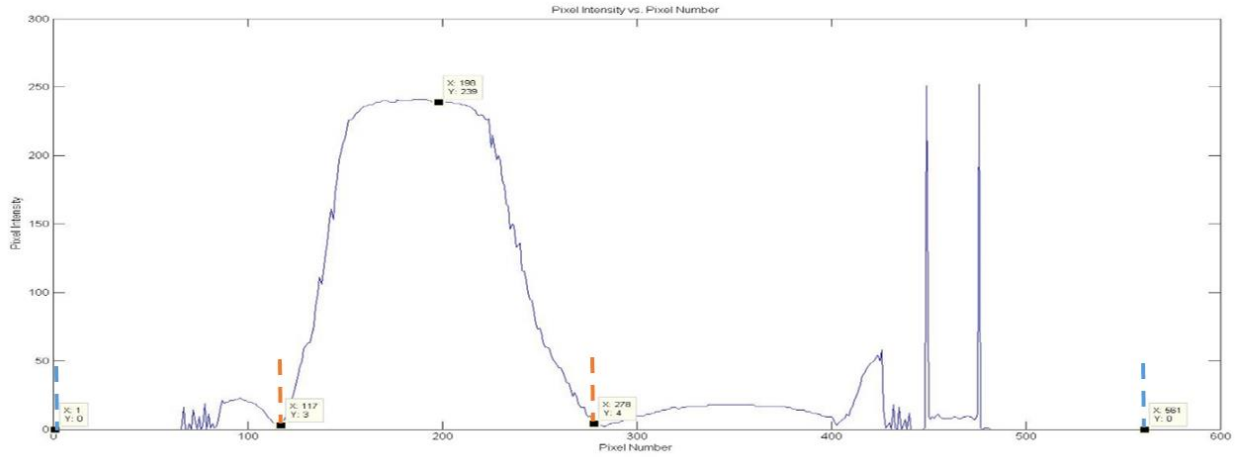

Figure C- 7: Pixel intensity vs. pixel number plot for the 16-bit reconstructed image, showing the relevant points that were used to compute the position and size errors. X values from the left of the plot: 1, 117, 198, 278 and 561.

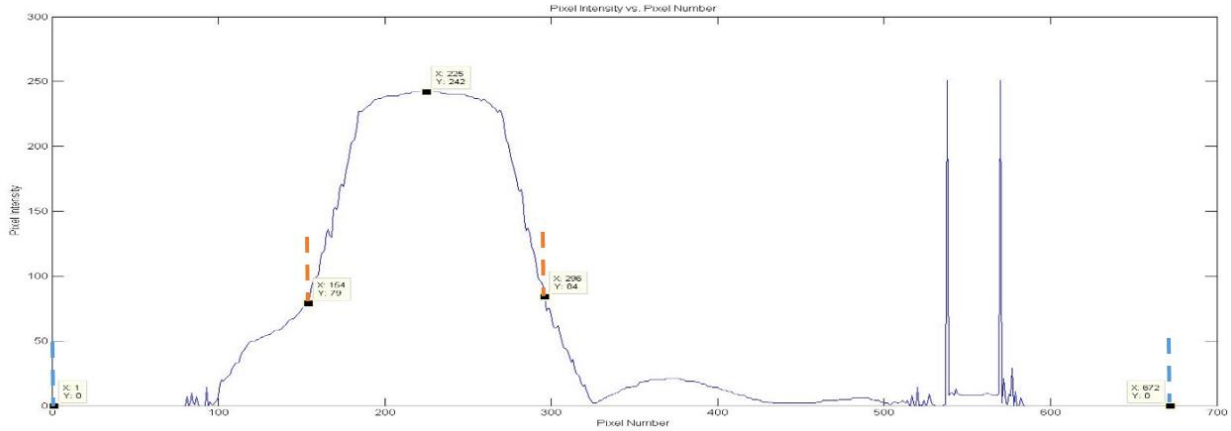

Figure C- 8: Pixel intensity vs. pixel number plot for the 24-bit reconstructed image, showing the relevant points that were used to compute the position and size errors. X values from the left of the plot: 1, 154, 225, 296 and 672.

The following graphs were recorded during the single plane stimulation tests described in Chapter 7.2.1

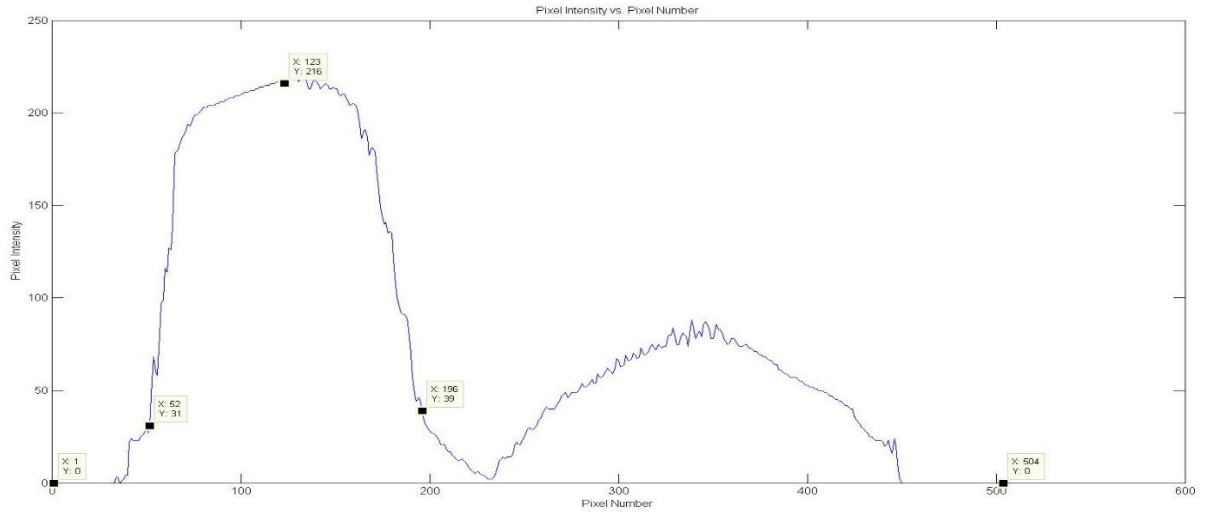

Figure C- 9: Pixel intensity vs. pixel number plot for the reconstructed image when the anomaly was placed at electrode 1. It shows the relevant points that were used to compute the position and size errors. X values from the left of the plot: 1, 52,123, 196 and 504.

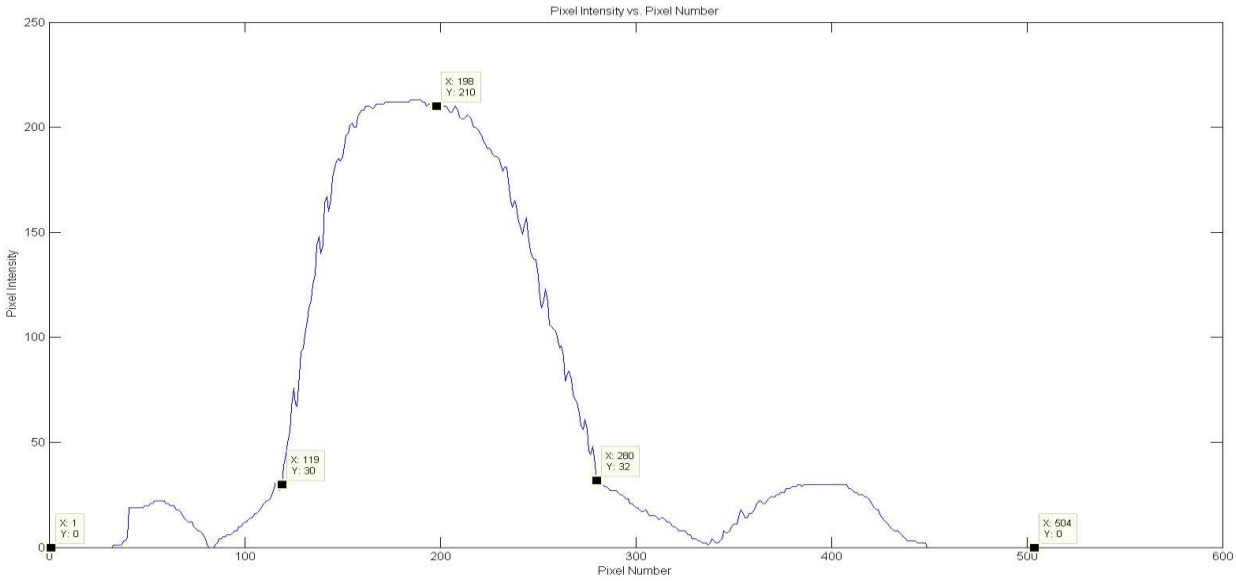

Figure C- 10: Pixel intensity vs. pixel number plot for the reconstructed image when the anomaly was placed at electrode 3. It shows the relevant points that were used to compute the position and size errors. X values from the left of the plot: 1, 119, 198, 280 and 504.

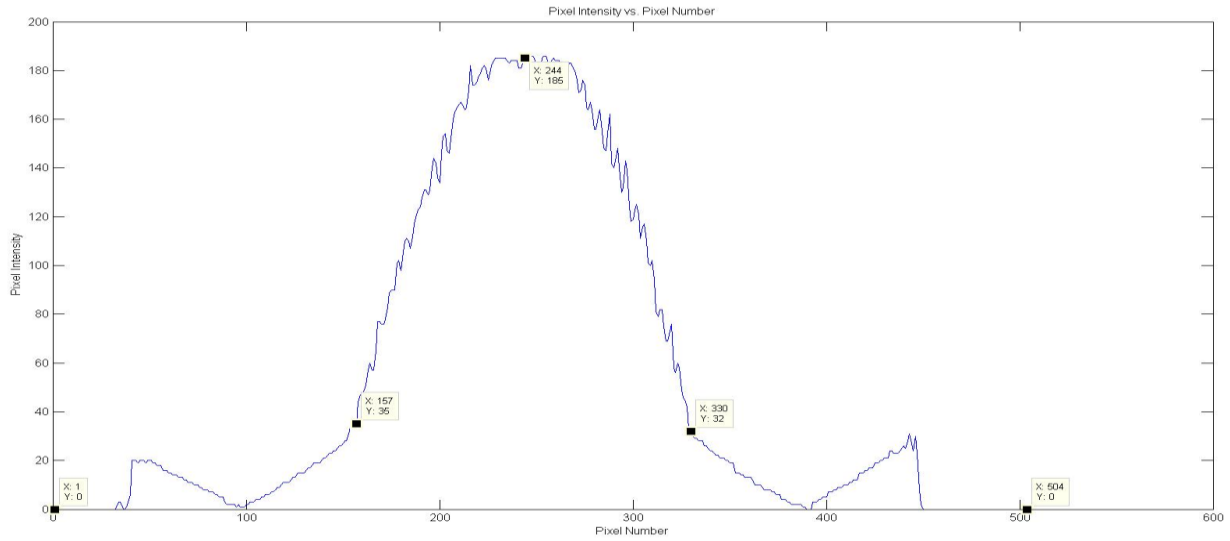

Figure C- 11: Pixel intensity vs. pixel number plot for the reconstructed image when the anomaly was placed at electrode 5. It shows the relevant points that were used to compute the position and size errors. X values from the left of the plot: 1, 157, 244, 330 and 504.

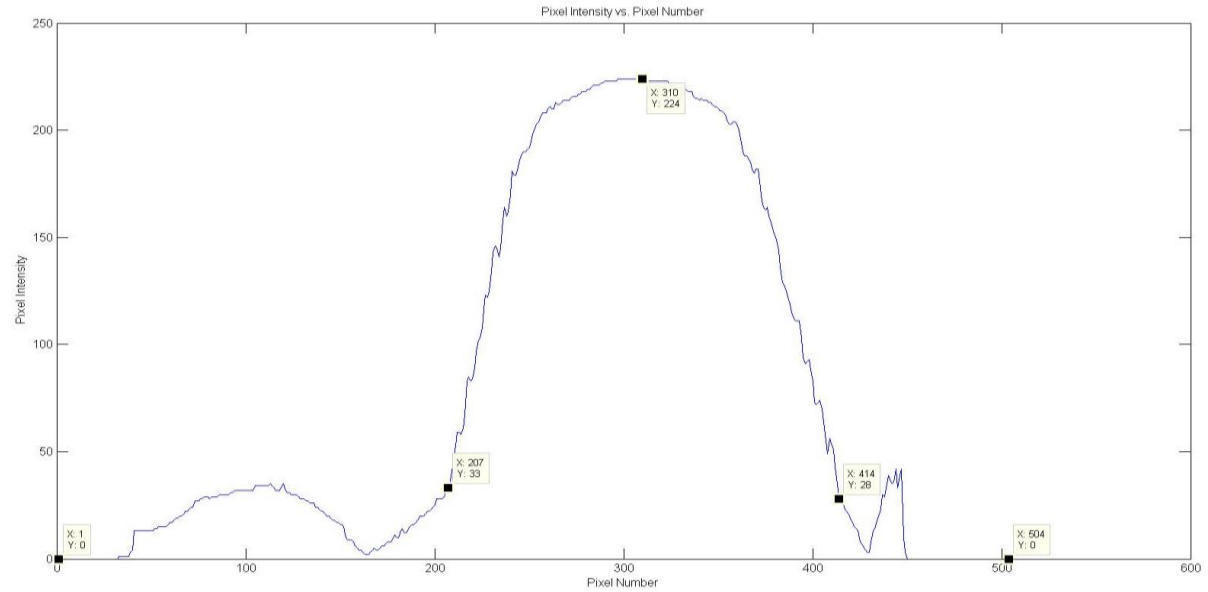

Figure C- 12: Pixel intensity vs. pixel number plot for the reconstructed image when the anomaly was placed at electrode 7. It shows the relevant points that were used to compute the position and size errors. X values from the left of the plot: 1, 207, 310, 414 and 504.

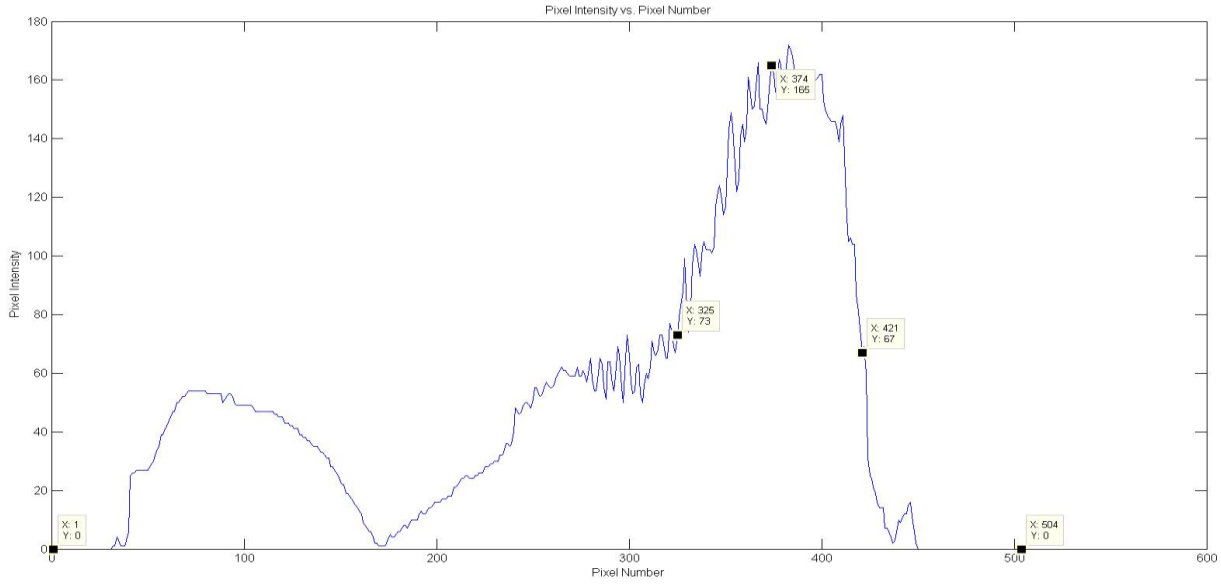

Figure C- 13: Pixel intensity vs. pixel number plot for the reconstructed image when the anomaly was placed at electrode 9. It shows the relevant points that were used to compute the position and size errors. X values from the left of the plot: 1, 325, 374, 421 and 504.

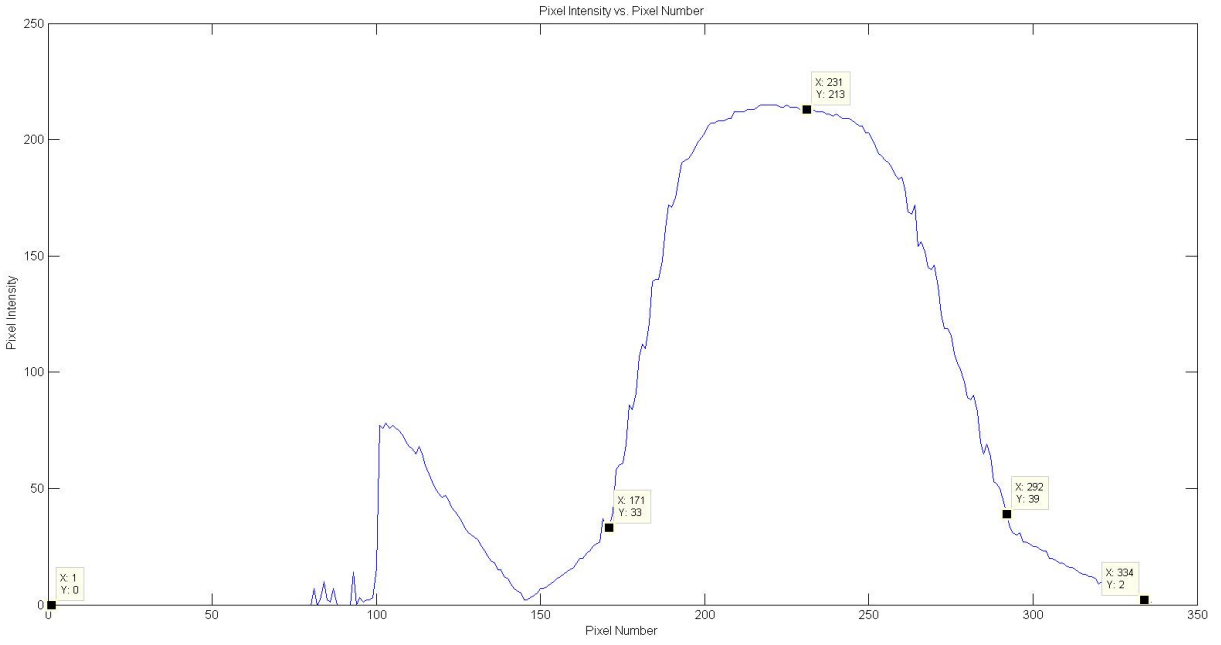

Figure C- 14: Pixel intensity vs. pixel number plot for the reconstructed image when the anomaly was placed at electrode 11. It shows the relevant points that were used to compute the position and size errors. X values from the left of the plot: 1, 171, 231, 292 and 334.

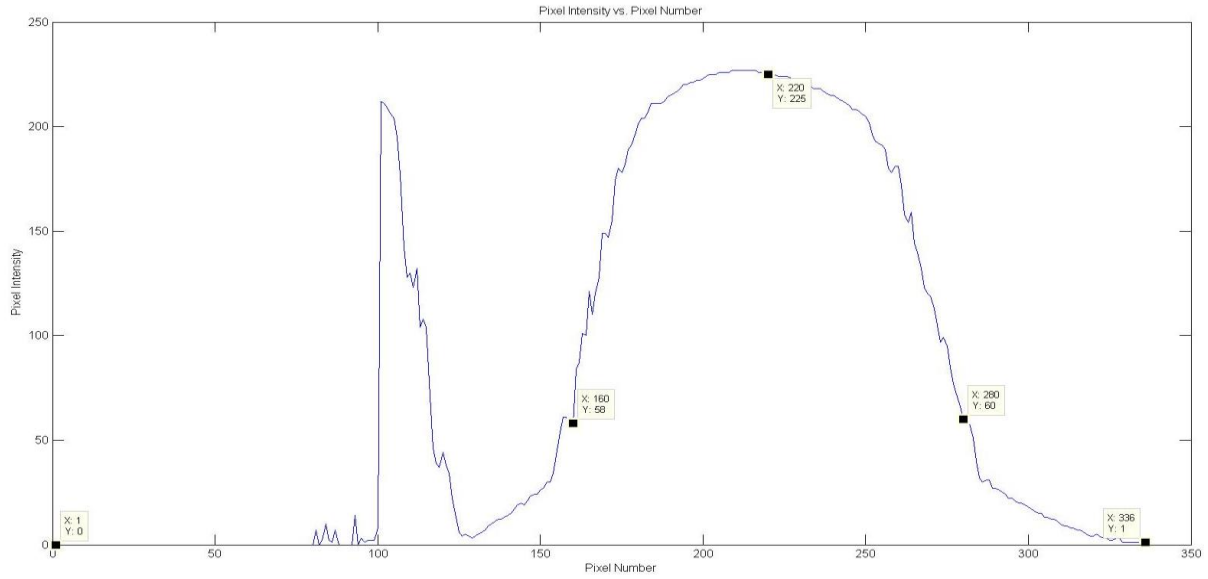

Figure C- 15: Pixel intensity vs. pixel number plot for the reconstructed image when the anomaly was placed at electrode 13. It shows the relevant points that were used to compute the position and size errors. X values from the left of the plot: 1, 160, 220, 280 and 336.

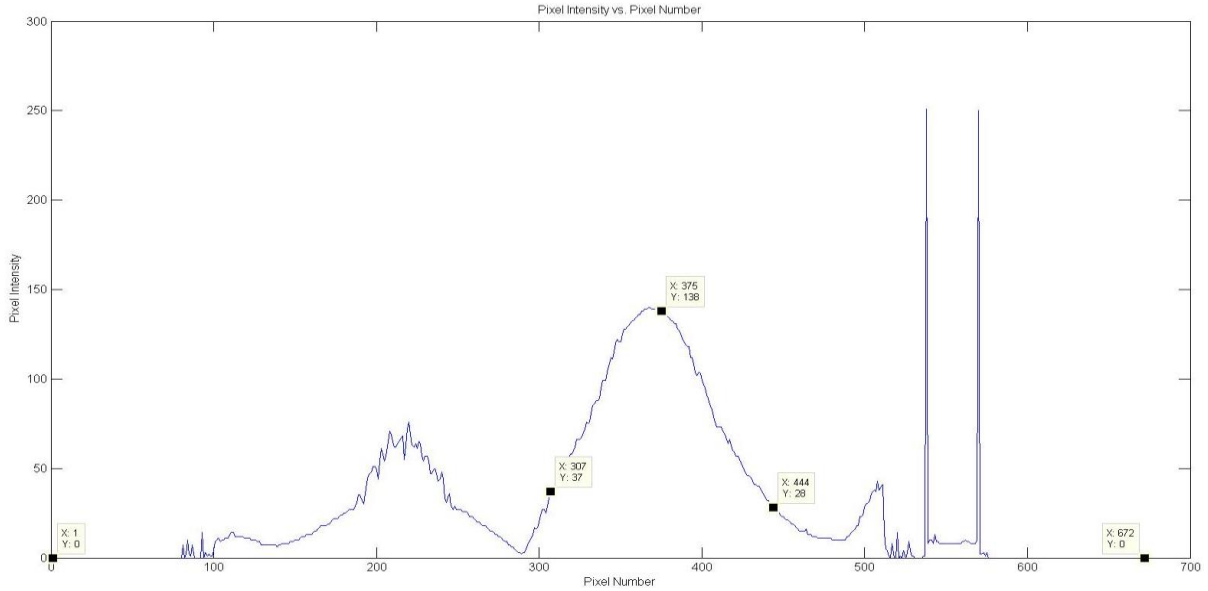

Figure C- 16: Pixel intensity vs. pixel number plot for the reconstructed image when the anomaly was placed at electrode 15. It shows the relevant points that were used to compute the position and size errors. X values from the left of the plot: 1, 307, 375, 444 and 672.

The following graphs were recorded during the cross plane stimulation tests described in Chapter 7.2.2

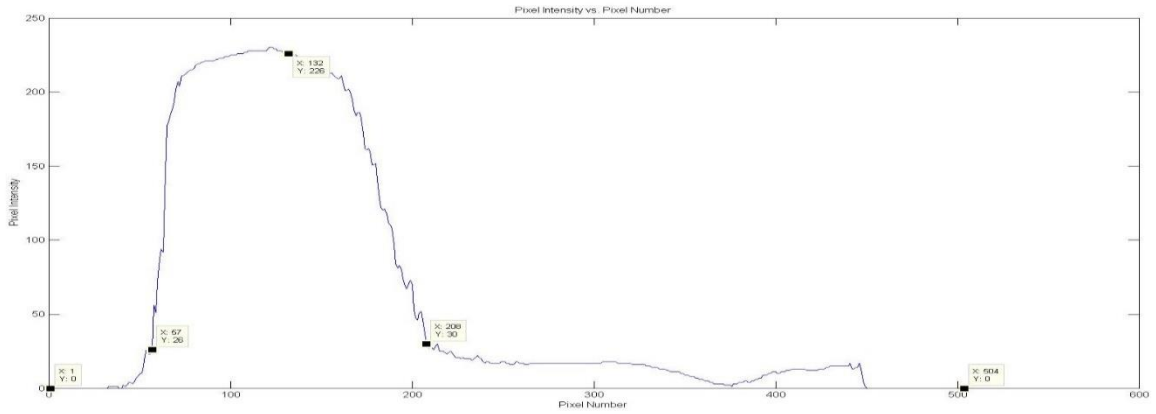

Figure C- 17: Pixel intensity vs. pixel number plot for the reconstructed image when the anomaly was placed at electrode 1. It shows the relevant points that were used to compute the position and size errors. X values from the left of the plot: 1, 57, 132, 208 and 504.

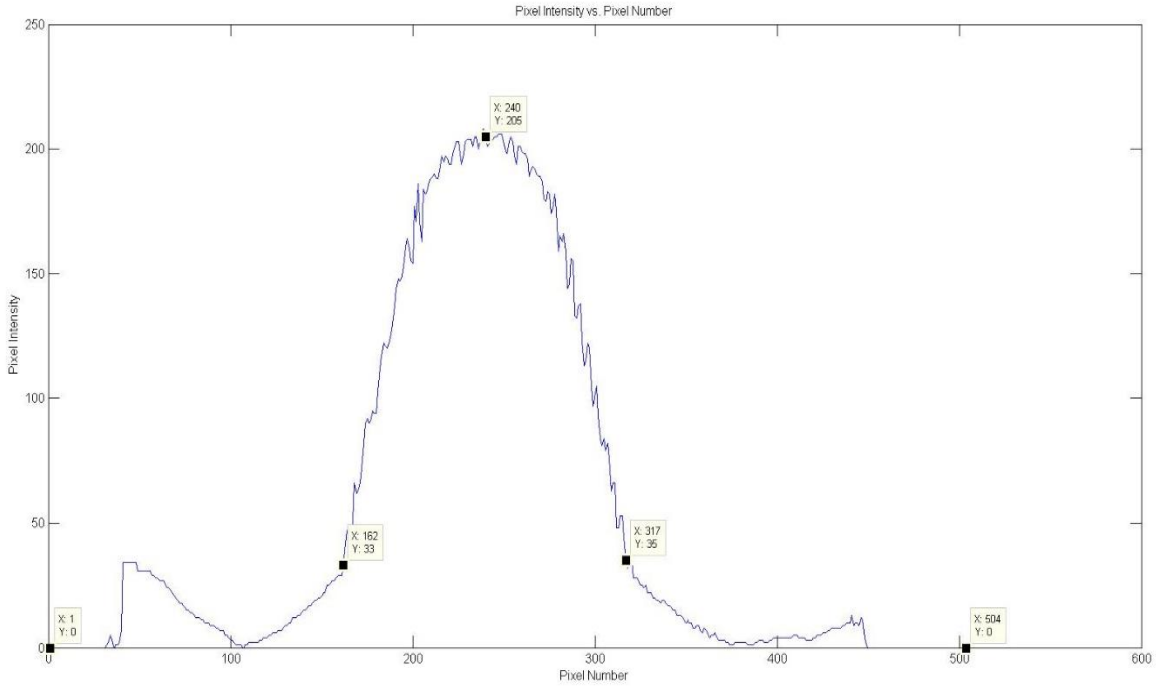

Figure C- 18: Pixel intensity vs. pixel number plot for the reconstructed image when the anomaly was placed at electrode 3. It shows the relevant points that were used to compute the position and size errors. X values from the left of the plot: 1, 162, 240, 317 and 504.

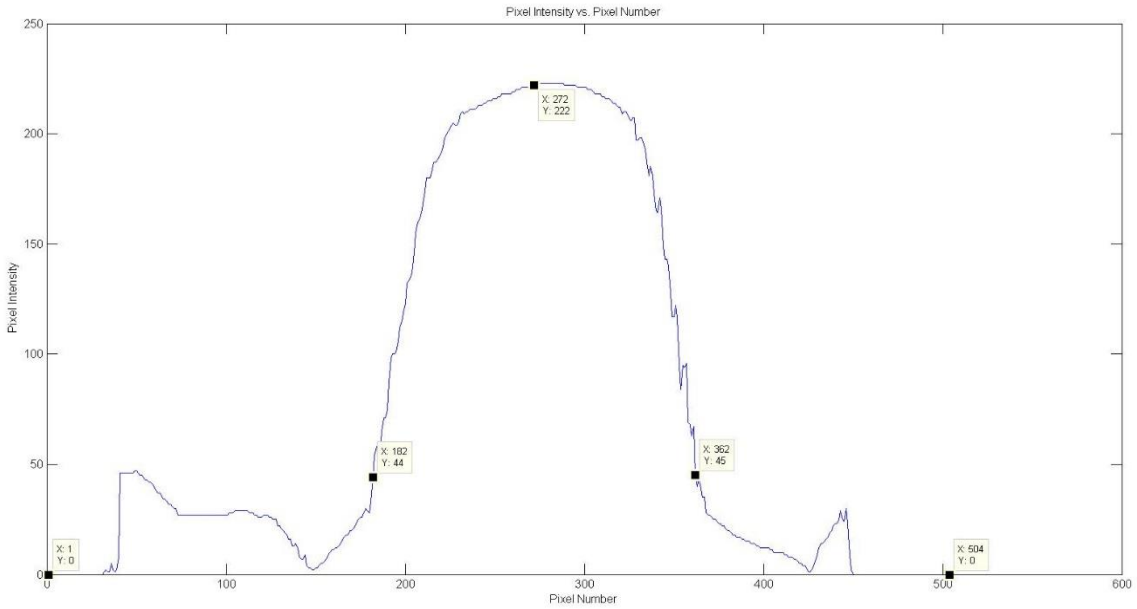

Figure C- 19: Pixel intensity vs. pixel number plot for the reconstructed image when the anomaly was placed at electrode 5. It shows the relevant points that were used to compute the position and size errors. X values from the left of the plot:1, 182, 272, 362 and 504.

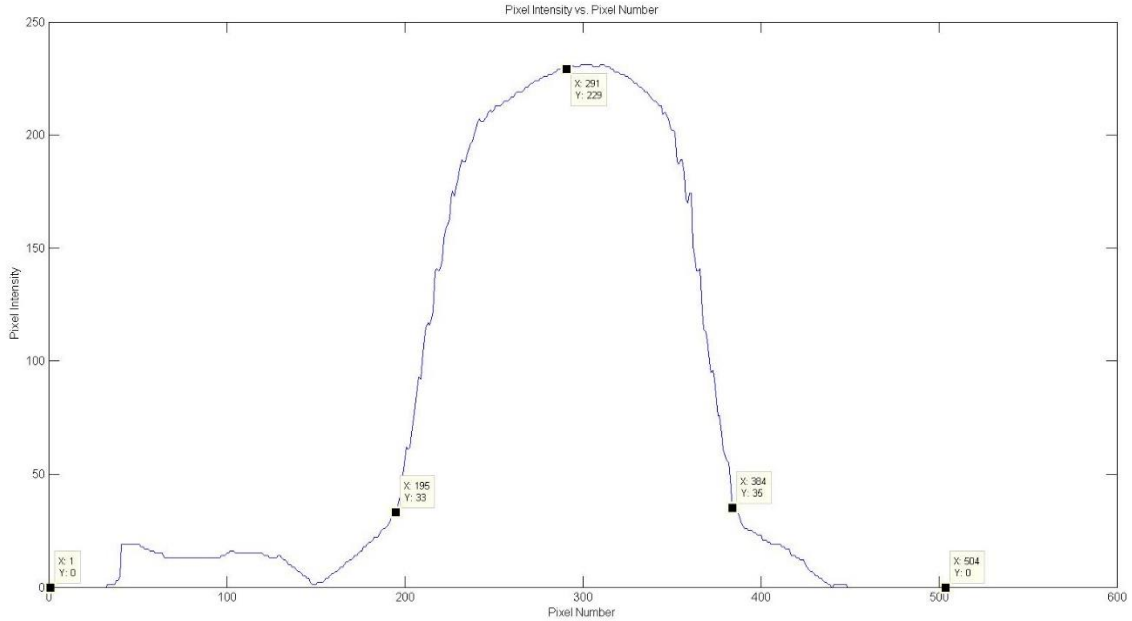

Figure C- 20: Pixel intensity vs. pixel number plot for the reconstructed image when the anomaly was placed at electrode 7. It shows the relevant points that were used to compute the position and size errors. X values from the left of the plot: 1, 195, 291, 384 and 504.

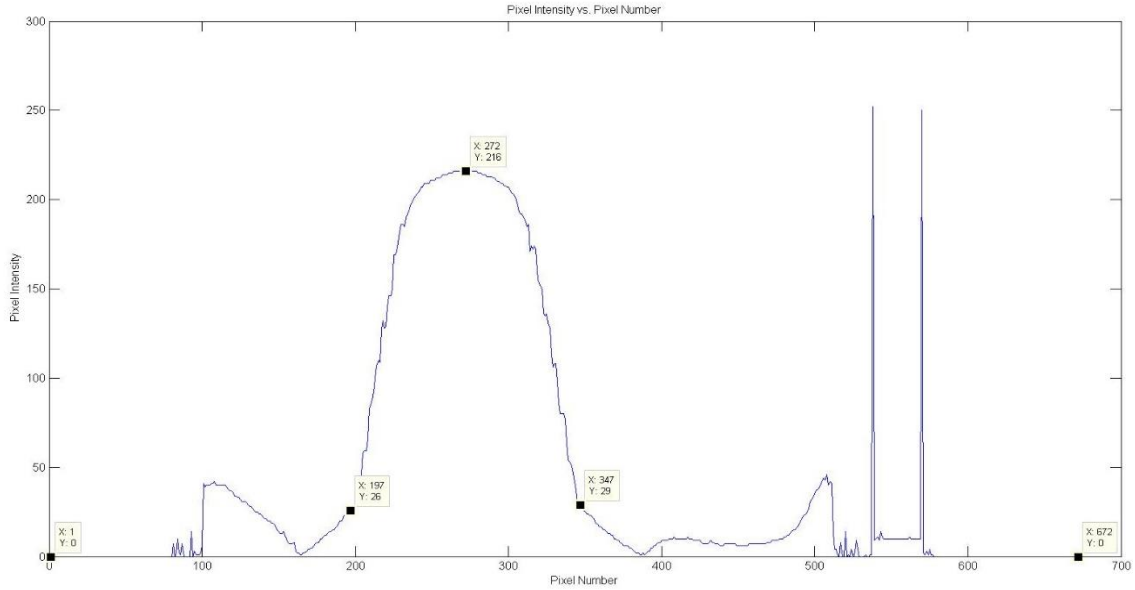

Figure C- 21: Pixel intensity vs. pixel number plot for the reconstructed image when the anomaly was placed at electrode 9. It shows the relevant points that were used to compute the position and size errors. X values from the left of the plot: 1, 197, 272, 347 and 672.

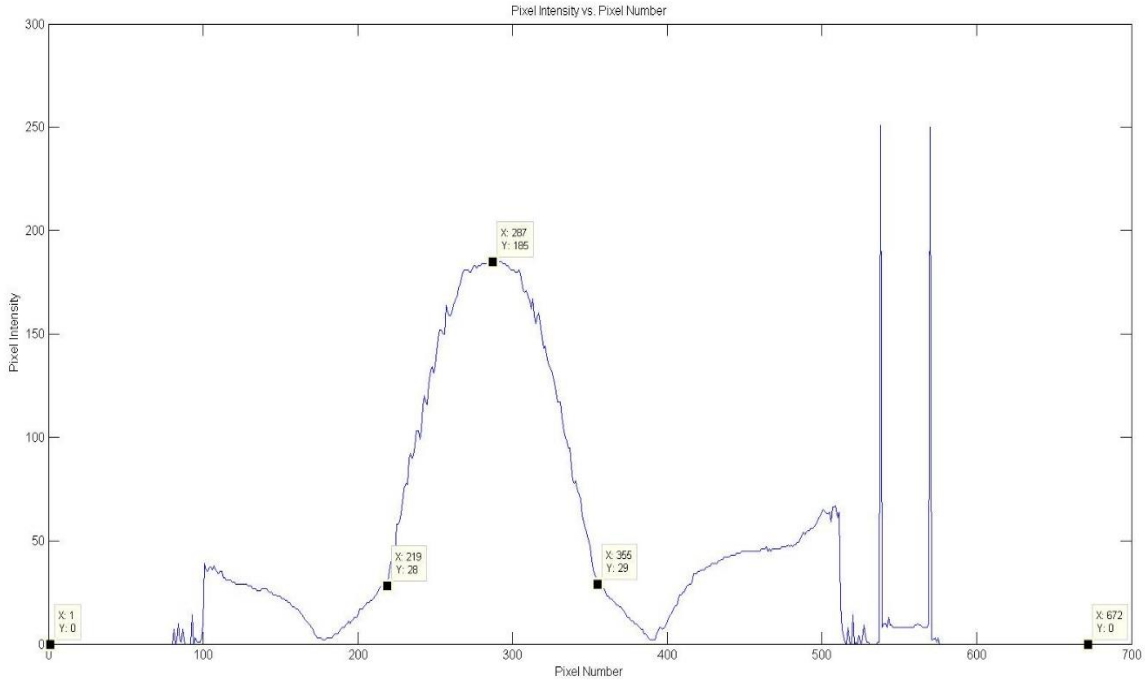

Figure C- 22: Pixel intensity vs. pixel number plot for the reconstructed image when the anomaly was placed at electrode 11. It shows the relevant points that were used to compute the position and size errors. X values from the left of the plot: 1, 219, 287, 355 and 672.

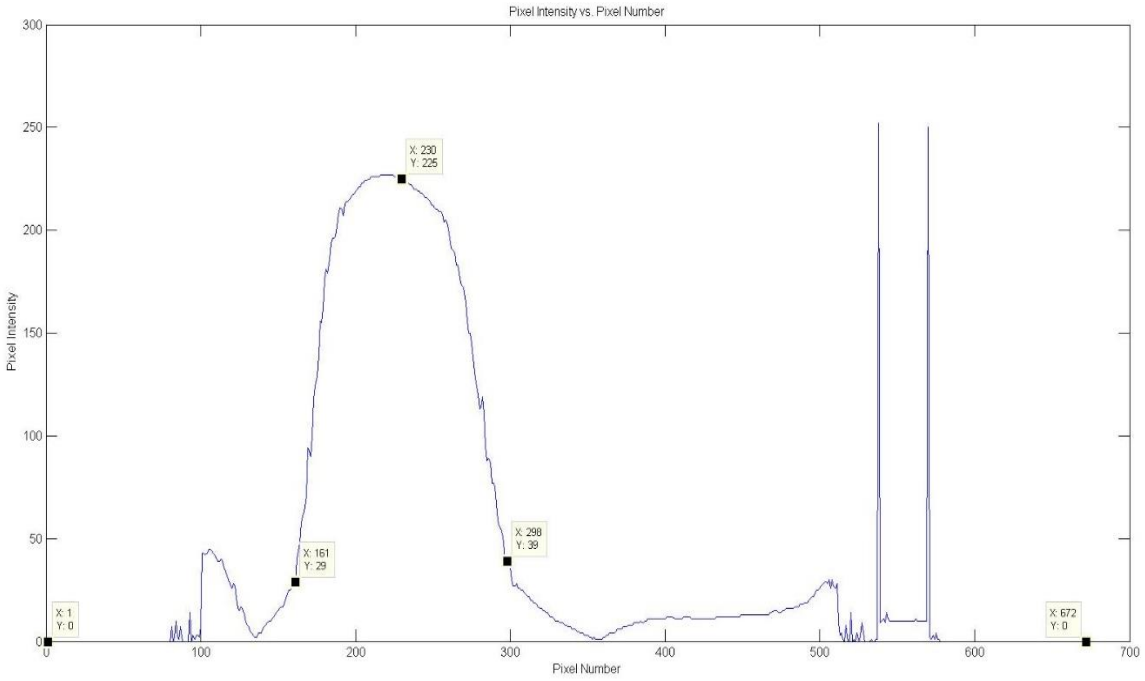

Figure C- 23: Pixel intensity vs. pixel number plot for the reconstructed image when the anomaly was placed at electrode 13. It shows the relevant points that were used to compute the position and size errors. X values from the left of the plot: 1, 161, 230, 298 and 672.

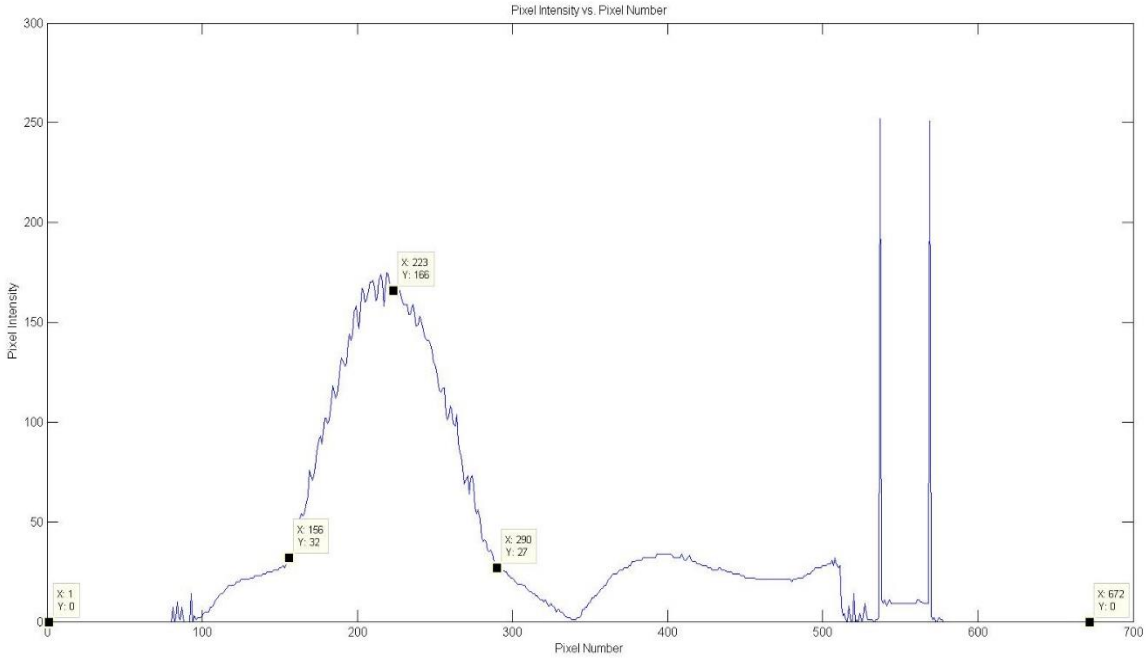

Figure C- 24: Pixel intensity vs. pixel number plot for the reconstructed image when the anomaly was placed at electrode 15. It shows the relevant points that were used to compute the position and size errors. X values from the left of the plot: 1, 156, 223, 290 and 672.

The following graphs were recorded during the dual current stimulation tests described in Chapter 7.2.2

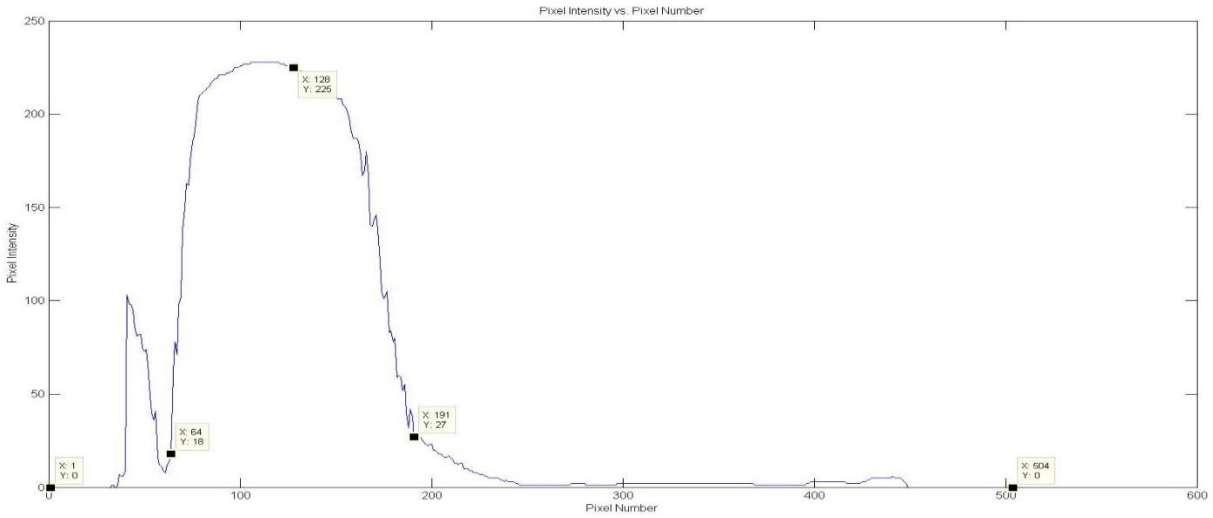

Figure C- 25: Pixel intensity vs. pixel number plot for the reconstructed image when the anomaly was placed at electrode 1. It shows the relevant points that were used to compute the position and size errors. X values from the left of the plot: 1, 64, 128, 191 and 504.

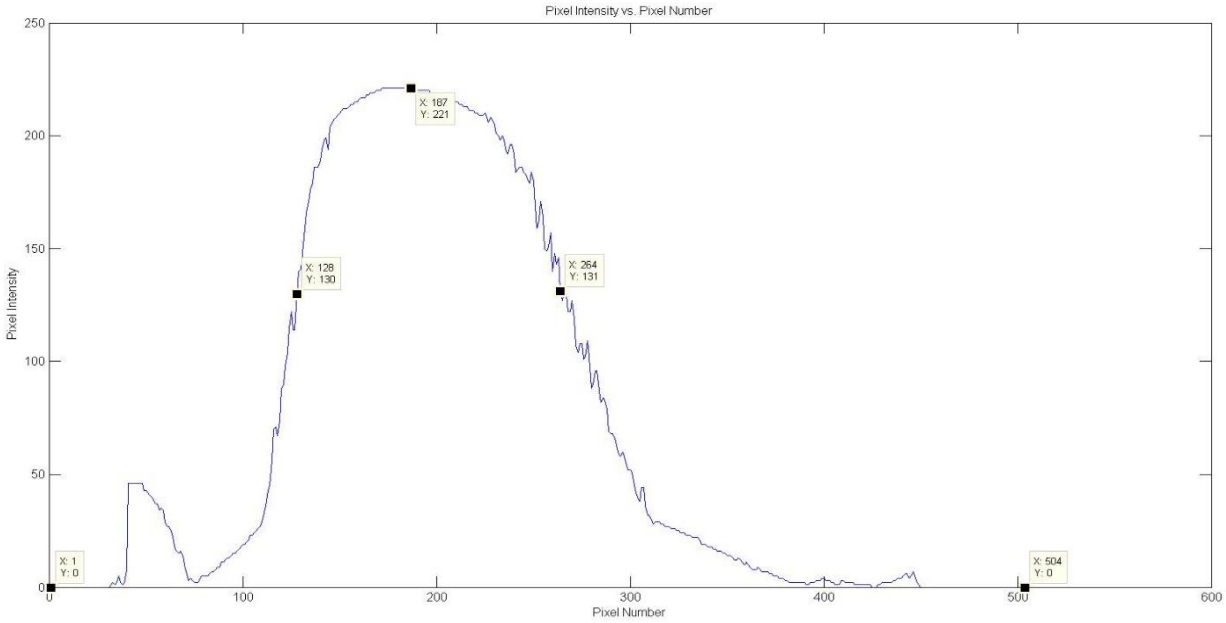

Figure C- 26: Pixel intensity vs. pixel number plot for the reconstructed image when the anomaly was placed at electrode 3. It shows the relevant points that were used to compute the position and size errors. X values from the left of the plot:1, 128, 187, 264 and 504.

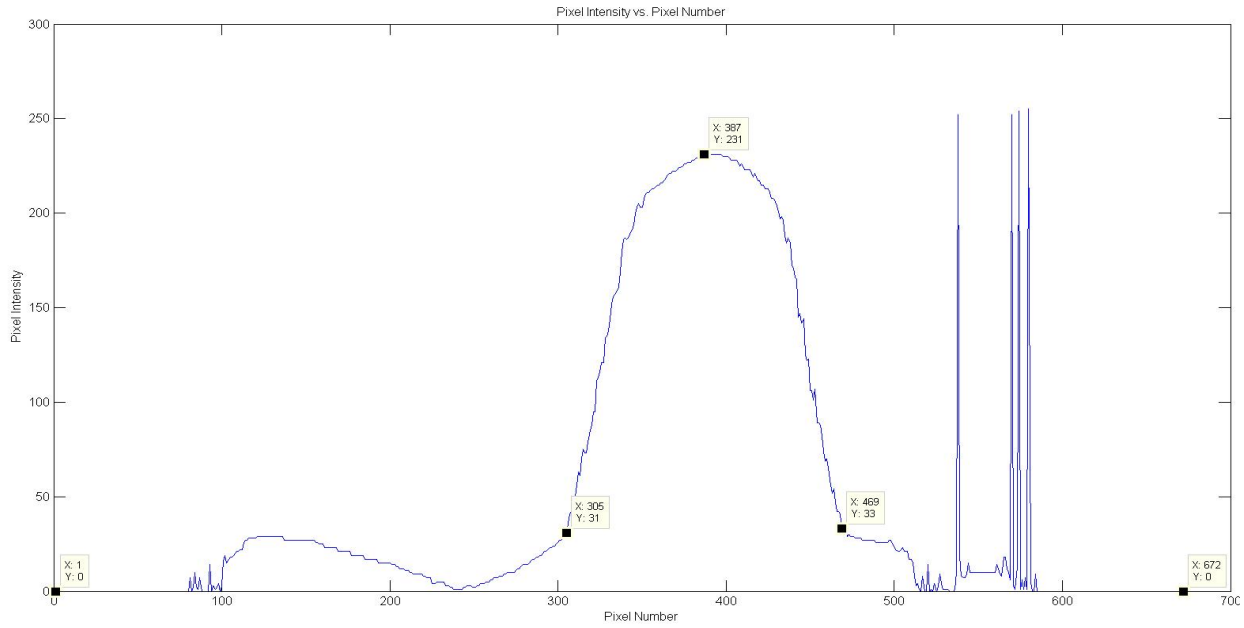

Figure C- 27: Pixel intensity vs. pixel number plot for the reconstructed image when the anomaly was placed at electrode 5. It shows the relevant points that were used to compute the position and size errors. X values from the left of the plot: 1, 305, 387, 469 and 672.

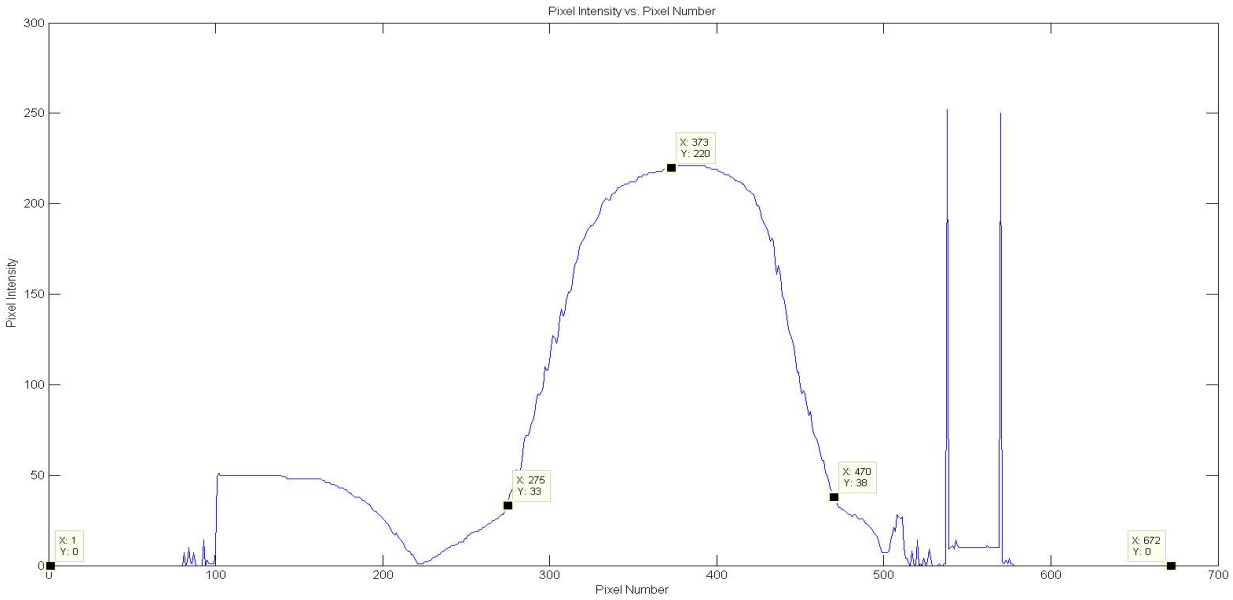

Figure C- 28: Pixel intensity vs. pixel number plot for the reconstructed image when the anomaly was placed at electrode 7. It shows the relevant points that were used to compute the position and size errors. X values from the left of the plot: 1, 275, 373, 470 and 672.

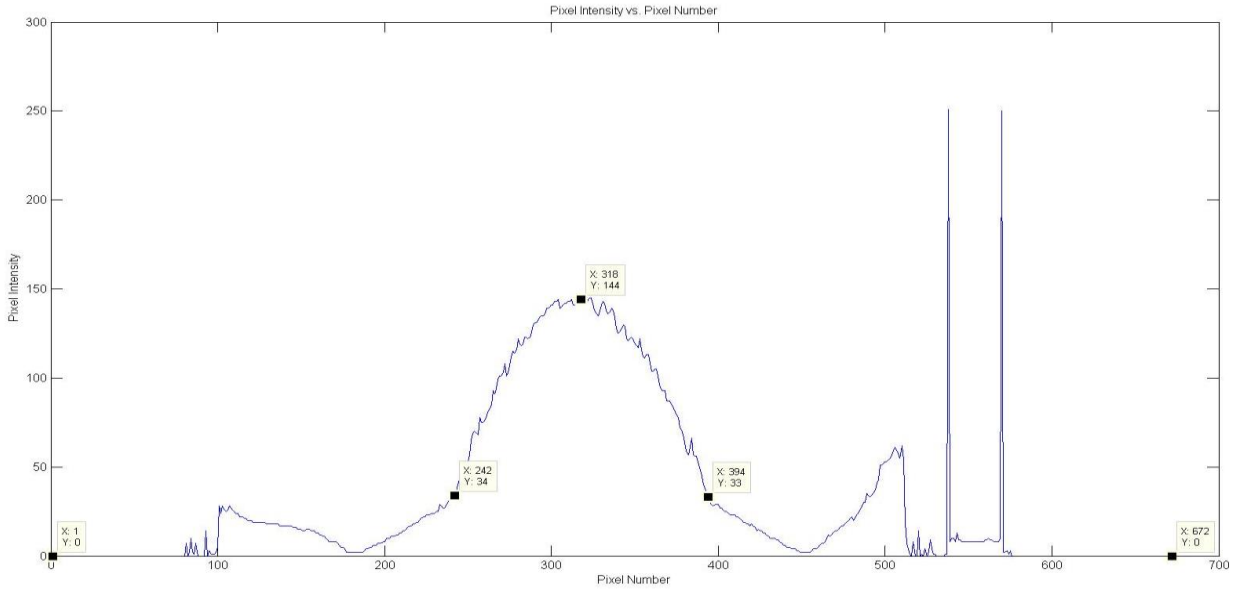

Figure C- 29: Pixel intensity vs. pixel number plot for the reconstructed image when the anomaly was placed at electrode 9. It shows the relevant points that were used to compute the position and size errors. X values from the left of the plot: 1, 242, 318, 394 and 672

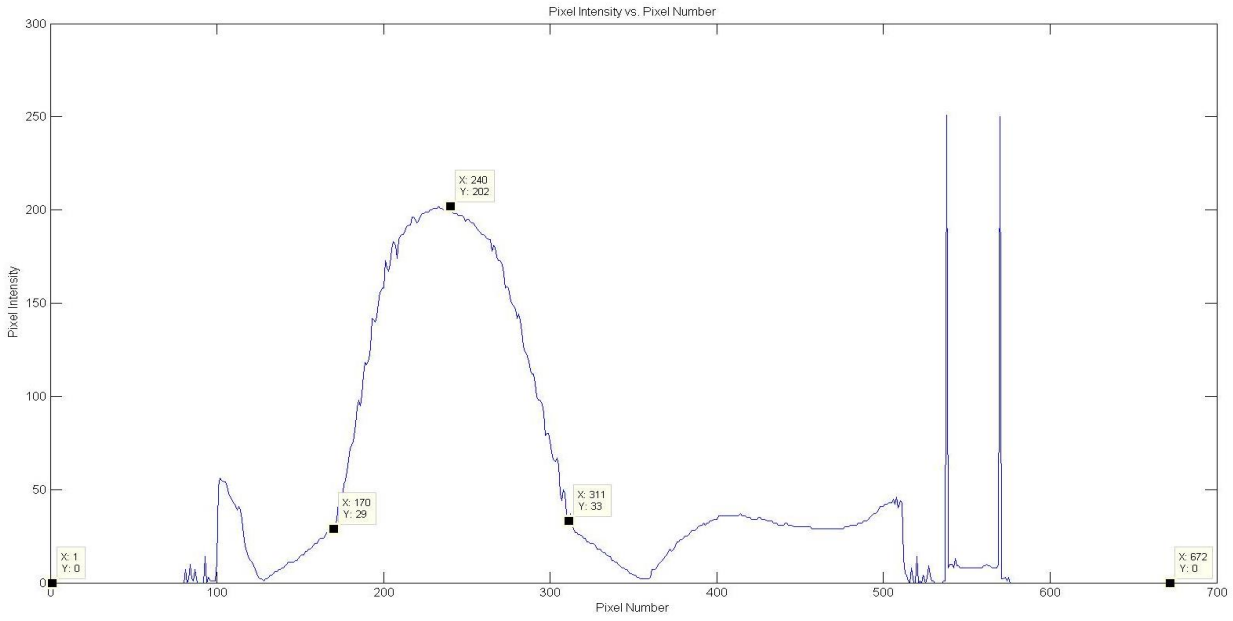

Figure C- 30: Pixel intensity vs. pixel number plot for the reconstructed image when the anomaly was placed at electrode 11. It shows the relevant points that were used to compute the position and size errors. X values from the left of the plot: 1, 170, 240, 311 and 672.

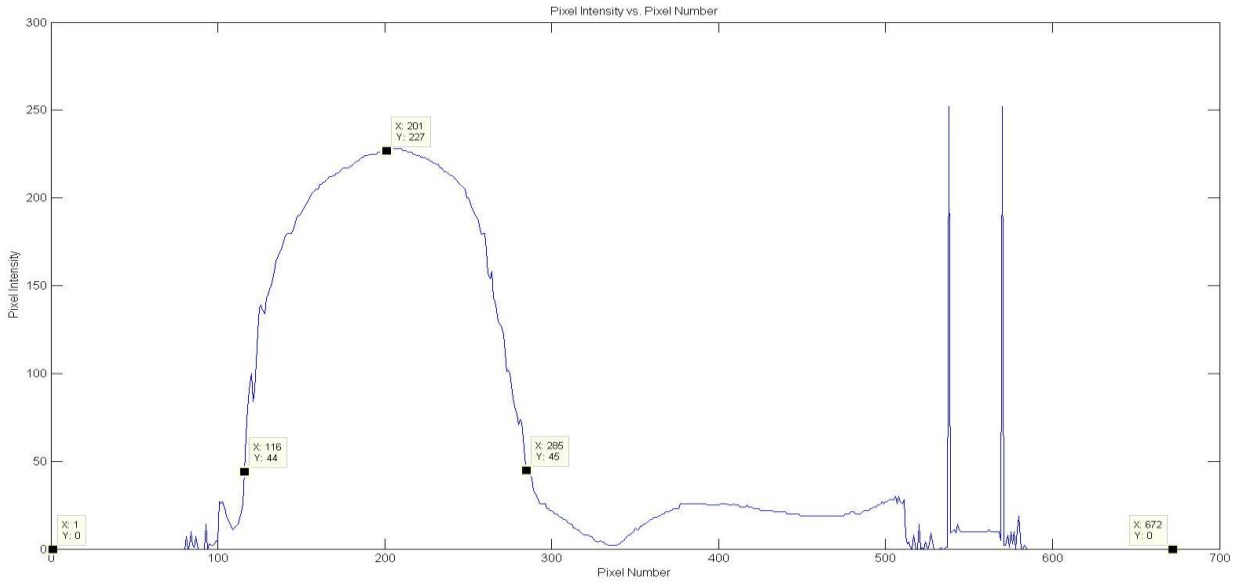

Figure C- 31: Pixel intensity vs. pixel number plot for the reconstructed image when the anomaly was placed at electrode 13. It shows the relevant points that were used to compute the position and size errors. X values from the left of the plot: 1, 116, 201, 285 and 672.

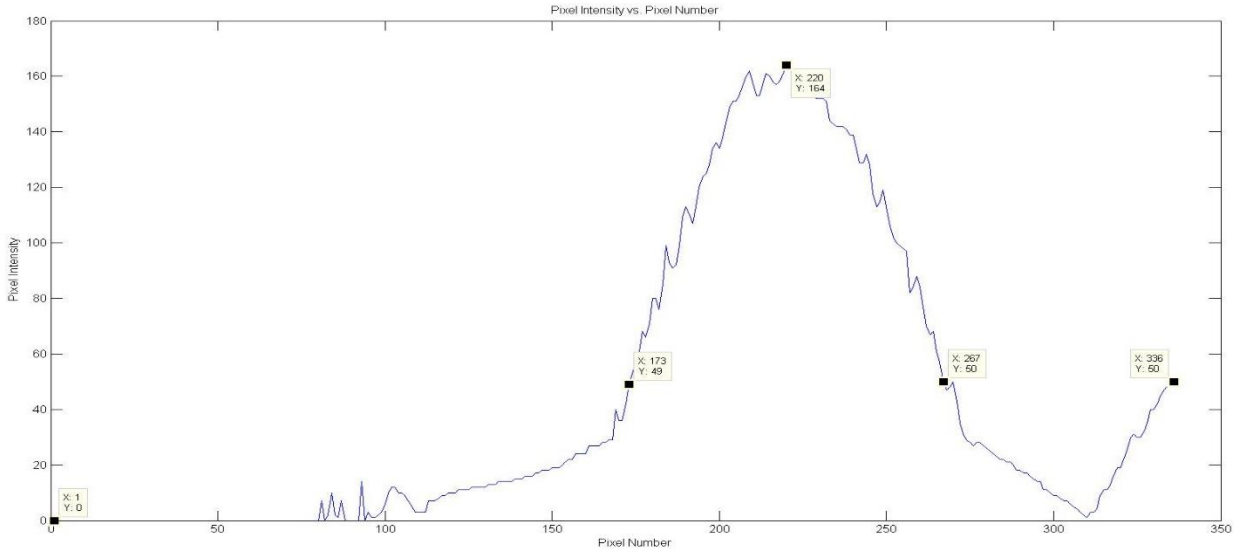

Figure C- 32: Pixel intensity vs. pixel number plot for the reconstructed image when the anomaly was placed at electrode 15. It shows the relevant points that were used to compute the position and size errors. X values from the left of the plot: 1, 173, 220, 267 and 336.